Title
Numerical analysis of the temporal and spatial instabilities on an annular liquid jet

Author
Zandian, Arash

Publication Date
2014

Peer reviewed|Thesis/dissertation

UNIVERSITY OF CALIFORNIA,
IRVINE

Numerical analysis of the temporal and spatial instabilities on an annular liquid jet

THESIS

submitted in partial satisfaction of the requirements
for the degree of

MASTER OF SCIENCE

in Mechanical and Aerospace Engineering

by

Arash Zandian

Thesis Committee:
Professor William A. Sirignano, Chair
Professor Said E. Elghobashi
Professor Roger H. Rangel

2014

TABLE OF CONTENTS

LIST OF FIGURES

LIST OF TABLES

ACKNOWLEDGMENTS

I would like to thank Professor William A. Sirignano, the chair of my committee, who gave me the opportunity of being a part of the UCI Combustion, Propulsion and Computational Fluid Dynamics Laboratory, and has been guiding me through the past years to pursue my studies. Professor Sirignano's support and unique perspective towards different problems was one of the most valuable lessons of my studies at UCI. His trust engaged me in a wide range of exciting projects, while his kindness and warmth inspired team work between the CFD laboratory members.

I would like to also thank Professor Feng Liu and Professor Said Elghobashi for their insightful discussions about the numerical techniques needed for my thesis, as well as their invaluable teachings in fundamentals of fluid mechanics, and mathematics. The courses I have taken with them changed my understanding of partial differential equations and numerical methods.

I am very thankful for Professor Derek Dunn-Rankin's kindness and support which has been crucial during the years I have been at the MAE department. His understanding of graduate students' concerns, and his tireless efforts to improve their condition as well as the department condition has been exemplary.

My many thanks are extended to all my UCI friends and colleagues, with whom I had many fruitful discussions about my research. My special thanks to my colleague, Dorrin Jarrahbashi, who has always assisted me in my research with kindness and patience. Her guidance in both theory and computations has been truly inspiring in my career.

CURRICULUM VITAE

Arash Zandian

EDUCATION

M.S. in Mechanical and Aerospace Engineering **2014**
University of California, Irvine *Irvine, USA*

Bachelor of Science in Mechanical Engineering **2012**
University of Tehran *Tehran, Iran*

RESEARCH EXPERIENCE

Graduate Research Assistant **2012–2014**
University of California, Irvine *Irvine, California*

TEACHING ASSISTANCE

Viscous and compressible flows, MAE 130B **Spring 2014**
University of California, Irvine *Irvine, California*

Introduction to fluid mechanics, MAE 130A **Winter 2013**
University of California, Irvine *Irvine, California*

Introduction to engineering computations, MAE 10 **Fall 2013**
University of California, Irvine *Irvine, California*

Linear control systems **Spring 2012**
University of Tehran *Tehran, Iran*

Thermal power-plants technology **Winter 2011**
University of Tehran *Tehran, Iran*

SELECTED HONORS AND AWARDS

Donald K. Edwards Endowed Fellowship **2012–2013**
Mechanical & Aerospace Engineering Department, UC-Irvine

ABSTRACT OF THE THESIS

Numerical analysis of the temporal and spatial instabilities on an annular liquid jet

By

Arash Zandian

Master of Science in Mechanical and Aerospace Engineering

University of California, Irvine, 2014

Professor William A. Sirignano, Chair

A numerical study of the temporal and spatial instabilities appearing on the interface of an annular liquid jet emerging from an orifice and flowing into a high pressure gas medium has been performed using Direct Numerical Simulation. The purpose of this study is to gain a better insight into the dominant mechanisms in the atomization of annular liquid jets during the start-up portion of the injection. The effects on the growth rate and wavelength of the emerging Kelvin-Helmholtz and Rayleigh-Taylor instabilities of various flow parameters have been investigated: the Reynolds and Weber numbers; fluids properties like gas-to-liquid density and viscosity ratios; and geometrical parameters involved in the problem such as thickness-to-diameter ratio of the liquid sheet. The Reynolds numbers used in this study are in the range from $3,000$ to $30,000$, and the Weber numbers are in the range of $6,000$ up to $150,000$. The convergence rate and length of the liquid jet has been also computed and compared for different cases. A characteristic convergence time has been proposed based on the obtained results. Use has been made of an unsteady axisymmetric code with a finite-volume solver of the Navier-Stokes equations for liquid streams and adjacent gas and a level-set method for the liquid/gas interface tracking.

Two significant velocity reversals were detected on the axis of symmetry for all flow Reynolds numbers; the one closer to the nozzle exit being attributed to the recirculation zone, and the one farther downstream corresponding to the annular jet collapse on the centerline. The effects of different flow parameters on the location of these velocity reversals are studied. The results indicate that the convergence length and time increase significantly with the gas density and liquid viscosity and decrease with the liquid sheet thickness, while the effects of the gas viscosity and the surface tension are not so considerable.

The range of unstable Kelvin-Helmholtz and Rayleigh-Taylor wavelengths have been also studied. The statistical data obtained from the numerical results show that, the average normalized wavelength of the KH instabilities decreases with the Reynolds and Weber numbers and the sheet thickness, and increases with the gas-to-liquid density ratio, and is independent of the viscosity ratio. The wavelength of the KH instabilities were observed to increase in time, except for the very thin liquid sheet, where the average KH wavelength oscillates between two values, indicating occurrence of different sheet breakup cycles. The sheet breakup times and lengths were reported up to the second sheet breakup, and it is shown that the later sheet breakups happen closer to the nozzle exit plane. The RT wavelengths tend to decrease during the start-up period of injection.

KEYWORDS: DNS, Annular liquid jet, Kelvin-Helmholtz instability, Rayleigh-Taylor instability, Finite-volume approach, Level-set method, Convergence length/rate.

Chapter 1

Introduction

1.1 Motivation

Atomization generally refers to the disintegration of a bulk liquid material via an atomizer into droplets in a surrounding gas. Atomizers are utilized in spraying liquids in many industrial and household applications. Gas-liquid two-phase jet flows are encountered in a variety of engineering applications such as fuel injection, propulsion and combustion systems, agricultural sprays and chemical reactors. The instability of the annular jet is of broader interest because at its limits it represents a cylindrical liquid jet, a hollow gas jet or a plane liquid sheet. Annular liquid jets are typically found in air-blasted and air-assisted atomizers which are integral parts in both aircraft propulsion systems and internal combustion engines. Annular liquid jets are known to form in various liquid spray applications. Spray formation through the breakup of an annular liquid sheet has been found to be an efficient process because of the increased surface area for interaction between the gas and the liquid.

The atomization processes may be classified into two major categories in terms of the relative velocity between the liquid being atomized and the ambiance [1]. In the first category, a liquid at high velocity is discharged into a still or relatively slow-moving gas (air or other gases). Notable processes in this category include, for example, pressure atomization and rotary atomization. In the second category, a relatively slow-moving liquid is exposed to a stream of gas at high velocity. This category includes, for example, two-fluid coaxial atomization and whistle atomization. Either of these atomization processes could be accompanied by a swirling flow (either the liquid itself or its surrounding gas) which would increase the instability growth rate and contribute to faster atomization. The initial breakup process is often referred to as primary breakup, primary disintegration, or primary atomization. A population of larger droplets produced in the primary atomization may be unstable if they exceed some critical flow conditions and thus may undergo further disruption into smaller droplets. This process is usually termed secondary breakup, secondary disintegration, or secondary atomization. Therefore, the final droplet size distribution produced in an atomization process is determined by the liquid properties in both the primary and secondary disintegration [1].

The unified design approach of atomizers in different fields requires the interrelations between the different spray characteristics of the atomizers with the pertinent input parameters such as liquid fuel properties, injection conditions and atomizer geometries. This requires a physical understanding of the flow field inside the atomizer and of the mechanism of spray formation outside the atomizer. The modeling of the atomization process is a very challenging task as it is affected by variety of factors as the nozzle geometry, the thermo-physical properties of the liquid, and the aerodynamic liquid-gas interaction. The success of spray modeling depends on the correct specification of the initial droplet conditions. Therefore, direct or indirect coupling of atomizer flow with the primary breakup and spray formation is important for the optimization of the atomizers as well as better understanding and consequent improvement of the overall atomization process.

Liquid-fuel injection systems operate under conditions of high Weber numbers induced by the huge velocity of the jet and high Reynolds numbers. Our purpose is to understand the mechanisms of jet flow under these extreme conditions which lead to the formation of small drops and mist. The disintegration of liquid jets can be framed in terms of instabilities. The instabilities are well known to be critical in the distortion of the liquid/gas interface and in the process by which ligaments of liquid are torn from the jet core. Three kinds of instabilities that can lead to break-up are capillary instability, Kelvin-Hemholtz (KH) instability, and Rayleigh-Taylor (RT) instability. These instabilities can take an axisymmetric form. However, three-dimensional instabilities can also occur. Various parameters affecting the liquid/gas interface instabilities at the early stages of jet injection are to be investigated and compared in this study.

1.2 Literature review

In this part of the Thesis, first the Kelvin-Helmholtz and Rayleigh-Taylor instabilities are introduced; then the works and contributions of the previous researchers on the field of liquid jet instability are brought in four different approaches, which are linear analytical studies, non-linear analysis, experimental observations and numerical studies. The assumptions made in each section and the key findings are mentioned in the corresponding sections.

1.2.1 Capillary instability

The Plateau-Rayleigh instability, often just called the Rayleigh instability or the Capillary instability, explains why and how a falling stream of fluid breaks up into smaller packets with the same volume but less surface area. The Plateau-Rayleigh instability is named after Joseph Plateau and Lord Rayleigh.

In 1873, Plateau found experimentally that a vertically falling stream of water will breakup

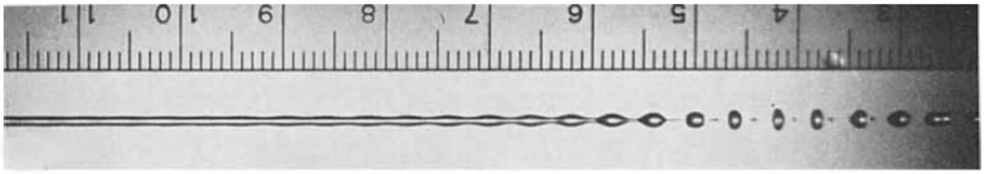

Figure 1.1: Typical photograph of a liquid jet, showing the formation of main and satellite drops from capillary instabilities.

into drops if its wavelength is greater than about 3.13 to 3.18 times the stream diameter. Later, Rayleigh [2] showed theoretically that a vertically falling column of non-viscous liquid with a circular cross-section should breakup into drops if the wavelength of the instabilities on the surface of the column exceeded the circumference of the column cross-section.

Studies of capillary instability have revealed that a liquid jet is unstable for axial disturbances with wave numbers less than a cut-off wave number k_c, but stable otherwise. For each wavelength of an unstable disturbance one main drop and one or more usually smaller drop(s), referred to as the satellite or spherous drop(s), are formed. Figure 1.1 shows image of a typical liquid jet becoming unstable when it is subject to small perturbation. The instabilities grow and cause the liquid jet to finally break-up into the main and satellite droplets.

The classical study of the capillary instability of liquid jets was published in the seminal work of Lord Rayleigh [2]. With the assumption of an inviscid liquid, he obtained an equation for the growth rate of a given axisymmetric surface disturbance by equating the potential and kinetic energies computed for the flow. Further, with the hypothesis that the disturbance with the maximum growth rate would lead to the breakup of the jet, he obtained an expression for the resulting droplet size assuming that it would be of the order of the wavelength of this disturbance. Later, Weber [3] included the effect of viscosity in his analysis of the jet breakup based on the three-dimensional partial differential equations of hydrodynamics of Newtonian viscous liquids. He found that the effect of the liquid viscosity is to shift the fastest growing waves to longer wavelengths and to slow down their growth rate, without, however, altering the value of the cut-off wave-number.

The explanation of capillary instability begins with the existence of tiny perturbations in the stream. These are always present, no matter how smooth the stream is. These disturbances may be in the form of surface displacement, pressure or velocity fluctuations in the supply system or on the jet surface, as well as fluctuations in liquid properties such as temperature, viscosity, or surface tension coefficient. If the perturbations are resolved into sinusoidal components, we find that some components grow with time while others decay with time. Among those that grow with time, some grow at faster rates than the others. Whether a component decays or grows, and how fast it grows is entirely a function of its wave-number and the radius of the original cylindrical stream.

When a liquid/gas interface is deformed, as shown in Figure 1.2, the surface tension forces may tend to bring it back to its equilibrium shape. The equilibrium shape of the interface is defined based on all the forces that may act on it, including the gravitational and pressure forces. On a flat interface, as the disturbed interface tends to move to its equilibrium shape, a wave-like propagation appears. If the forces that are acting on the disturbed interface are the surface tension or the capillary forces, the waves are referred to as the capillary waves.

Although a thorough understanding of how this happens requires a mathematical development, Figure 1.2 can provide a conceptual understanding. At the trough, the radius of the stream R_1 is smaller. Hence according to the Young-Laplace equation, the pressure due to surface tension is increased. Likewise at the peak the radius of the stream is greater and, by

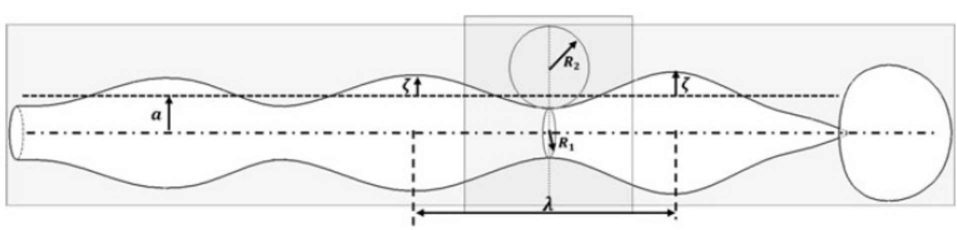

Figure 1.2: Schematic of an unstable jet.

the same reasoning, pressure due to surface tension is reduced. If this were the only effect, we would expect that the higher pressure in the trough would squeeze liquid into the lower pressure region in the peak. In this way we see how the wave grows in amplitude over time.

But the Young-Laplace equation is influenced by two separate radius components. In this case one is the radius R_1, already discussed, of the stream itself. The other is the radius of curvature of the wave itself, R_2. The fitted arc in the figure shows this radius at a trough. Observe that the radius of curvature at the trough is, in fact, negative, meaning that, according to Young-Laplace, it actually decreases the pressure in the trough. Likewise, the radius of curvature at the peak is positive and increases the pressure in that region. The effect of these components is opposite to the effects of the radius of the stream itself.

The two effects, in general, do not exactly cancel. One of them will have greater magnitude than the other, depending upon wave number and the initial radius of the stream. When the wave-number is such that the radius of curvature of the wave dominates that of the radius of the stream, those waves will decay over time. When the effect of the radius of the stream dominates that of the curvature of the wave, such instabilities grow exponentially with time.

Provided that the wavelength of surface deformation is long, the curvature $1/R_1 >> 1/R_2$ at the trough. Since liquid pressure is primarily balanced by capillary pressure due to curvature $1/R_1$, a greater liquid pressure is induced by a smaller radius of the cylinder. The positive difference in the pressures thus induces a perturbed flow from trough to the neighboring peak. The system therefore is unstable and breakups the cylinder into droplets. However, for deformation with small wavelength, the curvature $1/R_2 >> 1/R_1$ at the trough. The perturbed pressures at trough therefore decrease and it can be smaller than perturbed pressure at the neighboring peak, leading to the flow from peak to the trough, and stabilizing the system.

1.2.2 Kelvin-Helmholtz instability

The instability of uniform flow of incompressible fluids in two horizontal parallel infinite streams of different velocities and densities, is known as the Kelvin-Helmholtz (KH) instability [4]. The name is also commonly used to describe the instability of the more general case where the variations of velocity and density are continuous and occur over a finite thickness.

The KH instability is produced by the action of pressures on the perturbed interface; the instability is often discussed as being due to shear, but shear stresses are not the major actor here and in any event could not be inserted into an analysis based on potential flow even when viscosity is not neglected [4]. The formation of the instability may be described in terms of the action of pressure in Bernoulli equation which is small where the speed is great (at the top in Figure 1.3) and large where it is small (in troughs). An example of the KH instability due to wind shear in the atmosphere is shown in Figure 1.4.

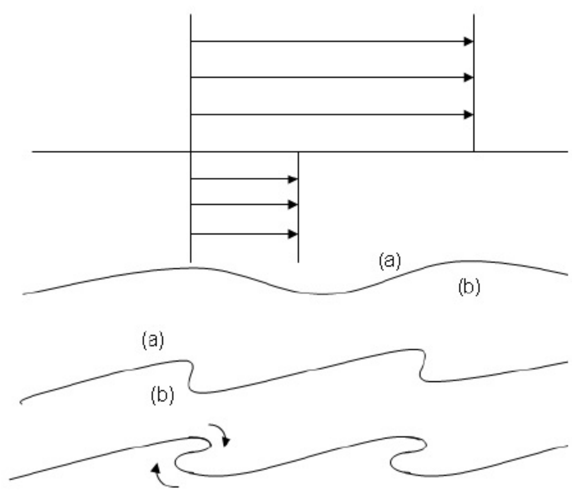

Figure 1.3: The speed of the fluid above is greater. The pressure is greater at crests (a) than at troughs (b). The upper part of the interface is carried by upper fluid causing the interface to overturn [4].

Figure 1.4: A KH instability rendered visible by clouds over Mount Duval in Australia [4].

1.2.3 Rayleigh-Taylor instability

The Rayleigh-Taylor (RT) instabilities are very important and very pervasive. They are driven by acceleration when a liquid accelerates away from a gas or a lighter fluid. The signature of this instability is the waves which corrugate the free surface at the instant of acceleration. Ultimately, these waves will finger into the liquid causing it to break-up [4].

Rayleigh [2] showed that a heavy fluid over a light fluid is unstable, as common experience dictates. He treated the stability of heavy fluid over light fluid without viscosity, and he found that a disturbance of the flat free surface grows exponentially like $\exp(\omega t)$ where

$$\omega = \left\{ \frac{kg(\rho_2 - \rho_1}{\rho_1 + \rho_2} \right\}^{1/2} \tag{1.1}$$

where ρ_2 is the density of the heavy fluid, ρ_1 is the density of the light fluid, g is the acceleration due to gravity and $k = \frac{2\pi}{\lambda}$ is the wavenumber and λ is the wavelength. The instability described by (1.1) is catastrophic since the growth rate ω tends to infinity, at any fixed time, no matter how small, as the wavelength tends to zero.

Nature will not allow such a singular instability; for example, neglected effects like viscosity and surface tension will enter the physics strongly at the shortest wavelength. These effects have been taken into account in the study of RT instability by later researchers. Surface

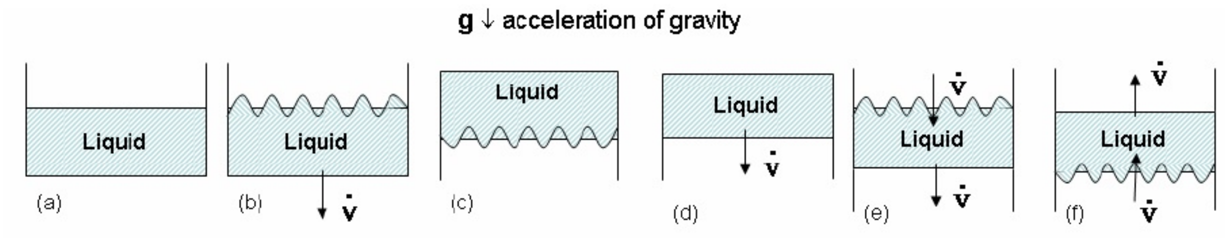

Figure 1.5: RT instability: (a) the liquid in the containers at rest is stable under gravity (Rayleigh 1890) but if the container is turned upside down as in (c) the liquid falls out. The liquid at rest in container can be destabilized by downward acceleration of the liquid $\dot{V} > g$ away from gas as in (b) and in the upside down case the liquid can be prevented from falling out by accelerating downward with $\dot{V} > g$ as in (d). If we open up the container and accelerates the liquid downward with $\dot{V} > g$, the top surface which accelerates away from the gas is unstable but the bottom surface which accelerates into the gas is stabilized as in (e), with the opposite effect when the acceleration is reversed as in (f) [4].

tension eliminates the instability of the short waves; there is a finite wavelength depending strongly on viscosity as well as surface tension for which the growth rate ω is maximum. This is the wavelength that should occur in a real physical problem and would determine the wavelength on the corrugated fronts of breaking drops in a high-speed air flow.

Taylor [5] extended Rayleigh's inviscid analysis to the case where a constant acceleration of the superposed fluids other than gravity is taken into account. Assuming a constant value for the acceleration, Taylor showed that when two superposed fluids of different densities are accelerated in a direction perpendicular to their interface, this surface is unstable if the acceleration is directed from the lighter to the heavier fluid [4]. The Taylor instability depends strongly on the value of the acceleration.

The idea behind Rayleigh and Taylor's instabilities are embodied in the cartoons and caption of Figure 1.5. These experiments show the difference between the theory of Rayleigh [2] who considered gravity g and Taylor [5] who considered the effect of the acceleration $\dot{V}$. The accelerations destabilize the liquid-gas surfaces which accelerate away from the gas and stabilize the liquid-gas surface which accelerate toward the gas (Figure 1.5 (e)).

1.2.4 Linear analyses

The practical and wide applications of liquid jets led to extensive investigation of the flow of liquid sheets and jets, which have received much attention in the literature since the classical studies of Rayleigh. A considerable number of works on the instability of liquid sheets and jets are available in the literature. In this part the linear analyses on liquid sheets (planar and annular) instabilities are presented.

In the classical studies it was usual to study the instability by linearizing the nonlinear equations around the basic uniform flow followed by analysis of normal modes proportional to

$$\exp(\omega t + ikx) \tag{1.2}$$

where $k = \frac{2\pi}{\lambda}$ is the wave number and $\omega = \omega_r + i\omega_i$ is the complex frequency. The real part of ω will be the growth/decay rate of the perturbations and the imaginary part will represent the waves' speed. It is clear that for positive ω_r the perturbations will grow unstably. It is also usual to assume that the fluids are inviscid and the amplitude of perturbations on the liquid/gas interface are much smaller than their wave length as well as the sheet thickness ($\varepsilon << \lambda$, $\varepsilon << h$).

The linear instability of a thin liquid sheet was first investigated by Squire [6] and Hagerty & Shea [8], and both liquid and gas phases were taken as inviscid and incompressible. Squire, Hagerty & Shea showed that there can only exist two modes of unstable waves on the two gas/liquid interfaces for liquid sheets in a stationary gas medium, corresponding to the two surface waves oscillating exactly in and out of phase, commonly referred to as the sinuous (anti-symmetric) and varicose (symmetric, dilational) modes, and that the sinuous mode is always predominant under the typical conditions for practical applications. However, later studies have revealed that this is not generally the case. They also performed the first experimental measurements of the wave growth and wavelength for liquid sheets under

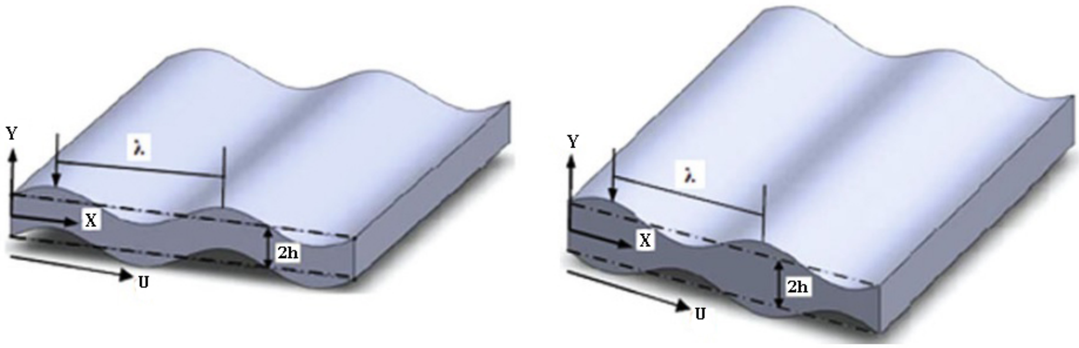

Figure 1.6: A schematic of the instability modes; Sinuous (left), Varicose (right).

various flow conditions, and the theoretical predictions were compared favorably with their experimental results. A schematic of the two instability modes is illustrated in Figure 1.6.

The growth rate found by Squire [6] and Hagerty & Shea [8] are of the form:

$$\frac{\omega_r}{kU_0} = \left\{ \frac{\hat{\rho}K}{(\hat{\rho}+K)^2} - \frac{kh}{We}\frac{1}{\hat{\rho}+K} \right\}^{1/2} \tag{1.3}$$

where U_0 is the liquid sheet velocity, $\hat{\rho} = \rho_g/\rho_l$ is the gas to liquid density ratio, h is the sheet half thickness and $We = \rho_l {U_0}^2 h/\sigma$ is the Weber number. In this equation, $K = tanh(kh)$ for the sinuous mode and $K = Coth(kh)$ for the varicose mode.

Figure 1.7, adopted from Sirignano & Mehring [9], provides the growth rate for various wave numbers for both sinuous (antisymmetric) and dilational (symmetric) waves and for different Weber numbers and density ratios. The results also show that the varicose mode is more unstable for density ratios near unity. It is clear that for the low Weber number case, the growth of sinuous waves dominate the growth of varicose waves due to the higher growth rates throughout the range of instability.

Dombrowski and Johns [7] combined a linear model for temporal instability and a sheet breakup model for an inviscid liquid sheet in a quiescent inviscid gas to predict the ligament and droplet sizes after breakup. The schematic of their wavy sheet is reproduced in Fig. 1.8.

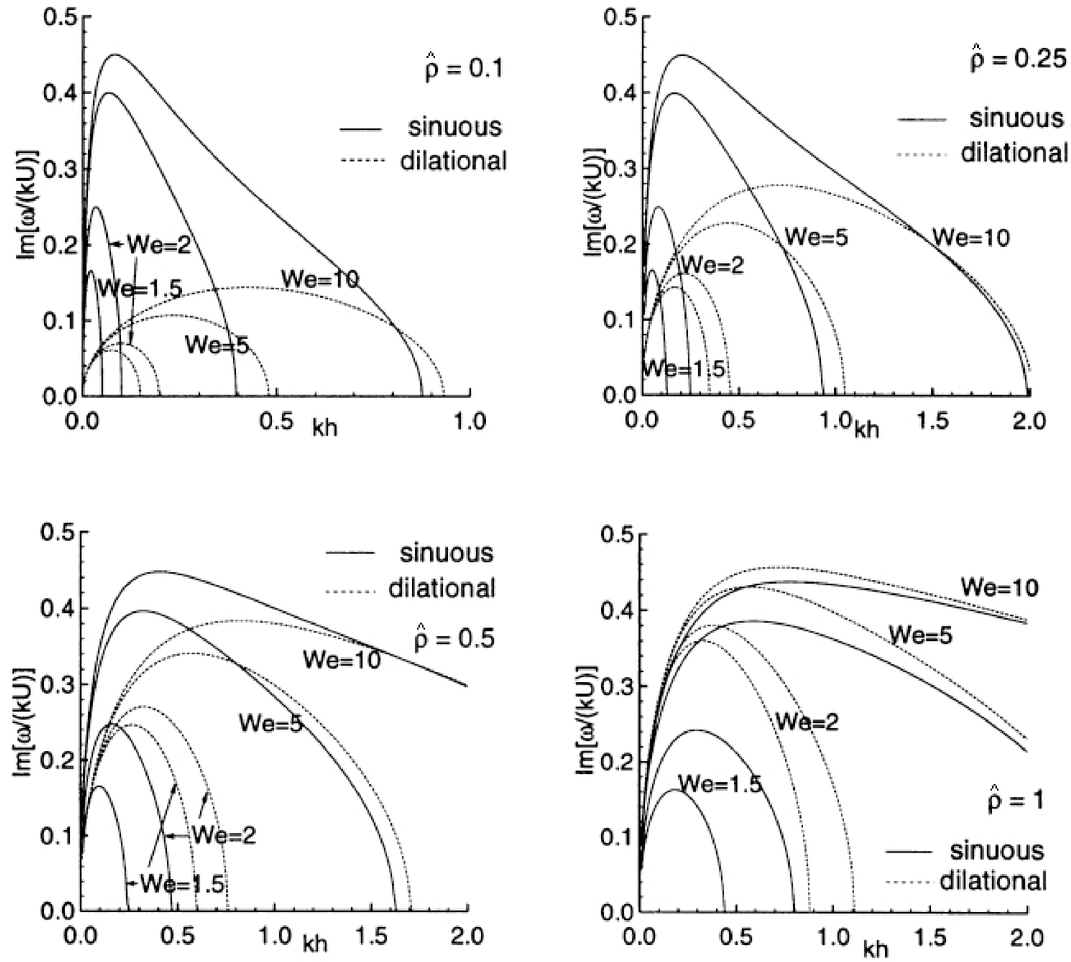

Figure 1.7: Dimensionless growth rate $\mathrm{Im}[\omega/(kU_0)]$ as function of kh for different values of We and $\hat{\rho}$, for inviscid liquid sheet [9].

The equation of motion of the neutral axis mid-way between the two gas/liquid interfaces was obtained for a sheet moving with velocity U_0 through stationary gas. The equation of motion was obtained by considering the forces due to gas pressure, surface tension, liquid inertia, and viscosity on an element of a sheet.

Li & Tankin [10] brought into account the effects of liquid viscosity on the liquid sheet instability. They realized that for sheets, the surface tension always opposes the onset and development of instability, while in liquid jets, it is destabilizing at low velocities and stabilizing at higher relative velocities. Li & Tankin called the instabilities that are caused by velocity difference between the gas and liquid for an inviscid liquid sheet (Squire's equation)

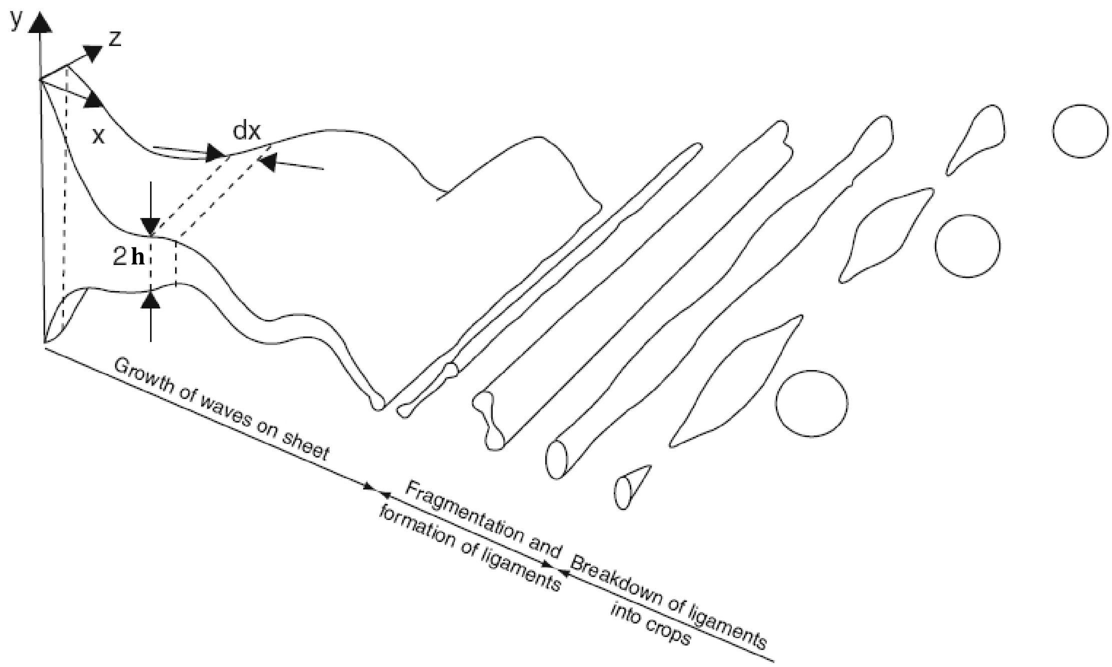

Figure 1.8: Wave instability of a thinning liquid sheet [7].

the aerodynamic instabilities [10]. They then claimed that there is a region of instability that is induced and enhanced by liquid viscosity, which they called the viscosity-enhanced instability. They also found that for low gas Weber numbers, the aerodynamic instability disappears, but the viscosity-enhanced instability still exists. They also presented some simplified relations for the cut-off (neutral) and the dominant wave number (the wave number with maximum growth rate) for very thin liquid sheets. They found that the dominant wave number of the viscous liquid sheet is related to its counterpart for inviscid liquid for $kh << 1$ through the Ohnesorg number, $Oh = \mu_l/\sqrt{\rho_l h\sigma}$.

The first study on annular jet flow appears to be the one reported by Ponstein [11], who treated swirling liquid jets and then annular jets with both surfaces free. Ponstein observed that in non-rotating jets only axisymmetric disturbances are unstable. Crapper et al. [12] analyzed theoretically the instability of an inviscid cylindrical liquid sheet moving in an inviscid gas medium at rest. They found that the sinuous (anti-symmetric) disturbance mode is the dominant mode for the variations of thickness and radius. They also demonstrated that the growth rate of both symmetric and antisymmetric waves increases significantly with reduction of the radius of the sheet annulus [12].

Meyer and Weihs [13] investigated analytically the capillary instability of a stationary viscous annular liquid jet in a moving inviscid gas stream. A critical penetration thickness was identified to classify whether an annular jet behaves like a cylinder jet or a thin planar sheet. When the annular jet behaves like a circular jet the axisymmetric mode was found to be the only unstable disturbance and its growth rate was found to be independent of the thickness. On the other hand, When the annulus thickness is less than the penetration thickness, the jet behaves like a two-dimensional liquid sheet; the most unstable perturbations are anti-symmetric and their growth rate increases as the sheet thickness decreases [13].

The instability of a stationary viscous annular liquid sheet with different gas velocities for the inner and outer gas streams has been studied by Lee and Chen [14]. Two dispersion relations corresponding to each interface were derived. However, only the cases for inviscid liquids were examined. Effects due to ambient fluid density and ambient fluid velocity on liquid-sheet instabilities were examined. They also found that the presence of air does not have discernible effects on symmetric disturbances; however, it shifts the maximum growth rate to a larger wave number for anti-symmetric disturbances [14]. The schematic of the two instability modes for annular liquid sheets given by Lee & Chen are illustrated in Figure 1.9.

Shen and Li [15, 16] carried out a temporal instability analysis of an annular viscous liquid jet

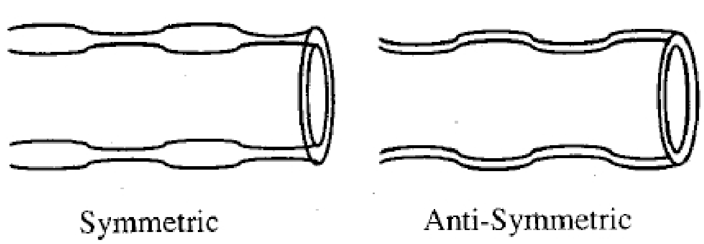

Figure 1.9: Schematic of symmetric and antisymmetric disturbances of cylindrical liquid sheets.

moving in an inviscid gas medium and then recovered both analytical and numerical results of plane liquid sheets, round liquid jets and hollow gas jets found by former researchers. They showed that curvature effects in general increase the disturbance growth rate, hence promoting the annular sheet breakup process. They found the two instability modes on the interfaces of annular sheet to be similar to the well known sinuous and varicose modes in the limit of planar liquid sheet; hence, they named them para-sinuous and para-varicose modes [15]. Liquid viscosity enhances sheet instability only at low Weber numbers and for para-sinuous modes, which is similar to the behavior of plane liquid sheets examined by Li and Tankin [10]. A critical Weber number was identified below which surface tension promotes instability, whereas above this value, surface tension inhibits instability. In [16], Shen & Li apply the linear stability theory to the study of breakup process of an annular viscous liquid jet exposed to both inner and outer gas streams of unequal velocities. It is found that not only the velocity difference across each interface, but also the absolute velocity of each fluid is important for the jet instability, although the effect of absolute velocity is secondary compared with that of relative velocity. They also realized that a high-velocity coflowing gas inside of the annular liquid jet promotes the jet breakup process more than the gas of equivalent velocity outside of the jet. The liquid inertia, density ratio, and high gas velocity all contribute to better atomization performance, whereas surface tension and liquid viscosity increase the resulting droplet size [16].

Jeandel and Dumouchel [17] studied the linear stability of an annular liquid sheet evolving in a gaseous environment at rest, taking into account the liquid viscosity. They derived a non-dimensional number $D = \frac{We_h}{Re}(We_h + h/a)$ based on the Reynolds and Weber numbers and sheet thickness to radius ratio (h/a), which allows one to account for the influence of the liquid viscosity on the linear stability of an annular liquid sheet. They found that for $D < 10^{-4}$, the viscous effects are negligible on the dominant wave-number and the maximum growth rate of the instabilities.

The effect of gas compressibility on the liquid sheet instability has also been investigated by Li & Kelly [18] for inviscid liquid sheets and by Cao & Li [19] for viscous liquid sheets in two gas streams of unequal velocities. It was shown that gas compressibility always enhances the instability and breakup processes of liquid sheets.

Sirignano and Mehring [9] summarized the results of the linear sheet instability theory as follows: "For all density ratios, the growth rate for both sinuous and dilational waves increases as the Weber number is increased. The maximum growth rate for the sinuous disturbances does not significantly change with changes in the density ratio. However, the maximum growth rate for the dilational case increases significantly as density ratio is increased. For low-density ratios, the maximum growth rate for the sinuous case is always higher than that for dilational waves. As $\hat{\rho}$ is increased beyond a certain value, the maximum growth rate for dilational waves eventually overcomes the value for sinuous growth. For all density ratios, there exists a region of wave numbers, in which dilational waves are more unstable than the sinuous ones; the latter might even be stable in that region. The disturbance wavelength with maximum growth rate decreases as the density ratio is increased. This is true for both sinuous and dilational waves".

Craster et al. [20] conducted a linear stability analysis of axisymmetric compound viscous jets (core-annular flow) using long-wave theory. An asymptotic reduction of the 1D set of equations was performed to explore the dynamics of the fluids, and the ratio of fluid densities was assumed to be the same as that of the viscosities. The linear study predicts that the para-sinuous mode is the dominant one, which is in agreement with the previous works. In the limit of small wave number (i.e. $k << 1$) and for a highly viscous annular liquid compared to the core gas, Craster et al. found analytically that the inner-to-outer interfacial amplitude ratio is approximately equal to the inner-to-outer radius ratio [20].

Ibrahim & McKinney [21] formulated a simplified mathematical model, based on body-fitted coordinates, to study the evolution of non-swirling and swirling liquid sheets emanated from an annular nozzle in a quiescent surrounding medium. It was found that a non-swirling annular sheet converges towards its centerline and assumes a bell shape as it moves downstream from the nozzle. They found that both the thickness and the stream-wise velocity of the non-swirling annular sheet are reduced with an increase in mass flowrate [21]. The introduction of swirl results in the formation of a diverging hollow-cone sheet. The hollow-cone divergence from its centreline is enhanced by an increase in liquid mass flowrate or liquid-swirler angle [21].

Fu et al. [22] used a linear instability analysis method to investigate the breakup of a conical liquid sheet under the combined influence of sinuous and varicose modes of disturbances at the liquid-gas interfaces, and adopted a modified model to predict the breakup length of the conical liquid sheet. They found that, for both modes, the maximum disturbances growth rate and the dominant wave number increase as the pressure drop increases, while the breakup length and breakup time decreases with the increase of the pressure drop.

Ahmad et al [23] carried out a temporal stability analysis to investigate the stability of an axially moving viscous annular liquid jet subject to axisymmetric disturbances in surrounding co-flowing viscous gas media. They investigated in their study the effects of inertia, surface tension, the gas-to-liquid density ratio, the inner-to-outer radius ratio and the gas-to-liquid viscosity ratio on the stability of the jet. A summary of the influence of flow and geometrical effects on the annular liquid sheet instability found by Ahmad et al. is given in Table 1.1 .

1.2.5 Nonlinear analyses

In all the above-cited theoretical studies, linearized stability analysis has been employed. The linear theory does not offer a means for the liquid sheet to break up, because during the growth of the sinuous mode of disturbances predominant under practical conditions, the two gas-liquid interfaces remain a constant distant apart. Hence, the liquid sheet breakup

Stability parameter	Disturbance growth rate	Mode of instability	Dominant wave-number	Maximum growth rate
Inertia	Increase	Para-Sinuous	Increase/Decrease (at negligible/large viscosity ratio)	Increase
Density ratio	Decrease	Para-Sinuous	Increase	Decrease
Radius ratio	Decrease (Increase in thin annular sheet)	Para-Sinuous	Decrease (Increase in thin annular sheet)	Decrease (Increase in thin annular sheet)
Surface tension	Increase	Both para-sinuous and para-varicose	Almost constant	Increase
Viscosity ratio	Decrease	Para-sinuous	Increase	Decrease

Table 1.1: Summary of parametric influence on the growth rate, mode of instability, the dominant wave-number and the maximum growth rate for axisymmetric disturbance [23].

length, which is an important parameter in the spray modeling and spray system design, cannot be predicted based on the linear theory alone. In reality, the liquid sheet breakup processes are nonlinear, especially near the breakup region [24].

So far, only limited studies have been carried out on the nonlinearity of the liquid sheet breakup processes. Clark & Dombrowski [25] were the first to analyze nonlinear liquid sheet disintegration through the perturbation expansion technique with initial disturbance amplitude as the perturbation parameter. A solution accurate up to the second order of the initial disturbance amplitude was obtained for the case of wavelengths relatively long compared with the sheet thickness. It was found that sheet thinning was caused by the growth of the harmonic wave, with maximum thinning and subsequent rupture occurring at positions corresponding to 3/8 and 7/8 of the length of the fundamental wave [25]. The theoretical results were also used to calculate the breakup lengths of attenuating liquid sheets produced by fan and swirl spray nozzles, and compared with experimental measurements.

Rangel & Sirignano [26] used the vortex-sheet discretization method and computation technique to investigate the nonlinear evolution of initially small disturbances at an interface separating two fluids of different density and velocity with effects of surface tension included.

The same approach was also used in a later study by Rangel & Sirignano [27] for the linear and nonlinear instability of a finite-thickness fluid sheet in contact with two semi-infinite streams of a different fluid. Their nonlinear calculations indicate the existence of sinuous oscillating modes when the density ratio is of the order of 1. It was shown that sinuous disturbances may result in the formation of ligaments interspaced at half the wavelength of the fundamental mode [27].

Panchagnula et al. [28] have developed a nonlinear model of annular liquid sheet using approximate one-dimensional equations derived by thin sheet approximations. They have considered only the para-varicose disturbances and have neglected the aerodynamic effects of the gas phase inside and outside the liquid sheet. It has been reported in the earlier studies that the para-varicose disturbances dominate the breakup process at very low liquid Weber numbers. In most practical atomizers, liquid Weber numbers are generally high and the para-sinuous disturbances dominate the breakup process in this regime [28].

In a series of nonlinear studies, Mehring and Sirignano [29–33] have developed nonlinear models of axisymmetric thin inviscid infinite (periodically disturbed) and semi-infinite (locally forced) annular liquid sheets in a surrounding void with non-zero gas core pressure at zero gravity by employing a reduced dimension approach (long-wavelength approximation). They found that there will be no Kelvin-Helmholtz instability if the ambient density is zero.

Jazayeri and Li [24] developed up to the third order nonlinear analysis of a liquid sheet to determine the breakup length of the sheet. Their results indicate that, for an initially sinusoidal surface disturbance, the thinning and subsequent breakup of the liquid sheet is due to nonlinear effects with the generation of higher harmonics as well as feedback into the fundamental. The breakup time (or length) of the liquid sheet was calculated, and the effect of the various flow parameters was investigated. It was found that the breakup time (or length) is reduced by an increase in the initial amplitude of disturbances, the Weber number and the gas-to-liquid density ratio, and it becomes asymptotically insensitive to the variations of the Weber number and the density ratio when their values become very large. It was also found that the breakup time (or length) is a very weak function of the wave-number unless it is close to the cut-off wave-numbers [24]. Jazayeri & Li found that the distance between the two interfaces vanishes near the half and full wavelength, which is different from the conclusions reached by Clark and Dombrowski [25] who found that the sheet breakup occurred at positions corresponding to 3/8 and 7/8 of the length of the fundamental wave. However, the liquid sheet breaks off at half-wavelength intervals, a result consistent with that of Clark and Dombrowski.

Nonlinear instability and breakup of an annular liquid sheet exposed to co-flowing inner and outer gas streams was modeled by Ibrahim & Jog [34]. They also studied the effect of outer gas swirl on sheet breakup. In their developed model a perturbation expansion method was used with the initial magnitude of the disturbance as the perturbation parameter. In their temporal analysis, the effect of liquid Weber number, initial disturbance amplitude, inner and outer gas-to-liquid velocity ratios, and outer gas swirl strength on the breakup time was investigated. Their results showed that with increasing outer gas swirl strength, the maximum disturbance growth rate increases and the most unstable circumferential wave number increases resulting in a highly asymmetric sheet breakup with shorter breakup lengths and thinner ligaments [34].

1.2.6 Experimental studies

The optical measurement techniques such as shadowgraph and Schlieren imaging and laser-based techniques, e.g., Mie scattering imaging and laser-induced fluorescence produce obscure images from the regions of high droplet density near the nozzle since the light scatters from the surface of the droplets. The above mentioned reasons have made it a difficult, yet interesting, task for many researchers to develop various experimental techniques to study the near nozzle jet instabilities.

The transient behavior of liquid injection has been the subject of numerous experimental studies for planar liquid sheets (Crapper et al. [35], Mansour & Chigier [36]), cylindrical liquid jets (Varga et al. [37], Marmottant & Villermaux [38], Crua et al. [39], Shoba et al. [40]) and annular liquid sheets (Kendall [41], Carvalho & Heitor [42], Fu et al. [43], Wahono et al. [44] and Duke et al. [45]). However, studies that only pertain to annular liquid jets are summarized in this section.

Kendall [41] performed experiments on annular liquid jet with coflowing airstream inside the annular sheet at relatively small velocities (1 m/s to 12 m/s). It was shown that periodic, axisymmetric oscillations arise spontaneously within the cylindrical sheet emerging from the nozzle and grow with such rapidity along the axial dimension that a sealing-off and encapsulation of the core gas occurs within a few jet diameters. He also found gravity to be unimportant to the shell formation.

Lee and Chen [14] identified three regimes for air-assisted atomization; namely, the Rayleigh, intermittent, and atomization regimes. At low airflow rates, periodic bubble formation was observed. This bubble-formation regime was termed the Rayleigh regime due to the similarity between the bubble formation and the droplet formation of low-velocity liquid jets. As the airflow rate is increased, the spacing between bubbles are decreased, and the bubble shape is distorted. This regime was termed the intermittent regime. With further increase in the airflow rate, small liquid drops are formed near the nozzle exit and the flow regime was named the atomization regime. Figure 1.10 shows the typical regimes observed by Lee & Chen in their experiments [14].

Later in 2000, Sirignano and Mehring [9] in their review of the theory of distortion and disintegration of liquid streams, identified the operation regimes of round liquid jet breakup into four distinct regimes, similar to what was found by Lee & Chen [14]. They identified

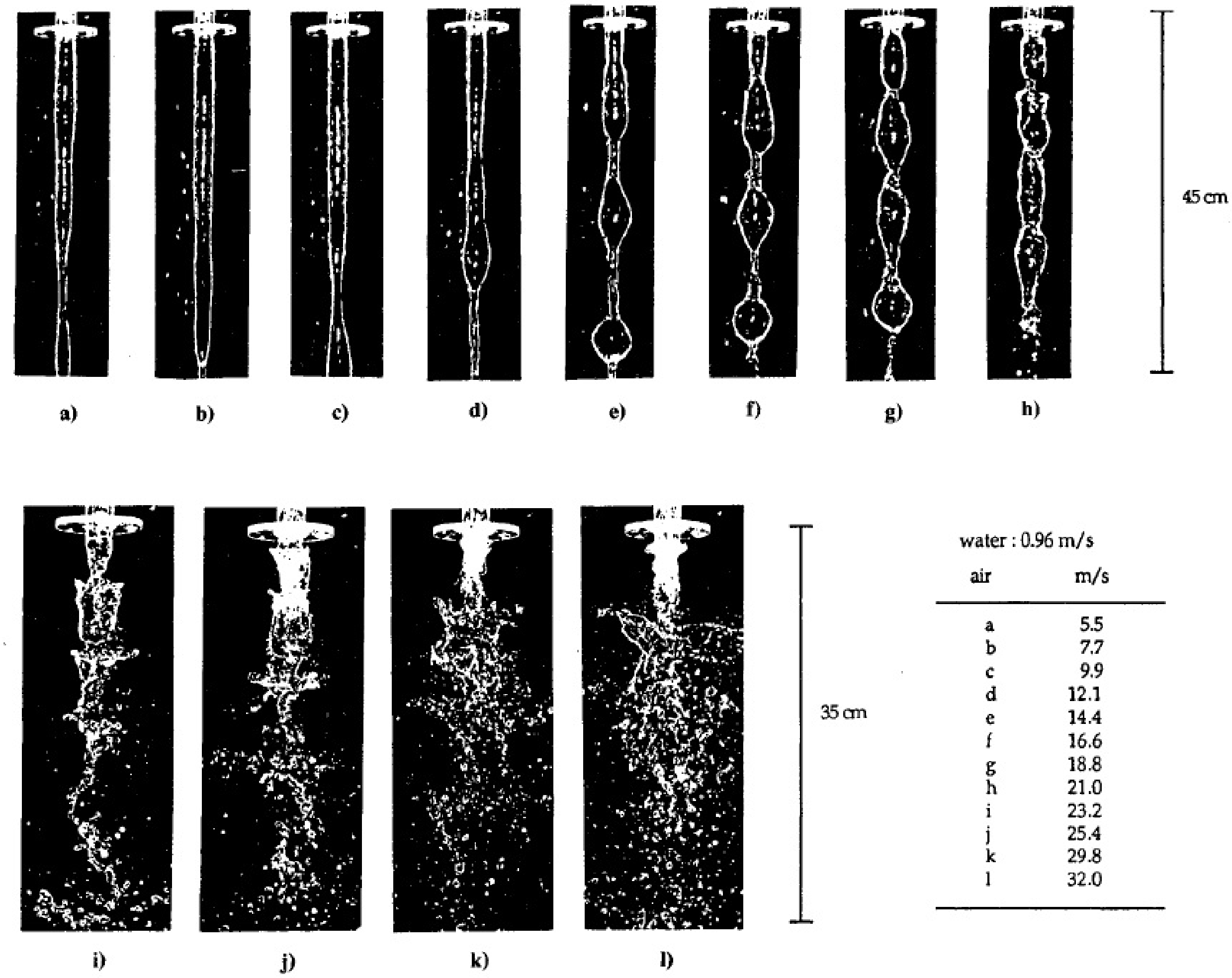

Figure 1.10: Flow characteristics of annular jets (water velocity = 0.96 m/s). Rayleigh regime (a–e), Intermittent regime (f–h), atomization regime (i–l) [14].

the regimes to be separated by straight lines with negative slope on the log-log plot of We (or Oh) versus Re as illustrated in Figure 1.11. The first domain is the Rayleigh capillary mechanism region at lower values of We and Re. Aerodynamic interaction with the gas is not significant. Axisymmetric distortion occurs with the formation of droplets that have a radius of the same order as the jet radius. Next is the first wind-induced region where non-axisymmetric (sinuous) oscillations occur resulting still in droplet sizes comparable to the jet radius. The second wind-induced region results in small droplets, while the atomization region at the highest values of We and Re result in the smallest droplets. As the Weber number or Ohnesorge number increases, the break-up length tends

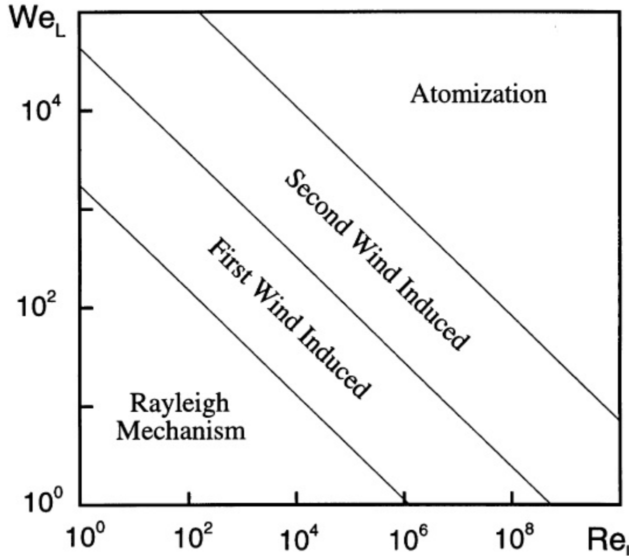

Figure 1.11: Modes of disintegration in dependence on liquid Reynolds and Weber numbers [9].

to decrease. The atomization regime is the domain where the break-up essentially occurs at the orifice exit [9].

Carvalho and Heitor [42] studied the atomization process of a liquid in an axissymmetric shear layer formed through the interaction of turbulent coaxial jets (respectively, inner and outer jets), with and without swirl, in a model airblast prefilming atomizer. The atomization process and spray quality was studied using different visualization techniques, namely laser shadowgraphy and digital image acquisition. The experiments were conducted for different liquid flow rates, Reynolds numbers ranging from 6600 to $66,000$ and $27,300$ to $92,900$ for the inner and outer air flows, respectively, for different outer flow swirl levels, and two liquid film thicknesses 0.2 and 0.7 mm. They found that film thickness strongly affects the time and length scales of the break-up process for the lower range of air velocities, and that the inner air stream is more effective on promoting atomization than the outer air flow.

Fu et al. [43] in their study, investigated experimentally the breakup characteristics of annular liquid sheets in two co-flowing air streams, by using a backlighting technique and a computer-controlled high-speed CCD camera. Their results indicate that transition from laminar to turbulent flow for the liquid sheets does not seem to affect much the breakup length and the pattern of the resulting sprays when comparing to the effect of changing the airflow velocities. The breakup length, defined as the distance from the nozzle exit to the location of the sheet breakup, increases with the liquid velocity, while is shortened by the air stream velocity [43].

Wahono et al. [44] in their experimental study, illuminated the liquid sheet with high-powered halogen lamps, and used high-speed imaging to qualitatively visualize the structure of the spray. Their particular interest was the evolution of the spray into a ligament structure during the primary break-up and the role the outer air stream plays in this process. Their observations showed that thicker and longer ligaments are formed with higher Re numbers, which they concluded to be associated with higher liquid momentum. They also found the Strouhal number (St) to increase with increasing gas to liquid momentum ratio.

Later on high-speed backlit photography was used by Duke et al. [45] to capture realizations of the unstable mixing layer, and the edge velocity was derived in order to measure the effects of parameters such as gas/liquid momentum ratio, Reynolds and Weber Number. The peak instability frequency was observed to increase with increasing the outer gas to liquid momentum ratio.

1.2.7 Numerical studies

Within the context of numerical studies of gas-liquid turbulent two-phase flow phenomena, the traditional Reynolds-averaged NavierStokes (RANS) modeling approach could lead to poor predictions of highly unsteady and complex flow phenomena involving vortical structures due to the intrinsic time- or ensemble-averaging of governing equations. Large-eddy simulation can be used to overcome the problems associated with the averaging involved in RANS approach but it may not be sufficient to understand the detailed mechanisms in a high-speed multiphase flow, since small scales still need to be modeled. In this context, direct numerical simulation (DNS) can be a very powerful tool that not only leads to a better understanding of the fluid mechanics involved, but also provides useful databases for the potential development of physical models for liquid breakup and atomization in gas environments.

Many studies have been performed using the above mentioned numerical methods to simulate the interface changes and turbulence in two-phase environments. These studies include planar liquid sheet instability (Stanley et al. [46], Klein et al. [47], Klein [48], Sander & Weigand [49]), cylindrical jet instability (Richards et al. [50], Yoon & Heister [51], Park et al. [52], Menard et al. [53], Pan & Suga [54], Gorokhovski & Hermann [55], Lebas et al. [56], Shinjo & Umermura [57], Chesnel et al. [58]) and swirling or non-swirling annular liquid sheet instabilities (Ibrahim [59] and Siamas et al. [60–62]).

Two-dimensional axisymmetric numerical simulations have been carried out by Ibrahim [59] to study the unsteady, turbulent, swirling two-phase flow field inside pressure swirl atomizers using the volume of fluid (VOF) method. In the same study, the linear and nonlinear asymmetric instability analyses are carried out to study the primary atomization of annular liquid sheets and liquid jets emanating from the pressure swirl (simplex) atomizer, prefilming airblast atomizer, and plain orifice pressure atomizer using a perturbation method with the initial amplitude of the disturbance as the perturbation parameter. For annular liquid sheets, he found that the breakup length is reduced by an increase in the liquid Weber number, initial disturbance amplitude and the inner and outer gas-liquid velocity ratios (in consistent with previous experiments). His numerical results also indicate that air swirl not only promotes the instability of the annular liquid sheet, but also switches the dominant mode from the axisymmetric mode to a helical mode [59].

An annular liquid jet in a compressible gas medium was examined by Siamas et al. [60] using an Eulerian approach with mixed-fluid treatment. An adapted volume of fluid method combined with a continuum surface force model was used to capture the gas-liquid interface dynamics in this research. It was identified that the liquid-to-gas density and viscosity ratios have opposite effects on the flow field, with the reduced liquid-to-gas density ratio demoting the instability and the reduced liquid-to-gas viscosity ratio promoting the instability characteristics [60].

Siamas et al. [61, 62] used the same numerical methods mentioned above to solve a time-dependent, compressible, swirling annular gas-liquid two-phase flow system. In [61] three-dimensional spatial direct numerical simulation was performed with parallelization of the code based on domain decomposition. The results showed that the flow is characterized by a geometrical recirculation zone adjacent to the nozzle exit and by a central recirculation zone further downstream. The swirling mechanism was known to be responsible for the development of the central recirculation zone downstream of the nozzle, a feature which is absent in annular gas-liquid non-swirling jet flow [61].

In [62], the dynamics of annular gas-liquid two-phase swirling jets was examined by means of direct numerical simulation and proper orthogonal decomposition. The effects of liquid-to-gas density ratio on the flow development was examined, and it was found that the higher density ratio case is more vortical with larger spatial distribution of the liquid, in agreement with linear theories. In the lower density ratio case, both the central and the geometrical recirculation zones, which were observed in the earlier studies, were captured while only one central recirculation zone was evident at the higher density ratio. The results also indicated the formation of a precessing vortex core at the high density ratio, indicating that the precessing vortex core development is dependent on the liquid-to-gas density ratio of the two-phase flow, apart from the swirl number alone [62].

Chapter 2

Computational modeling

In this study computational models have been used to solve the unsteady, two-dimensional axisymmetric Navier-Stokes equations for flow of an incompressible fluid through annular nozzle and the exiting transient jet through orifice. Use will be made of the previously developed unsteady multidimensional code with the finite-volume solver of the Navier-Stokes equations for liquid streams and adjacent gas, boundary-fitted gridding scheme, and level-set method for liquid/gas interface tracking applied by Dabiri et al. [63, 64]; Dabiri [65]. We will use the model capability to examine the annular jet flows during start-up transition, typical of intermittent combustors, predicting jet formation and resulting axisymmetric instabilities that can lead to stream break-up.

In this chapter the numerical methods that have been used to find solutions to the Navier-Stokes flow in later chapters will be discussed. This includes the discretization of convection diffusion problem, the coupling of velocity-pressure through SIMPLE algorithm and the application of the level-set method to track the liquid-gas interface.

2.1 Governing equations

The general form of the continuity (mass conservation) equation is:

$$\frac{\partial \rho}{\partial t} + \mathbf{u} \cdot \nabla \rho + \rho \nabla \cdot \mathbf{u} = 0 \tag{2.1}$$

The first two terms could be combined to make the material (Lagrangian) derivative of the density

$$\Rightarrow \quad \frac{D\rho}{Dt} + \rho \nabla \cdot \mathbf{u} = 0 \tag{2.2}$$

Although both fluids (liquid and gas) are considered to be incompressible in this research, one might think that since there is a density variation across the interface over time, the general continuity equation (2.1) should be used, which takes care of the density variation in whole domain. However, we know that the density of either zones (gas or liquid) does not change, even though the interface location is altered over time. Therefore, from the definition of the material derivative (time derivative of a variable following a particle), it is concluded that the first term in Eqn. (2.2) is identically zero and the incompressible form of the continuity equation is obtained:

$$\nabla \cdot \mathbf{u} = 0 \tag{2.3}$$

The equations of fluid motion are Navier-Stokes equations which in an incompressible flow and considering the viscous and surface tension forces and neglecting the gravitational forces have a conservative form as follows:

$$\frac{\partial (\rho \mathbf{u})}{\partial t} + \nabla \cdot (\rho \mathbf{u}\mathbf{u}) = -\nabla p + \nabla \cdot (2\mu \mathbf{D}) + \mathbf{F} \tag{2.4}$$

where $\mathbf{D}$ is the strain rate tensor,

$$\mathbf{D} = \frac{1}{2}\left[(\nabla\mathbf{u}) + (\nabla\mathbf{u})^T\right] \tag{2.5}$$

and $\mathbf{F}$ is the surface tension force per unit volume

$$\mathbf{F} = -\sigma\kappa\delta(d)\vec{\mathbf{n}} \tag{2.6}$$

In the equations above, $\mathbf{u}$ is the velocity field, ρ and μ are the density and viscosity of the fluid, respectively, p is the pressure field, σ is the surface tension coefficient, κ is the surface curvature, $\delta(d)$ is the Dirac delta function and $\vec{\mathbf{n}}$ is the unit vector normal to the interface. Notice that the entire strain rate tensor has been used in the viscous diffusion term because the viscosity varies near the interface zone, and this will introduce extra terms in the momentum equations in each direction, which include the viscous variation effects. This will be discussed later in this section.

2.1.1 Navier-Stokes in curvilinear orthogonal coordinates

Simulation of flow in complex geometries, such as flow through a nozzle with curved corners, can be handled by implementing a boundary-fitted grid. The axisymmetric annular jet flow in this research is studied using the boundary-fitted grid. In this problem, an orthogonal grid is used to discretize the domain because orthogonality of the grid leads to many of the terms in the metric tensor being zero which makes the calculation faster. Also, it will offer more accuracy in the calculation of the normal fluxes.

In this study, the Laplace equation corresponding to the irrotational axisymmetric flow in the same geometry has been solved to generate the desired bounday-fitted grid. Therefore, the potential function and stream function of the theoretical axisymmetric potential flow are used as the orthogonal-coordinates system. This choice of coordinates will increase the accuracy since the flow far from the boundaries and regions of separated flow is irrotational and thus, closely parallel to the grid. For detailed descriptions on generation of the boundary-fitted grid see Dabiri (2009) [65].

The momentum equation for an incompressible flow with constant properties is

$$\frac{\partial(\rho\mathbf{u})}{\partial t} + \nabla\cdot(\rho\mathbf{u}\mathbf{u}) = -\nabla p + \mu\nabla^2\mathbf{u} + \mathbf{F} \tag{2.7}$$

In order to solve the momentum equation with the finite-volume method, each component of the equation should be written in the form of a convection-diffusion equation of a scalar field as follows

$$\frac{\partial(\rho\varphi)}{\partial t} + \nabla\cdot(\rho\mathbf{u}\varphi) = \Gamma\nabla^2\varphi + S \tag{2.8}$$

In cartesian coordinates, the jth component of the momentum equation is already in the form of a convection-diffusion equation for $\varphi = u_j$, with $-\nabla p$ acting as the source term, S, and dynamic viscosity μ as the diffusion coefficient, Γ.

In a curvilinear coordinate system $(x_1,\, x_2,\, x_3)$, due to dependency of the base unit vectors on position, additional terms come into the equation. Considering the jth component of the momentum equation, we have

$$\left[\frac{\partial\rho\mathbf{u}}{\partial t}\right]\cdot\hat{e}_j + [\nabla\cdot(\rho\mathbf{u}\mathbf{u})]\cdot\hat{e}_j = [-\nabla p]\cdot\hat{e}_j + \left[\mu\nabla^2\mathbf{u}\right]\cdot\hat{e}_j + [\mathbf{F}]\cdot\hat{e}_j \tag{2.9}$$

where $\hat{e}_j$ is the unit vector in j-direction. Each term of the equation can be rewritten as

$$\left[\frac{\partial\rho\mathbf{u}}{\partial t}\right]\cdot\hat{e}_j = \frac{\partial\rho u_j}{\partial t} \tag{2.10}$$

$$[\nabla\cdot(\rho\mathbf{u}\mathbf{u})]\cdot\hat{e}_j = \nabla\cdot(\rho\mathbf{u}u_j) + \rho U_j \tag{2.11}$$

$$[-\nabla p] \cdot \hat{e}_j = -\frac{1}{h_j}\frac{\partial p}{\partial x_j} \tag{2.12}$$

$$\left[\nabla^2 \mathbf{u}\right] \cdot \hat{e}_j = \nabla^2 u_j + B_j \tag{2.13}$$

$$[\mathbf{F}] \cdot \hat{e}_j = F_j \tag{2.14}$$

where U_j is

$$U_j = \sum_{k=1}^{3} \frac{u_k}{h_k h_j}\left(u_j \frac{\partial h_j}{\partial x_k} - u_k \frac{\partial h_k}{\partial x_j}\right) \tag{2.15}$$

and for $j = 1$, B_1 is

$$\begin{aligned} B_1 \quad = \quad & \frac{1}{h_1 h_2 h_3}\left[\frac{\partial}{\partial x_1}\left(\frac{h_3}{h_1}u_2\frac{\partial h_1}{x_2} + \frac{h_2}{h_1}u_3\frac{\partial h_1}{\partial x_3}\right)\right. \\ & \left. -\frac{\partial}{\partial x_2}\left(\frac{h_3}{h_2}u_2\frac{\partial h_2}{x_1}\right) - \frac{\partial}{\partial x_3}\left(\frac{h_2}{h_3}u_3\frac{\partial h_3}{x_1}\right)\right] \\ & +\frac{G_{12}}{h_1 h_2}\frac{\partial h_1}{\partial x_2} + \frac{G_{13}}{h_1 h_3}\frac{\partial h_1}{\partial x_3} - \frac{G_{22}}{h_1 h_2}\frac{\partial h_2}{\partial x_1} - \frac{G_{33}}{h_1 h_3}\frac{\partial h_3}{\partial x_1} \end{aligned} \tag{2.16}$$

and here, $\mathbf{G} = \nabla \mathbf{u}$. F_j in equation (2.14) is the jth component of the capillary forces.

Therefore, equation (2.9) can be rewritten as

$$\frac{\partial(\rho u_j)}{\partial t} + \nabla \cdot (\rho \mathbf{u} u_j) = \Gamma \nabla^2 u_j + S \tag{2.17}$$

where the source term is

$$S = -\frac{1}{h_j}\frac{\partial p}{\partial x_j} - \rho U_j + \mu B_j + F_j \tag{2.18}$$

In the above formulation h_js are the scale factors for the orthogonal curvilinear coordinate $(x_1,\, x_2,\, x_3)$ [66].

2.1.2 Finite-Volume formulation for variable properties

The viscous stress term in the Navier-Stokes equations for an incompressible flow with variable properties in the cartesian coordinates can be written as follows

$$
\begin{aligned}
&\left[\nabla \cdot (\mu(\nabla \mathbf{u} + \nabla \mathbf{u}^T))\right] = \\
&= \frac{\partial}{\partial x}\left[2\mu\frac{\partial u}{\partial x}\right] + \frac{\partial}{\partial y}\left[\mu\Big(\frac{\partial u}{\partial y} + \frac{\partial v}{\partial x}\Big)\right] + \frac{\partial}{\partial z}\left[\mu\Big(\frac{\partial u}{\partial z} + \frac{\partial w}{\partial x}\Big)\right] \\
&= \nabla \cdot (\mu \nabla u) + \frac{\partial}{\partial x}\left(\mu\frac{\partial u}{\partial x}\right) + \frac{\partial}{\partial y}\left(\mu\frac{\partial v}{\partial x}\right) + \frac{\partial}{\partial z}\left(\mu\frac{\partial w}{\partial x}\right) \\
&= \nabla \cdot (\mu \nabla u) + \mu \nabla \cdot \mathbf{u} + \frac{\partial \mu}{\partial x}\frac{\partial u}{\partial x} + \frac{\partial \mu}{\partial y}\frac{\partial v}{\partial x} + \frac{\partial \mu}{\partial z}\frac{\partial w}{\partial x}
\end{aligned} \tag{2.19}
$$

The second term is zero due to incompressibility of the fluid. If we write the momentum equation in the following form, the last three terms should be included in the source term S.

$$
\frac{\partial(\rho u)}{\partial t} + \nabla \cdot (\rho \mathbf{u} u) = \nabla \cdot (\mu \nabla u) + S \tag{2.20}
$$

2.2 Numerical methods

A finite-volume discretization on a staggered grid has been considered in this study. The conservation equations come from the balance in the flux going in and coming out of the control volume. Therefore, accurate calculation of these fluxes is of great importance. Third-order accurate QUICK scheme has been used for spatial discretization and the Crank-Nicolson scheme has been used for time-marching treatment in this research. SIMPLE algorithm has been used for velocity-pressure coupling. In this section these algorithms will be discussed briefly.

2.2.1 QUICK discretization

The Quadratic Upwind Interpolation for Convective Kinetics (QUICK) was first introduced by Leonard [67]. The method is based on a three-point upstream-weighted quadratic interpolation technique for cell face values on a staggered grid. Leonard [67] has shown that this scheme has a better accuracy than central difference scheme while retains the transportiveness property of the upwind scheme. The face value of the scalar quantity ϕ is obtained from a quadratic function passing through two bracketing nodes (on each side of the face) and a node on the upstream side (Figure. 2.1).

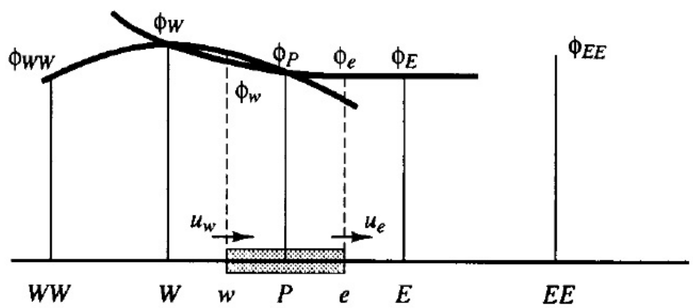

Figure 2.1: Quadratic profiles used in QUICK scheme

A uniform grid spacing is used here for simplicity but the concept can be easily extended to nonuniform grids. The value of ϕ at the interface of the cell is calculated by fitting a quadratic polynomial to three consecutive nodes: the two nodes located at either side of the surface and another node on the upstream side. For example, when $u_w > 0$ and $u_e > 0$ a quadratic fit through WW, W and P is used to evaluate ϕ_w, and a further quadratic fit through W, P and E to calculate ϕ_e. It can be shown that for a uniform grid the value of ϕ at the cell face between two bracketing nodes i and $i-1$ and upstream node $i-2$ is given by the following formula [67]:

$$\phi_{face} = \frac{6}{8}\phi_{i-1} + \frac{3}{8}\phi_i - \frac{1}{8}\phi_{i-2} \quad (2.21)$$

Using this formula the value of the scalar ϕ at the west cell face can be written as:

$$\phi_w = \begin{cases} \frac{6}{8}\phi_W + \frac{3}{8}\phi_P - \frac{1}{8}\phi_{WW} & \text{for } u_w > 0 \\ \frac{6}{8}\phi_P + \frac{3}{8}\phi_W - \frac{1}{8}\phi_E & \text{for } u_w < 0 \end{cases} \tag{2.22}$$

and a similar relation for the east cell face value ϕ_e.

There have been several papers addressing the practical implementation of the QUICK scheme, but among them Hayase et al. [68] presented a consistent formulation of QUICK scheme which is more stable and also fast converging which will be used here. In this formulation, the interpolated values of the scalar function are rearranged as

$$\phi_w = \begin{cases} \phi_W + \frac{1}{8}[3\phi_P - 2\phi_W - \phi_{WW}] & \text{for } u_w > 0 \\ \phi_P + \frac{1}{8}[3\phi_W - 2\phi_P - \phi_E] & \text{for } u_w < 0 \end{cases} \tag{2.23}$$

and

$$\phi_e = \begin{cases} \phi_P + \frac{1}{8}[3\phi_E - 2\phi_P - \phi_W] & \text{for } u_e > 0 \\ \phi_E + \frac{1}{8}[3\phi_P - 2\phi_E - \phi_{EE}] & \text{for } u_e < 0 \end{cases} \tag{2.24}$$

The terms in the brackets are treated as source terms using the values from previous iteration. Hence, the values of ϕ at interface are given as an upwind estimation plus a corrective source term. The advantage of this approach is that the main coefficients in the discretized equation are positive and satisfy the requirements for conservativeness, boundedness and transportiveness. The QUICK scheme is third order accurate.

2.2.2 SIMPLE algorithm

The acronym SIMPLE stands for Semi-Implicit Method for Pressure-Linked Equations. The algorithm was originally put forward by Patankar and Spalding [69] and is essentially a guessand-correct procedure for the calculation of pressure on the staggered grid arrangement.

To initiate the SIMPLE calculation process a pressure field p^* is guessed. Discretized momentum equations are solved using the guessed pressure field to yield velocity components u^* and v^*. Then a pressure correction equation which represents the continuity equation is solved to give the pressure correction variable p'. Once the pressure correction field is known, the correct pressure field and velocity components are obtained.

The SIMPLE algorithm gives a method of calculating pressure and velocities. The method is iterative, and when other scalars are coupled to the momentum equations the calculation needs to be done sequentially. The sequence of operations in a CFD procedure which employs the SIMPLE algorithm is given in Figure 2.2. The equations that need to be solved in each step are also shown here.

2.3 Interface tracking approach

Tracking the interface between two phases and modeling its physics such as surface tension is of great importance in studying multiphase flows. Several methods have been developed to handle the difficulties in interfacial modeling. The surface marker method or the front-tracking method explicitly tracks the position of the interface by updating the position of marker points on it. For example, Tryggvason and Unverdi [71] and Glimm et al. [72] used this method to study Rayleigh-Taylor instabilities. Popinet and Zaleski [73] did an accurate balance of surface tension forces on a finite volume method by explicit tracking of the interface. The method was applied only for two-dimensional calculations because of the geometrical complexity appearing in the three-dimensional calculation. The drawback of the front-tracking method is the difficulty in capturing the topological changes in the phases, such as breakup or coalescence of liquid drops and specially in three-dimensional calculations

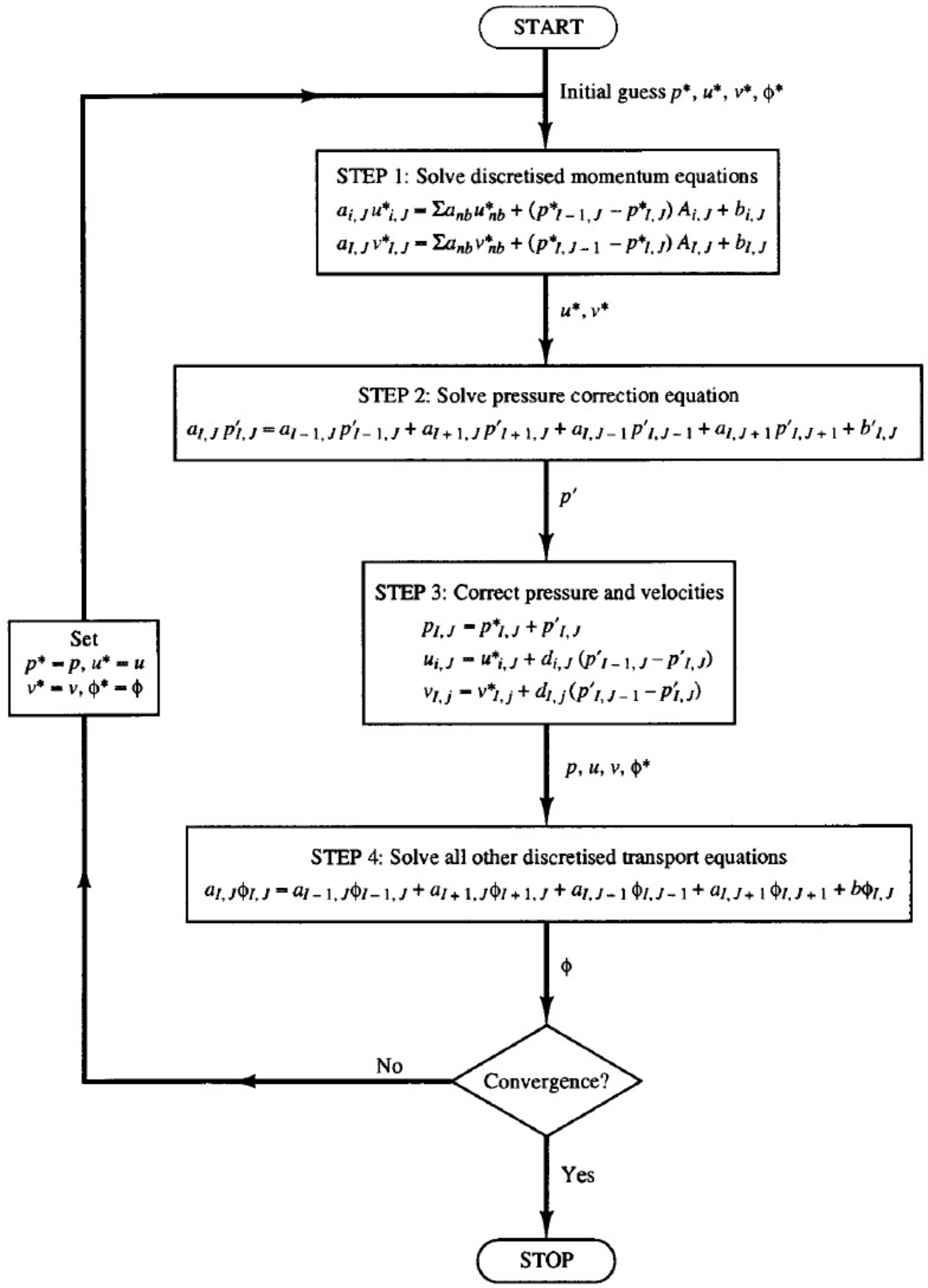

Figure 2.2: The SIMPLE algorithm flow chart [70].

[65].

In the limit of inviscid flow, the interface could be modeled as a vortex sheet with zero thickness. Rangel and Sirignano [27] performed a nonlinear analysis of temporal instability of a liquid sheet using this idea. From the momentum equation on sides of the interface and a balance of interfacial forces, they derived an equation for the evolution of circulation on the interface for a case with density discontinuity and surface tension. The velocity field is also found by the Savart law from the vorticity [65].

Volume of Fluid (VOF) is another method developed to treat the multiphase flows. In this method, a scalar parameter in each discretized cell is defined as the volume fraction of cell filled with one of the phases. This scalar is updated in time by considering the convection from and to neighboring cells. A review of different methods of interface tracking and surface tension modeling is done by Scardovelli and Zaleski [74].

In this work, the level-set method is employed to track the interface and model its physics. The level-set method has been developed by Osher and coworkers (see Zhao et al. [75], Sussman et al. [76], and Osher et al. [77]). In this method, the interface between two phases is defined as the zero level set of a scalar function called level-set function and denoted by θ here. The level-set function is defined over the whole computational domain as a signed distance function from the interface, i.e., it has positive values on one side of the interface (gas phase), and negative values on the other side (liquid phase) and the magnitude of the level-set at each point in the computational domain is equal to the distance from that point to the interface.

2.3.1 Level-set method

The level-set function θ is defined as a smooth distance function allowing us to give the interface a thickness fixed in time. Density, viscosity and surface tension all depend on the level set function being a distance function. In this algorithm, the interface Γ is the zero level set of θ,

$$\Gamma = \{\mathbf{x} \,|\, \theta(\mathbf{x}, t) = 0\}$$

We take $\theta < 0$ in the liquid region and $\theta > 0$ in the gas region. Therefore we have

$$\theta(\mathbf{x}, t) \begin{cases} > 0 & \text{if } \mathbf{x} \in \text{the gas} \\ = 0 & \text{if } \mathbf{x} \in \Gamma \\ < 0 & \text{if } \mathbf{x} \in \text{the liquid} \end{cases} \tag{2.25}$$

By virtue of the boundary conditions $\mathbf{u}$ is continuous across the interface. Since the interface moves with the fluid particles, the evolution of θ is then given by

$$\frac{\partial \theta}{\partial t} + \mathbf{u} \cdot \nabla \theta = 0 \tag{2.26}$$

Equation (2.26) is called the Level-set equation. It is obvious that, if the initial distribution of the level-set is a signed distance function, after a finite time of being convected by a nonuniform velocity field, it will not remain a distance function. Therefore, we need to re-initialize the level-set function in such a way that it will be a distance function (with property of $|\nabla \theta| = 1$) without changing the zero level-set (position of the interface). Suppose $\theta_0(x)$ is the level-set distribution after some time step and is not exactly a distance function. This can be re-initialized to a distance function by solving the following partial differential equation (Sussman et. al. [76]):

$$\frac{\partial d}{\partial \tau} = \text{sign}(\theta)(1 - |\nabla d|) \tag{2.27}$$

with initial condition

$$d(\mathbf{x}, 0) = \theta_0(\mathbf{x})$$

where τ is a psuedo time. The steady solutions of Equation (2.27) are distance functions with property $|\nabla d| = 1$. Furthermore, since $\text{sign}(0) = 0$, then $d(\mathbf{x}, t)$ has the same zero level-set as $\theta(\mathbf{x})$. Therefore, we simply solve Equation (2.27) to steady state and then replace $\theta(\mathbf{x})$ by $d(\mathbf{x}, \tau_{\text{steady}})$.

The $5th$ order accurate Weighted Essential Non-Oscillatory (WENO) scheme of Jiang & Peng [78] has been used in this research to solve the re-initialization equation (2.27) in every iteration.

For the multiphase flow, if we define the Ω_l and Ω_g to be the domain occupied by liquid and gas, respectively, we can write the Navier-Stokes equations in each of the domains as,

$$\rho_l \frac{D\mathbf{u}_l}{Dt} = -\nabla p_l + 2\mu_l \nabla \cdot \mathbf{D}_l \ , \quad \nabla \cdot \mathbf{u}_l = 0 \ , \quad \mathbf{x} \in \Omega_l \tag{2.28}$$

$$\rho_g \frac{D\mathbf{u}_g}{Dt} = -\nabla p_g + 2\mu_g \nabla \cdot \mathbf{D}_g \ , \quad \nabla \cdot \mathbf{u}_g = 0 \ , \quad \mathbf{x} \in \Omega_g \tag{2.29}$$

where $\mathbf{D}$ is the strain rate tensor and subscripts g and l denote the gas and liquid phase, respectively. The boundary conditions on the liquid-gas interface are:

$$(2\mu_l \mathbf{D}_l - 2\mu_g \mathbf{D}_g) \cdot \mathbf{n} = (p_l - p_g - \sigma\kappa)\mathbf{n} \quad \text{and} \quad \mathbf{u}_l = \mathbf{u}_g \ , \quad \mathbf{x} \in \Gamma \tag{2.30}$$

where Γ is the liquid-gas interface, $\mathbf{n}$ is the normal unit vector on the interface towards the gas phase, $\kappa = \nabla \cdot \mathbf{n}$ is the curvature of the interface and σ is the surface tension coefficient.

The unit normal on the interface $\mathbf{n}$, drawn from the liquid into the gas, and the curvature of the interface κ can easily be expressed in terms of $\theta(\mathbf{x}, t)$:

$$\vec{\mathbf{n}} = \left. \frac{\nabla\theta}{|\nabla\theta|} \right|_{\theta=0} \quad \text{and} \quad \kappa = \nabla \cdot \vec{\mathbf{n}} = \nabla \cdot \left. \left(\frac{\nabla\theta}{|\nabla\theta|} \right) \right|_{\theta=0} \tag{2.31}$$

Expanding equation (2.31) in Cartesian coordinates leads to the following equation for the curvature of the interface in a 2-D problem (x, y):

$$\kappa = -\frac{\theta_y^2 \theta_{xx} - 2\theta_x \theta_y \theta_{xy} + \theta_x^2 \theta_{yy}}{(\theta_x^2 + \theta_y^2)^{3/2}} \tag{2.32}$$

The governing equations for the fluid velocity (Eqns. 2.28 & 2.29) along with their boundary condition (Eqn. 2.30) can be written as a single equation containing both liquid and gas properties in the whole domain, $\Omega = \Omega_l \cup \Omega_g$,

$$\rho(\theta)\frac{D\mathbf{u}}{Dt} = -\nabla p + \nabla \cdot (2\mu(\theta)\mathbf{D}) - \sigma\kappa(\theta)\delta(\theta)\vec{\mathbf{n}} \tag{2.33}$$

Since the density and viscosity are constant in each fluid, they then take on two different values depending on the sign of θ, and we can write

$$\rho(\theta) = \rho_l + (\rho_g - \rho_l)H(\theta) \tag{2.34}$$

and

$$\mu(\theta) = \mu_l + (\mu_g - \mu_l)H(\theta) \tag{2.35}$$

where $H(\theta)$ is the Heaviside function given by

$$H(\theta) = \begin{cases} 0 & \text{if } \theta < 0 \\ \frac{1}{2} & \text{if } \theta = 0 \\ 1 & \text{if } \theta > 0 \end{cases} \tag{2.36}$$

The subscripts g and l in equations (2.34) and (2.35) refer to gas and liquid, respectively.

Therefore, the incompressible flow of a liquid-gas mixture could be treated as an incompressible flow of a variable density fluid with surface tension modeled as a body force per unit volume.

2.3.2 Interface thickness

In order to solve Equation (2.33) numerically we must modify it slightly due to the sharp changes in ρ and μ across the interface front and also due to the numerical difficulties presented by the Dirac delta function $\delta(\theta)$ contained in the surface tension force $\mathbf{F}$. To alleviate these problems we shall give the interface a fixed thickness that is proportional to the spatial mesh size. This allows us to replace $\rho(\theta)$ and $\mu(\theta)$ by a smoothed density and viscosity which we denote as $\rho_\epsilon(\theta)$ and $\mu_\epsilon(\theta)$ and is given by

$$\rho_\epsilon(\theta) = \rho_l + (\rho_g - \rho_l)H_\epsilon(\theta) \tag{2.37}$$

and

$$\mu_\epsilon(\theta) = \mu_l + (\mu_g - \mu_l)H_\epsilon(\theta) \tag{2.38}$$

with smoothed Heaviside function

$$H_\epsilon(\theta) = \begin{cases} 0 & \text{if } \theta < -\epsilon \\ \frac{1}{2}(\frac{\theta+\epsilon}{\epsilon}) + \frac{1}{2\pi}\sin(\frac{\pi\theta}{\epsilon}) & \text{if } |\theta| \le \epsilon \\ 1 & \text{if } \theta > \epsilon \end{cases} \tag{2.39}$$

where ϵ represents the half thickness of the interface and has the value of $1.5\Delta x$ where Δx is the cell size. The plot illustrating the variation of $H_\epsilon(\theta)$ across the three interface cells is given in Figure 2.3. This Heaviside function corresponds to a Delta function that can be used to evaluate the force caused by the surface tension:

$$\delta_\epsilon(\theta) = \frac{dH_\epsilon}{d\theta} = \begin{cases} \frac{1}{2\epsilon}\left[1 + \cos(\frac{\pi\theta}{\epsilon})\right] & \text{if } |\theta| \le \epsilon \\ 0 & \text{otherwise} \end{cases} \tag{2.40}$$

The variation of the modified Delta function across the interface cells is plotted in Figure 2.4. It should be noticed that introduction of the modified Heaviside and Delta functions, allows the density and viscosity to vary smoothly across the interface cells, and is not in consistent with our earlier assumption that the density is constant within each liquid or gas zone. This might result in some minor errors which are negligible in this context.

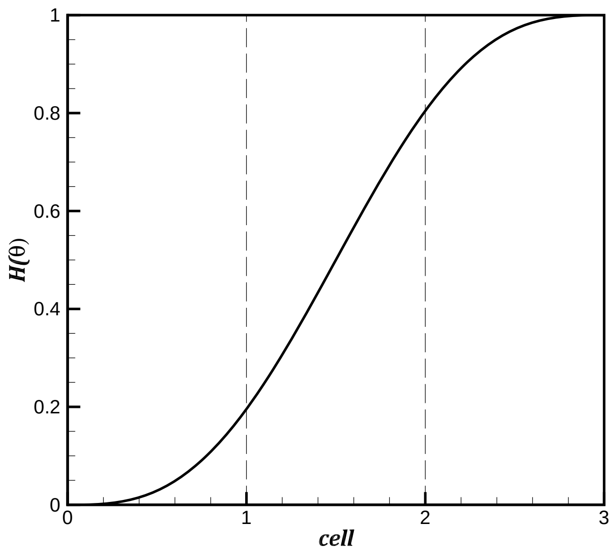

Figure 2.3: The smoothed Heaviside function variation across the interface

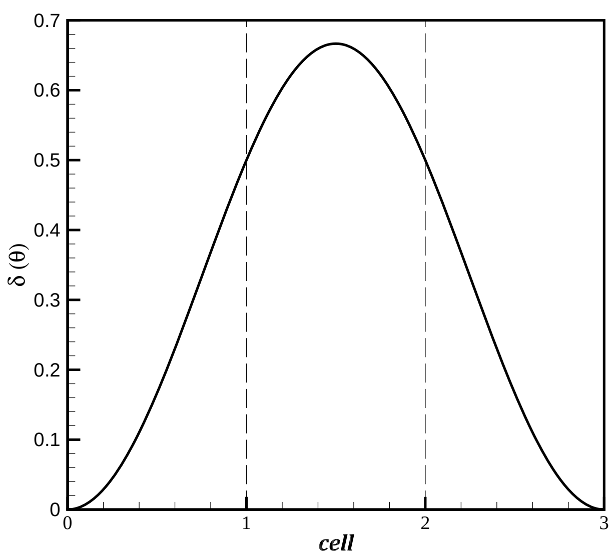

Figure 2.4: The modified Delta function variation across the interface

2.4 Computational domain

The computational domain and the grid system that consists of an annular nozzle initially full of liquid and a gas chamber initially filled with quiescent gas is demonstrated in Figure 2.5. The computational gird consists of an orthogonal curvilinear coordinate system based on potential flow solutions in the nozzle and a Cartesian coordinate system in the external flow (gas zone).

A non-uniform mesh has been used with more grid points clustered inside the nozzle and near the nozzle exit and coarsened with increasing downstream distance and radial position. There are $1,140$ and 410 mesh points in the x and r-direction, with $16,000$ mesh points lying inside the nozzle (400×40) and $303,400$ nodes in the external gas chamber (740×410). The finest grid cells are at the nozzle exit and they are kept uniform for some distance downstream of the nozzle exit plane. The dimensions of these cells are $\Delta x = \Delta r = 1.5\ \mu m$. A time step of $\Delta t = 10\ ns$ ($0.01\ \mu s$) is chosen for the time marching computations.

As is shown in Figure 2.5, the outer nozzle diameter is indicated by D while the inner diameter will be shown by d. The domain size and all other length scales will be represented

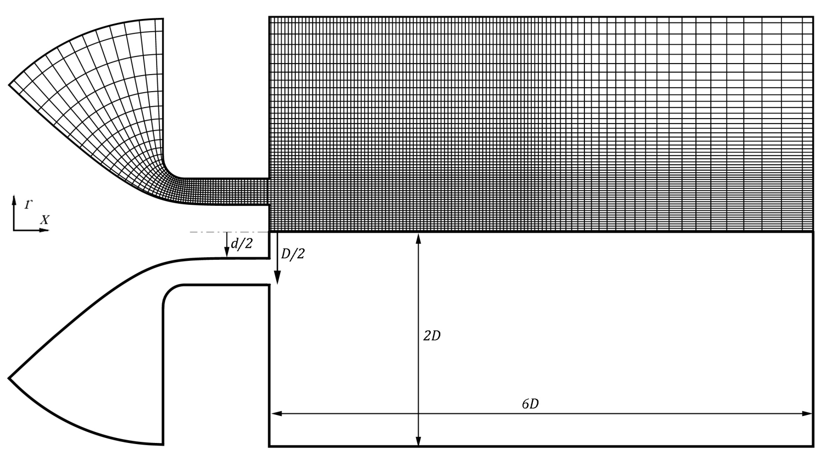

Figure 2.5: Physical domain and orthogonal grid for annular nozzle and gas chamber for full jet (flow from left to right).

Fluid Properties	Liquid (Kerosene)	Gas (air)
Dynamic viscosity, μ $(kg/m.s)$	2.7×10^{-3}	1.8×10^{-5}
Density, ρ (kg/m^3)	804	38.4 (at 30 atm)
Surface tension coefficient, σ (N/m)	0.028	–
Maximum jet velocity, U (m/s)	100	–

Table 2.1: Fluid properties

with respect to the outer nozzle diameter in this report and, as has been illustrated in the figure, the length of the rectangular domain downstream of the nozzle exit plane is $6D$ whereas its height from the centerline is twice the diameter. The nozzle outer diameter is chosen to be $D = 500$ μm ($R = 250$ μm) in this research, and the inner diameter will be obtained based on the inner to outer diameter ratio (d/D). The length of the horizontal part of the nozzle channel before reaching the nozzle exit plane is equal to the nozzle diameter $L/D = 1$. Further discussion about the domain size and the reason for choosing the mentioned values will be presented in the code verification section.

The flow properties are summarized in Table 2.1. Kerosene (paraffin) is used in this research as the injected liquid, and air at high pressure (30 atm) is considered as the surrounding gas. The highest velocity that the liquid jet can reach at the nozzle exit is considered to be 100 m/s. It should be noted that the tabulated values are only for the base case; for other cases with different Reynolds and Weber numbers, the liquid properties will be derived from the corresponding dimensionless parameter. The gas density and viscosity might also vary according to the density and viscosity ratios, respectively, based on the values that will be calculated for the liquid phase.

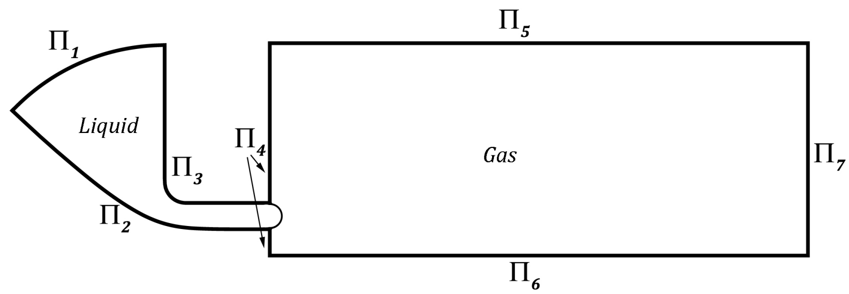

Figure 2.6: Geometry of the computational domain and its boundaries.

2.5 Boundary and initial conditions

The boundaries of the computational domain, which are to be described in this section, are shown in Figure 2.6. The initial conditions are zero velocity and zero pressure everywhere (in both gas and liquid zones); and the initial position of the interface between the liquid and the gas phase is a semi-circle at the nozzle exit, as is shown in Figure 2.6.

The plenum pressure upstream in the nozzle (at Π_1) is set to increase exponentially over a

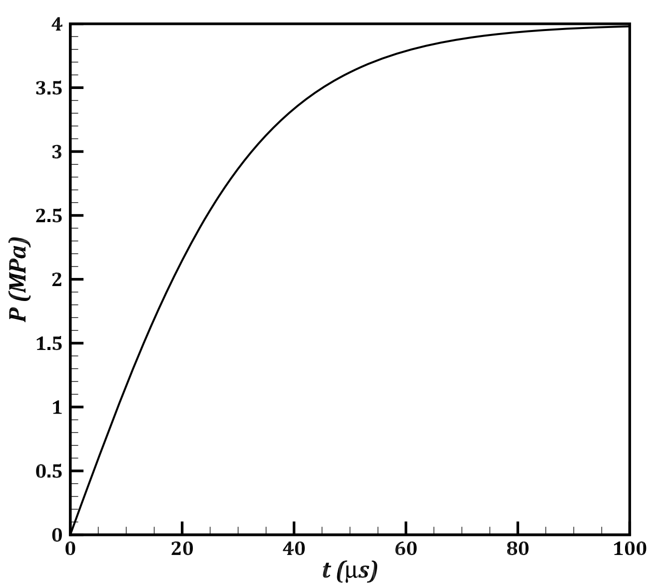

Figure 2.7: Variation of the upstream nozzle pressure with time.

period of 100 μs until a prescribed maximum pressure (4 MPa) is reached. The plenum pressure drives the flow and the mass flux; the exit velocity of the jet increase with the plenum pressure. At the end of start-up process, the maximum jet velocity reaches 100 m/s (based on a simple calculation from the Bernouli's relation $U = \sqrt{2p/\rho_l}$). The upstream boundary (Π_1) is then time dependent and its variation in time is given in Figure 2.7.

Π_2 and Π_3 in Figure 2.6 are the inner and outer sides of the nozzle walls, respectively, and Π_4 is the vertical wall of the gas chamber, where no-slip condition is imposed on all of these boundaries. Π_6 is the axis of symmetry of the geometry and symmetric condition is applied at that centerline. For Π_5 boundary a constant zero pressure is prescribed, and for the downstream boundary Π_7 zero material derivative of the fluid velocities is considered. A summary of the boundary conditions mentioned above are presented mathematically in Table 2.2. In this report the axial velocity component (in x-direction) will be defined as u and the radial velocity component as v.

Boundary	**Condition**	**formulation**
Π_1	time dependent upstream pressure	$p = 4 \times 10^6 \tanh(3 \times 10^4 t)$
Π_2	wall	$u = 0,\ v = 0$
Π_3	wall	$u = 0,\ v = 0$
Π_4	wall	$u = 0,\ v = 0$
Π_5	constant pressure	$p = 0$
Π_6	axis of symmetry	$\frac{\partial}{\partial r} = 0,\ v = 0$
Π_7	zero material derivative downstream	$\frac{D}{Dt} = 0$

Table 2.2: Boundary conditions

2.6 Dimensional analysis

The main purpose of this study is to investigate the growth rate of instabilities on the liquid/gas interface and the dominant wave length corresponding to that maximum growth rate. The most important parameters that effect the instability growth rate ω could be written as,

$$\omega = f(\rho_l, \rho_g, \mu_l, \mu_g, d \text{ (or } h), D, \lambda \text{ (or } k), U, \sigma) \tag{2.41}$$

where ρ and μ are the density and viscosity, respectively; and the subscripts l and g stand for liquid and gas phase, respectively. d is the inner diameter of the nozzle annulus, h is the annular liquid sheet thickness and D is the outer diameter of the nozzle. λ is the wave length of the instabilities on the liquid/gas interface, $k = 2\pi/\lambda$ is the instabilities wave-number, U is the maximum jet velocity at nozzle exit and σ is the surface tension coefficient. Using dimensionless parameters, Equation (2.41) can be reduced to the following form

$$\frac{\omega}{kU} = \Phi\big(\frac{\rho_g}{\rho_l}, \frac{\mu_g}{\mu_l}, \frac{d}{D} \text{ (or } \frac{h}{D}), \frac{\lambda}{D} \text{ (or } kh), \frac{\rho_l U d_h}{\mu_l}, \frac{\rho_l U^2 d_h}{\sigma}\big) \tag{2.42}$$

where in this equation d_h is the hydraulic diameter of the annular jet. For an annular jet the hydraulic diameter would be twice the sheet thickness, $d_h = 2h = D - d$. The last two dimensionless parameters in (2.42) are the Reynolds number and the Weber number (based on the liquid properties), respectively.

It is also useful to write Equation (2.33) in dimensionless form. The following dimensionless variables are used for non-dimensionalization:

$$\begin{aligned} x^* &= \frac{x}{d_h}, \qquad \mathbf{u}^* = \frac{\mathbf{u}}{U}, \qquad t^* = \frac{tU}{d_h} \\ p^* &= \frac{p}{\rho_l U^2}, \qquad \rho^* = \frac{\rho}{\rho_l}, \qquad \mu^* = \frac{\mu}{\mu_l} \end{aligned} \tag{2.43}$$

where the asterisks denote dimensionless variables. Substitution of these variables into Equation (2.33) and dropping the asterisks we obtain

$$\frac{\partial \mathbf{u}}{\partial t} + \mathbf{u} \cdot \nabla \mathbf{u} = -\frac{\nabla p}{\rho(\theta)} + \frac{1}{\rho(\theta)} \left(\frac{1}{\mathrm{Re}} \nabla \cdot (2\mu(\theta)\mathbf{D}) - \frac{1}{\mathrm{We}} \kappa(\theta)\delta(\theta)\vec{\mathbf{n}} \right) \tag{2.44}$$

The density and viscosity now become

$$\rho(\theta) = \eta + (1 - \eta)H(\theta) \quad \text{and} \quad \mu(\theta) = \zeta + (1 - \zeta)H(\theta) \tag{2.45}$$

where $H(\theta)$ in here is the heaviside function as introduced earlier. The dimensionless groups used in Eqns. (2.44 & 2.45) are the density ratio,

$$\eta = \frac{\rho_l}{\rho_g} \tag{2.46}$$

the viscosity ratio,

$$\zeta = \frac{\mu_l}{\mu_g} \tag{2.47}$$

the Reynolds number,

$$Re = \frac{\rho_l U d_h}{\mu_l} \tag{2.48}$$

and the Weber number,

$$We = \frac{\rho_l U^2 d_h}{\sigma} \tag{2.49}$$

In order to keep the convention in this research, the gas to liquid density and viscosity ratios will be used, which are the reciprocal of η and ζ as defined above. So, the important dimensionless parameters that are to be analyzed in this research are:

$$Re = \frac{\rho_l U d_h}{\mu_l}, \quad We = \frac{\rho_l U^2 d_h}{\sigma}, \quad \hat{\rho} = \frac{\rho_g}{\rho_l}, \quad \hat{\mu} = \frac{\mu_g}{\mu_l}, \quad \hat{d} = \frac{d}{D} \tag{2.50}$$

It should be noted that the Froude number $Fr = U/\sqrt{g d_h}$ in our study is of order of $O(10^3)$, which means that the gravitational forces are negligible compared to the inertial effects; i.e. the gravity can be neglected in our computations.

The range of dimensionless parameters and the cases that are analyzed in this study are written in Table 2.3. In this table, the first column values for each dimensionless parameter

Parameter	Case Values		
Re	$3,000$	**15,000**	$30,000$
We	**30,000**	$6,000$	$150,000$
$\hat{\rho}$	**0.05**	0.1	0.9
$\hat{\mu}$	**0.0066**	0.0001	0.05
$\hat{d}$	**0.8**	0.9	0.7

Table 2.3: Dimensionless parameters' range

correspond to the fluid properties that were given in Table 2.1 for liquid Kerosene and air as gas. The boldface values however, are the base values for each parameter that are held constant in each case, while the rest of the parameters are varied.

As can be seen from Table 2.3, a wide range of values have been chosen for each parameter to clearly show the effect of all important properties. The Reynolds number ranges from $3,000$ which is almost in transient regime up to $30,000$ which is highly turbulent. The Weber number varies from $6,000$ indicating a very large surface tension, up to $150,000$ which corresponds to a very low surface tension case. The density ratio comprises three different orders of magnitude from a very high density difference ($\hat{\rho} = 0.05$) to a value of $\hat{\rho} = 0.9$ indicating an almost like-density liquid and gas. The same story goes on for viscosity ratio; the chosen values include a highly viscous gas ($\hat{\mu} = 0.05$) and an almost inviscid gas with very low viscosity ratio. The diameter ratio contains a very thin liquid sheet ($\hat{d} = 0.9$) resembling an almost planar sheet and a relatively thick liquid sheet with a thickness equal to 0.3 of the outer annulus radius.

As mentioned earlier, $t^* = Ut/D$ is considered as the dimensionless time in this section. Jarrahbashi and Sirignano in [79] found a new dimensionless time for evolution and breakup of cylindrical liquid jet instabilities based on the gas density and liquid viscosity $t_{lg} = \mu_l t/\rho_g D^2$, where D in their case was the liquid jet diameter. It was claimed that this dimensionless time is capable of predicting the dimensional time at which certain flow instabilities, e.g., lobe formations, occur at the interface for different gas densities [79]. The validity of such dimensionless time for the annular liquid jet case (and/or possible modifications for the current geometry) will be investigated in later sections, where the effects of density and viscosity, as well as sheet thickness, are discussed.

2.7 Code verification

The accuracy of the QUICK scheme and SIMPLE algorithm, the implementation of curvilinear coordinates and the level-set formulation have been checked previously for a series of benchmark problems; i.e. cavity flow, flow past a sphere, oscillating drop, and falling drop problems [65]. The code has proven to be accurate and valid in all of the above-mentioned problems. The independency of the numerical results on the grid size and computational domain are evaluated in this section. A valid numerical solution should not depend on neither the size of the mesh nor the domain size.

2.7.1 Grid independency

Figure 2.8 shows the effects of grid resolution on the size of detached ligaments and instabilities on the interface of liquid and gas for mesh sizes equal to 1, 1.5, and 2 μm at 40 μs after the start of injection. It appears in all cases that most of the protrusions on the liquid surface are produced near the tip of the liquid jet as a result of impact of the curled cap on the main stem of the jet. The high velocity difference between the liquid and the stationary gas assist the instabilities to grow and form thin elongated ligaments. The ligaments stretch upstream and when the inertia forces dominate the capillary forces, the ligaments are ruptured and two-dimensional "droplets" are formed. The ligaments formed on the inner side of the annulus are more stretched than the ones on the outer surface.

These pictures show that a coarse grid produces thicker ligaments and larger droplets when

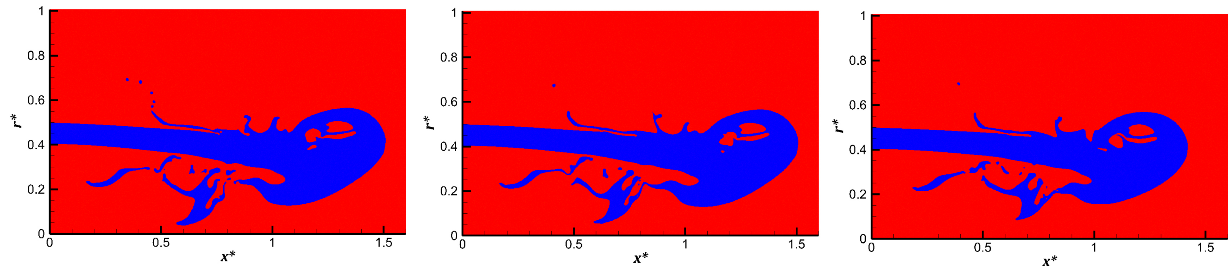

Figure 2.8: Impact of grid-resolution at 40 μs, $Re = 3,000$, $We = 30,000$, $\hat{\rho} = 0.05$, $\hat{\mu} = 0.0066$, $\hat{d} = 0.8$; $\Delta x = \Delta r = 1\ \mu m$ (left), $\Delta x = \Delta r = 1.5\ \mu m$ (center), $\Delta x = \Delta r = 2\ \mu m$ (right).

detached from the jet core. The coarse grid system is also unable to show the elongation of the ligaments effectively, and the liquid segments tear before becoming thin enough. This is clearly shown on the inner side of the liquid sheet, where thicker and less stretched ligaments with more detached large droplets are seen compared to the finer mesh systems (the right tab).

Other than the size of the detached ligaments, the first two cases (i.e., 1 and 1.5 μm) show

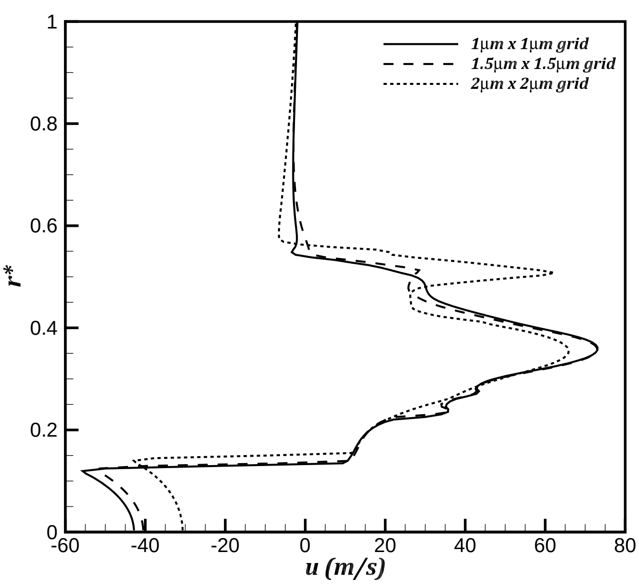

Figure 2.9: Comparison between the axial velocity profiles of the three grid resolutions at 40 μs and $x^* = 1$; $Re = 3,000$, $We = 30,000$, $\hat{\rho} = 0.05$, $\hat{\mu} = 0.0066$, $\hat{d} = 0.8$.

similar behavior in terms of the jet velocity, jet penetration and interface instability; however the ligaments of the 2 μm-case detach from the interface before they curl at the back of the jet head as was observed in the first two cases. The comparison between the axial velocity profile of the three grids at $x^* = 1$ and $t = 40\ \mu s$ is given in Figure 2.9. As can be seen in this figure, the first two cases match almost closely; the coarser grid however, predicts a velocity which is considerably off the correct value. It can also be observed from Figure 2.8 that the coarser mesh results in smaller penetration than the two other cases. In the 2 μm-case the jet cap has not reached $x^* = 1.5$ yet, while at the same time the two finer meshes show that the jet has penetrated beyond $x^* = 1.5$. In other words, the 2 μm resolution seams insufficient to capture the jet penetration behavior during start-up. Therefore, the grid resolution on which the level-set function has been solved coupled with Navier-Stokes equations dictates the break-up length and diameter of the ruptured segments of the liquid jet. The interface thickness based on which the liquid and gas properties have been defined equals to three mesh sizes, i.e., 4.5 μm for 1.5 μm grid resolution. The hydrodynamic stabilities can be predicted well by computation; However, the prediction of the breakup of ligaments and droplets will have quantitative inaccuracies. The grid system with $\Delta x = \Delta r = 1.5\ \mu m$ at the nozzle exit is used for this study.

2.7.2 Domain size independency

After checking the grid resolution and finding the proper grid size which doesn't affect the numerical results, it is important to check whether the results are independent of the size of the domain or not. If the domain is too small, the downstream boundary conditions may affect the computational results and even the code might not be able to converge to any solutions that satisfy both the flow field conditions and the imposed boundary conditions. On the other hand, if the domain size is too big, too much computational effort is wasted in order to solve the flow field at regions that are not of our interest. A good domain is the

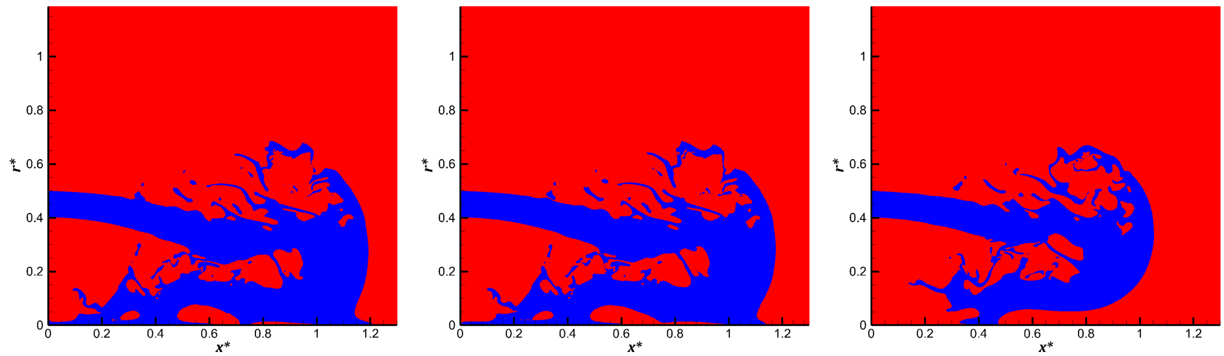

Figure 2.10: Impact of the size of computational domain; $8D$ length and $3D$ height (left), $6D$ length and $2D$ height (center), $4D$ length and $1.5D$ height (right); $t = 40\ \mu s$, $Re = 15,000$, $We = 30,000$, $\hat{\rho} = 0.05$, $\hat{\mu} = 0.0066$, $\hat{d} = 0.8$.

one that doesn't affect the results, while being the least costly in terms of the CPU time.

The independency of the solution on the size of the computational domain (the gas chamber length and height) has been investigated in this section. Three different domain sizes have been considered for this purpose; A large domain $8D$ downstream of the nozzle exit and $3D$ height from the axis of symmetry, a medium domain with $6D$ length and $2D$ height, and a small domain with the downstream boundary at $4D$ and $1.5D$ height. The number of mesh points in both axial and radial directions have been changed accordingly, keeping the mesh size the same $\Delta x = \Delta r = 1.5\ \mu m$ for all of the cases. The results of liquid/gas interface 35 μs after the start-up of injection are compared for the three domains in Figure 2.10.

The unstable structures at the interface for the large and medium computational domains demonstrated in figure 2.10 show similarities in terms of wavelengths and shape of ligaments. The smallest domain however, does not predict the interface shape and position well enough. It could be concluded that the results for any domain larger than the medium domain ($6D \times 2D$) are independent of the size of the domain, and thus, this domain is chosen for the computations in this research.

Chapter 3

Results and discussion

The axysymmetric CFD code mentioned in the previous section has been developed to simulate the flow of a liquid sheet through an annular orifice and the gas chamber during start-up period of injection. The effects on the growth rate and wavelength of the emerging Kelvin-Helmholtz and Rayleigh-Taylor instabilities of various flow parameters are discussed in this section; the Reynolds and Weber number; gas to liquid density and viscosity ratios; and inner to outer liquid sheet diameter ratio. The reasons for the observed differences between the analyzed cases are also investigated in this chapter.

In the following sections, the effects of each of the dimensionless parameters, mentioned above, are discussed. The base parameter values that are used throughout the research were introduced in Table 2.3. The cases that are considered for study are also mentioned in the same table.

In order for the reported results to be consistent with other flow geometries, the dimensions are normalized by their characteristic values. The normalized parameters are then denoted with an asterisk. The velocity is normalized by the maximum velocity at the nozzle exit ($U_0 = 100\ m/s$); i.e. $u^* = u/U_0$. The lengths are normalized by the outer diameter of the annular nozzle; e.g. $r^* = r/D$. Time is also normalized by the characteristic velocity, mentioned above, and the hydraulic diameter which is twice the sheet thickness ($d_h = 2h$), so that $t^* = U_0 t/d_h$.

3.1 Reynolds number effects

In this section the effects of the liquid viscosity, through the Reynolds number, on the flow conditions are investigated. Three different cases with Reynolds numbers of $3,000$, $15,000$ and $30,000$ are analyzed here. The range of the Reynolds numbers that have been chosen for this analysis include a weak turbulent flow (beginning of the turbulent regime), a very intense turbulent flow and a case with moderate turbulence. It should be noted that the Reynolds numbers in this section are varied through the liquid viscosity, while the gas to liquid viscosity ratio are kept constant. The rest of the dimensionless parameters are also held constant at their base values.

In the subsequent sections, the Reynolds number effects on the velocity profile of the flow and its dependent features, like the recirculation zone, are studied first. Next, the effects on the penetration and convergence rate and length of the annular jet are investigated. At the end, the variation of the observed instabilities' wavelengths based on the Reynolds number are reported and the results are compared with the results from linear analysis. It should be noted though, that our 2D axisymmetric analysis does not properly capture transition to turbulence, as turbulence is a three-dimensional phenomenon. A three-dimensional numerical study with very fine mesh and time step is required to see the real turbulent flow and its corresponding 3D instabilities (azimuthal instabilities in this case), which cannot be seen in the current simulation.

3.1.1 Effects on the flow

The axial velocity profile of the liquid jet at the nozzle exit at different instances of time are given in Figure 3.1 for two different Reynolds numbers of $3,000$ and $30,000$. As can be seen from the profiles, the rate of growth of the maximum velocity at the nozzle is almost the same for both cases. Both reach a maximum value of 55 m/s at their centerline just 25 μs after the start of the injection, and this value increased to 80 m/s, 10 μs later. The diffusion of the momentum is, however, higher for the case with higher Reynolds number; which causes a flatter profile at the middle and with steeper gradients at the edges, for the higher Reynolds number case. This results in a higher shear stress at the walls of the nozzle as well as the liquid/gas interface for higher Reynolds. It could be concluded from what is seen in Figure 3.1 that stronger vortices, and hence, more Kelvin-Helmholtz instabilities should be expected at the interface of the liquid with higher Reynolds number, as will be shown later.

The numerical resolution must be sufficient to capture these vortex structures development

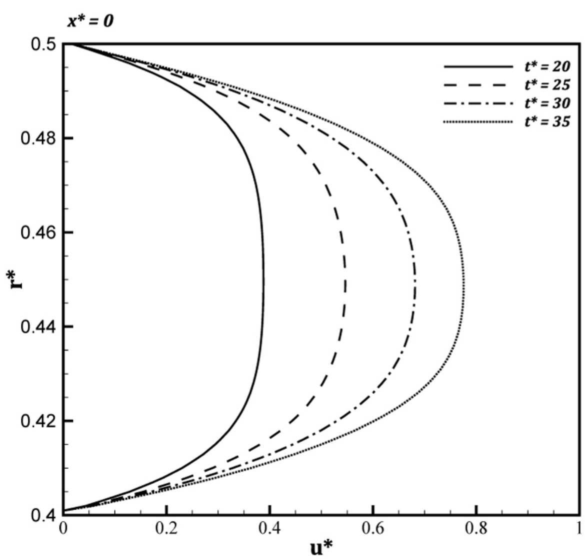

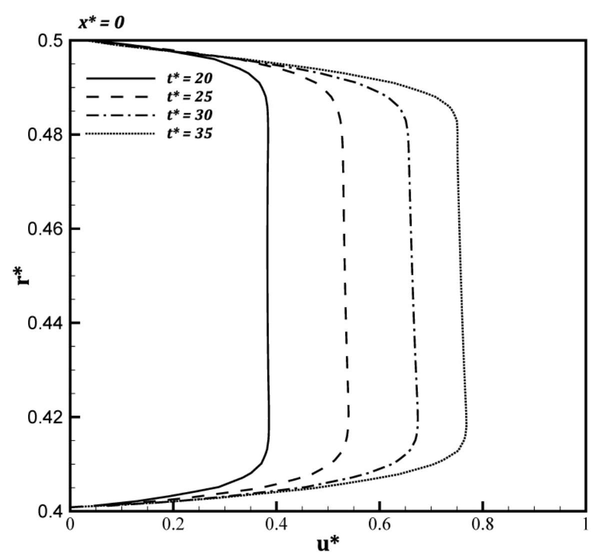

Figure 3.1: Axial velocity profiles at the nozzle exit for different Reynolds numbers at different instances of time. $We = 30,000$, $\hat{\rho} = 0.05$, $\hat{\mu} = 0.0066$, $\hat{d} = 0.8$; $Re = 3,000$ (left), $Re = 30,000$ (right).

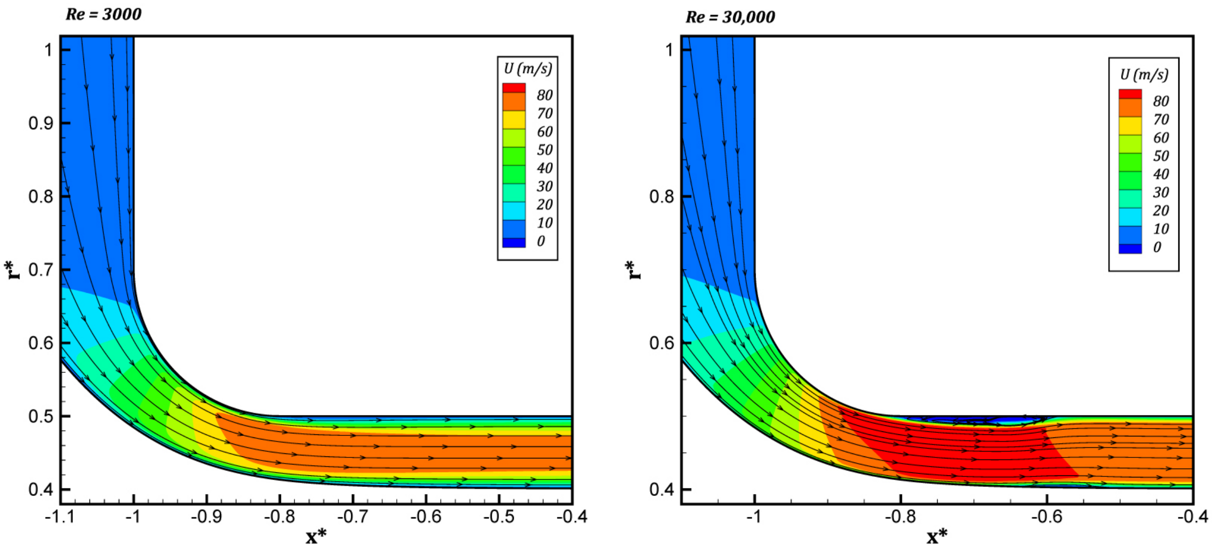

Figure 3.2: Flow streamlines at the upstream nozzle, showing the generation of the recirculation zone at the curved corner. $We = 30,000$, $\hat{\rho} = 0.05$, $\hat{\mu} = 0.0066$, $\hat{d} = 0.8$; $Re = 3,000$ (left), $Re = 30,000$ (right).

since these vortices produce the fingers that break-up and form the spray. For a finger that, in three dimensions, has a location of minimum cross-sectional area in the liquid, the capillary action can cause this neck to shrink and cause breaking. The presence of capillary stress in the model will allow this to happen.

As the Re number increases, the flow separates from the nozzle at the upstream curved corner and generates a recirculation zone at that region since the fluid cannot make a sharp turn at that corner. This fact is shown and compared for the two Reynolds numbers cases, in Figure 3.2. As is illustrated in this figure, the separation does not occur for the case with $Re = 3,000$, but it occurs at higher Re numbers and grows larger with increasing the Re number. Figure 3.3 shows the axial velocity profile at the recirculation zone ($x^* = -0.7$) at $t^* = 35$ for the three cases. As can be seen from this figure, the separation happens at $Re = 15,000$, too; however, its intensity is lower than $Re = 30,000$ case.

The recirculation zone may extend throughout the orifice channel. This phenomenon known as hydraulic flip entrains air into the orifice and fills the recirculating zone. One way to avoid hydraulic flip is to increase the length of the nozzle channel or to reduce the curvature

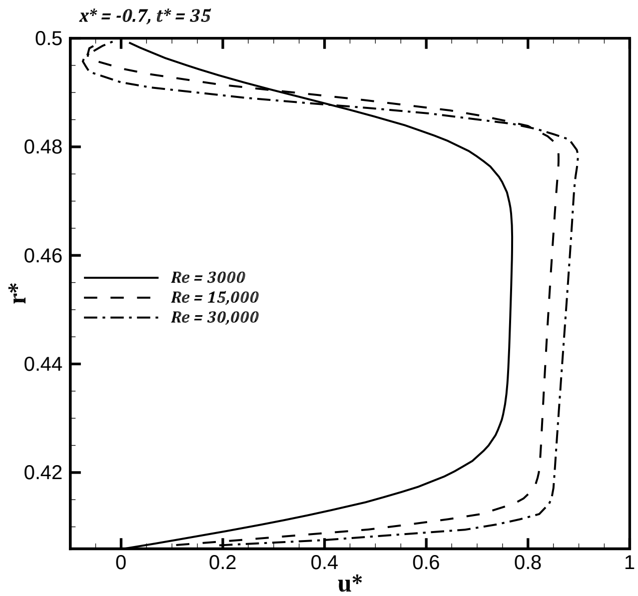

Figure 3.3: The axial velocity profile for different Re, at the recirculation region at the nozzle corner $x^* = -0.7$ at $t = 35\ \mu s$. $We = 30,000$, $\hat{\rho} = 0.05$, $\hat{\mu} = 0.0066$, $\hat{d} = 0.8$.

of the corner. The nozzle length for this research has been chosen to be equal to the nozzle diameter to make sure that such phenomenon does not happen for the cases that we are considering. The effects of cavitation and flow recirculation on jet instability have been explained by Dabiri [65].

Figure 3.4 shows the radial variation of axial velocity with time at different distances downstream of the nozzle exit for $Re = 3000$ and $30,000$. The velocity profiles of the both cases are almost similar up to $t^* = 25$ at all the distances downstream of the nozzle exit (compare the solid and the dashed lines for all the plots). During the start-up the axial velocity in liquid phase increases at the centerline of the liquid sheet while the pressure is building up at the exit of the nozzle. The maximum value of the velocity happens almost at the centerline of the liquid sheet (at $r^* \simeq 0.45$ for $Re = 3000$ and $r^* \simeq 0.4$ for $Re = 30,000$) between $t^* = 30$ and 35, at a distance half a diameter downstream of the nozzle exit (top two plots in Figure 3.4). Farther from the centerline, the velocity decreases. The maximum velocity at the centerline of the sheet is almost 70 m/s at $t^* = 35$ and $x^* = 0.5$. Notice that in the

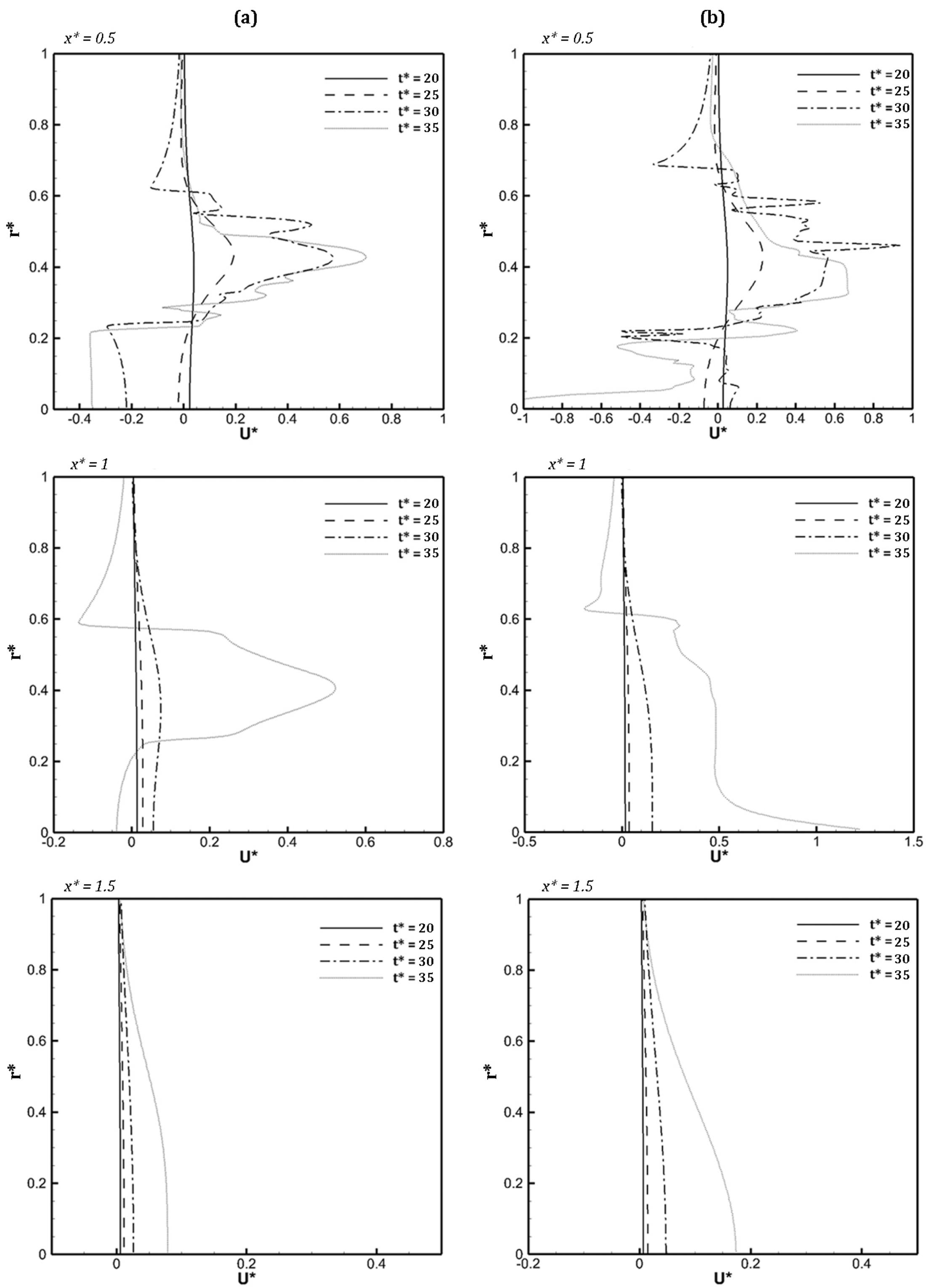

Figure 3.4: The axial velocity profile variation over time at different distances downstream of the nozzle exit. $We = 30,000$, $\hat{\rho} = 0.05$, $\hat{\mu} = 0.0066$, $\hat{d} = 0.8$. (a) $Re = 3,000$; (b) $Re = 30,000$.

meantime, the maximum velocity at the nozzle exit, as was given in Figure 3.1, was 80 m/s; which shows that the sheet centerline velocity is decreasing as it moves downstream.

On the other hand, at the liquid/gas interfaces ($r^* \simeq 0.5$ and 0.4 for $Re = 3000$, and $r^* \simeq 0.45$ and 0.35 for $Re = 30,000$) the gas flow appears to experience vortical motion very close to the interface. The deviations seen on the graph at $t^* = 30$ and 35 close to the interface (sharp kinks) explains the effects of these vortical structures. The nonlinear waves resulting from hydrodynamic instability form vortex structures that affect the shear layer near the interface.

As can be seen from the top plots of Figure 3.4, at $x^* = 0.5$ and $t^* = 35$, the axial velocity is negative and the fluid is moving upstream at the axis of symmetry ($r^* = 0$); which indicates the existence a recirculation zone at that position. The intensity of this recirculation zone is larger for the higher Re case, as can be seen from its greater negative velocity.

At a further downstream distance $x^* = 1$ (center plots in Figure 3.4), the flow remains similar for a longer period of time (up to $t^* = 30$) before the liquid jet reaches that position. At $t^* = 35$, however, the profiles completely differ. For the lower Re case (the left tab) the liquid sheet has not reached the axis of symmetry, and has the maximum velocity at the center of the sheet and decreasing radially outward. The entrainment of the gas flow on both sides of the interface can also be seen in this figure; positive velocities near the liquid interface ($r^* \simeq 0.45$ and 0.35) and negative values at radial positions farther from the interface. In the higher Re case (the right tab) at $t^* = 35$ and $x^* = 1$, however, liquid sheet only entrains the gas at its outer interface, and the velocity increases monotonically towards the axis of symmetry. At this instant the liquid sheet has hit the axis of symmetry at a position upstream of this point, and thus the fluids downstream are pushed by the liquid on the axis. At $x^* = 1.5$ the velocity profiles are the same since the liquid jet has net passed this location so far, in neither of the cases. The velocity magnitudes are slightly greater for the higher Reynolds case, which is due to the liquid jet pushing the gas downstream, as was discussed earlier.

Figure 3.5 illustrates the velocity profile at the axis of symmetry for different instances of time, for all Reynolds cases. As it can be seen, at $t^* = 25$ all of the cases demonstrate a similar behavior; with a recirculation zone at about $x^* = 0.6$ (the solid line). As time elapses, the length of the recirculation bubble increases and it becomes stronger (the dashed line). At later times (the dash-dot and the dotted lines), the profiles show more complexity

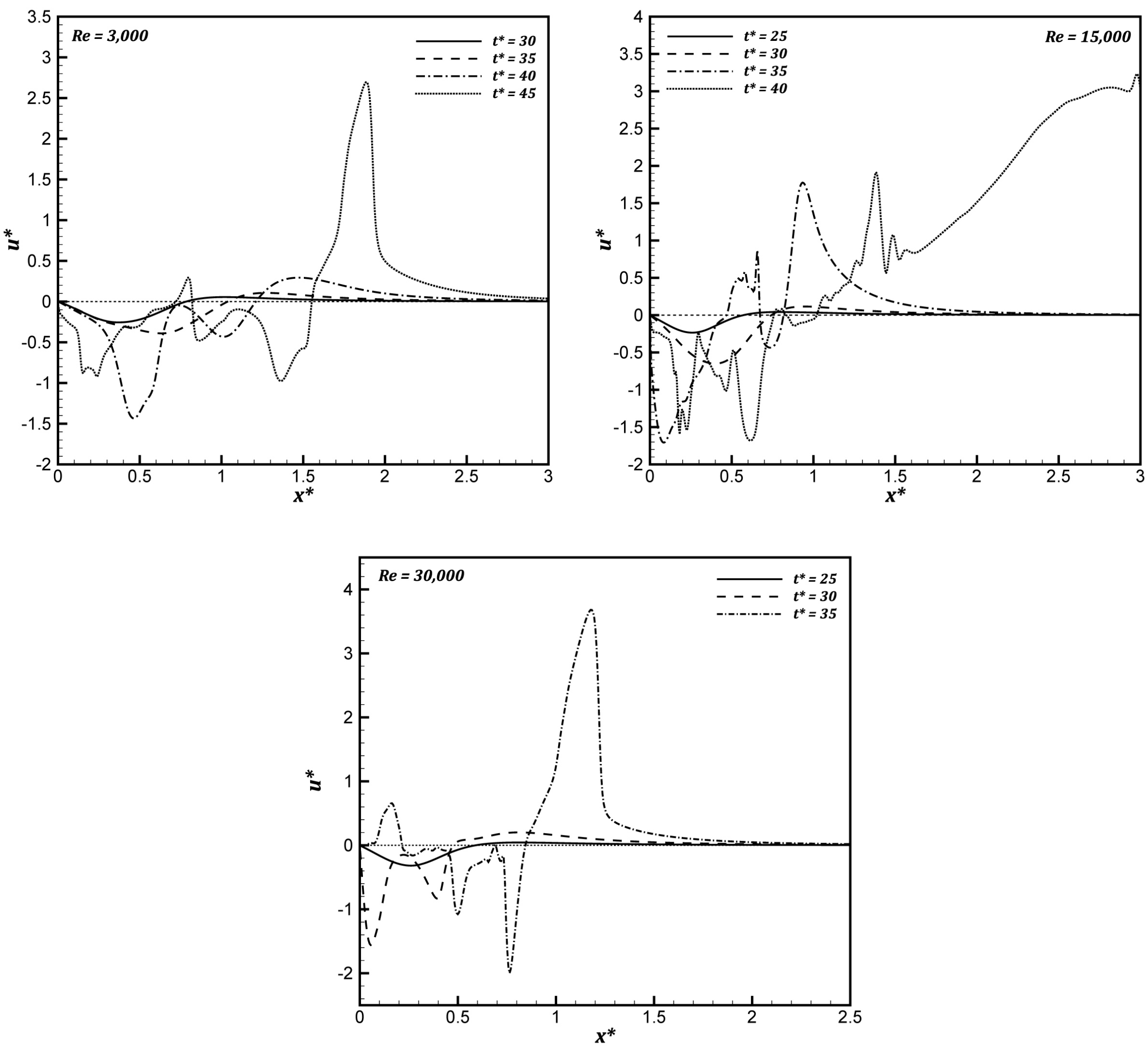

Figure 3.5: The velocity profile on the axis of symmetry at different instances of time for different Re numbers. $We = 30,000$, $\hat{\rho} = 0.05$, $\hat{\mu} = 0.0066$, $\hat{d} = 0.8$.

(oscillations on the negative side), which is due to the occurrence of more recirculating regions and smaller eddies in the region near the axis of symmetry. As can be seen from the figure, the smaller eddies appear sooner for the higher Reynolds case. This behavior is observed at $t^* = 35$, 40 and 45 for $Re = 30,000$, $15,000$ and $3,000$, respectively.

Later in time, the velocity profiles shows two significant velocity reversals along the Centerline. The first one occurs very close to the nozzle exit and is due to the recirculation zone, which its length increases with decreasing the Reynolds number ($x^* = 0.2$ for $Re = 30,000$, $x^* = 0.5$ for $Re = 15,000$ and $x^* = 0.7$ for $Re = 3,000$). The second velocity reversal which occurs further downstream, corresponds exactly to the locations where the collapse of the annular jet takes place ($x^* \approx 0.8$–1.5), and could be a good indication of the convergence length of the annular jet. The large peak after the second velocity reversal in all the cases is associated with the liquid jet pushing forward the downstream gas after its collapse on the axis of symmetry. Further downstream, the velocity decreases smoothly, until it reaches zero velocity indicating quiescent far-field gas. The existence of two significant velocity reversals were also reported by Siamas et al. [60].

The unpredictable behavior of the velocity profile along the centerline and near the nozzle exit, clearly shows the importance of the knowledge of vortex dynamics in the study of annular jet instabilities like this. The formation of the vortical structures is mainly associated with the development of the KH instabilities, which occurs when velocity shear is present within a continuous fluid or when there is sufficient velocity difference across the interface between the two fluids. Figure 3.6 shows the liquid/gas interface (the zero level-set) at $t^* = 35$ for $Re = 30,000$. The blue color in this figure represents the liquid, and the white region is the gas. A schematic of the eddies and streams are also demonstrated by arrows in this figure. The size of the arrows and their direction, represent the size and direction of the real eddies.

As can be seen in Figure 3.6, the recirculation zone on the inner side of the annular jet,

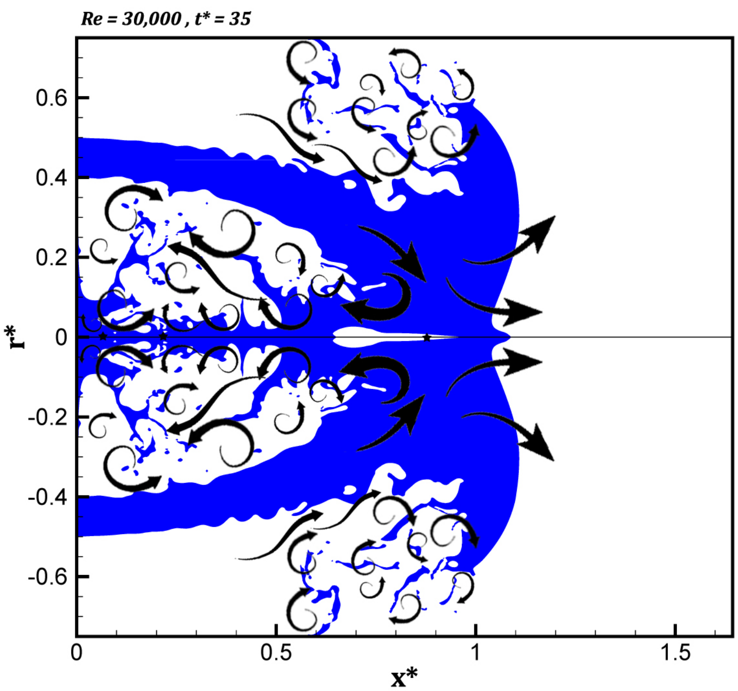

Figure 3.6: Liquid/gas interface at $t^* = 35$, and a schematic of the eddy structures. $Re = 30,000$, $We = 30,000$, $\hat{\rho} = 0.05$, $\hat{\mu} = 0.0066$, $\hat{d} = 0.8$.

actually consists of numerous large and small eddies with different directions and intensities. This figure can give a better insight into the understanding of the velocity profile along the centerline for $Re = 30,000$ at $t^* = 35$, which was given in Figure 3.5 (the dash-dotted line on the bottom plot). The three stagnation points on the centerline, corresponding to the velocity reversal points on the plot, are indicated by the star symbols in Figure 3.6. The large arrow to the right of the last stagnation point, corresponds to the largest peak on the figure, and the arrows pointing towards its left indicate the negative velocity (trough) of the profile on the left of the last reversal point. Figure 3.6 clearly shows the entrainment of the gas by the liquid jet on the inner and outer surface of the annulus. The appearance of the KH instabilities on the main stem of the liquid jet, as a result of the large velocity difference across the interface and its consequent vortices, are also shown on this figure.

The thickness of the smallest ligaments and the diameter of the corresponding pinched-off drops in Figure 3.6 is in order of 4–6 μm, which comparing to our mesh size 1.5 $\mu m \times$ 1.5 μm, shows that there are enough mesh points in each of the liquid elements to describe their interface curvatures sufficiently enough. The effects of the mesh size on the ligaments thickness was discussed previously, and will be discussed later on, when the study of the wavelength of the instabilities are presented.

3.1.2 Penetration/convergence rate

Ibrahim & McKinney [21] described that, without a strong enough swirl for the inertia forces to overcome the opposing surface tension, the annular jet converges towards the centerline. The annular jet exhibits formation of a “bell shape” near the nozzle exit plane. This shape occurs because, upon emerging from the nozzle exit, the jet has the tendency to converge continuously towards the centerline. The annular jet collapses into a “solid” round jet further downstream of the computational domain and it spreads in the cross-streamwise direction when the collapse is taking place. The collapse also increases the tendency of liquid breakup. The formation of the “bell-shaped” annular sheet can be seen in Figure 3.6.

The length and rate of the annular sheet collapse is an important characteristic of the annular jet injection. A shorter and faster convergence towards the centerline corresponds to faster atomization and shorter jet breakup length. In this section, the effects of the flow Reynolds number on the convergence rate and length of the annular sheet are discussed. Another pertinent parameter in this regard is the penetration rate of the liquid jet, which is also compared for different Re cases.

Predictions of the dimensionless radius of the annular sheet with the axial distance from the nozzle exit for different Re cases is presented in Figure 3.7. The lines show the trajectories of the mid-point of the liquid sheet core, that have been traced from the injection plane to the location where the jet collapse takes place.

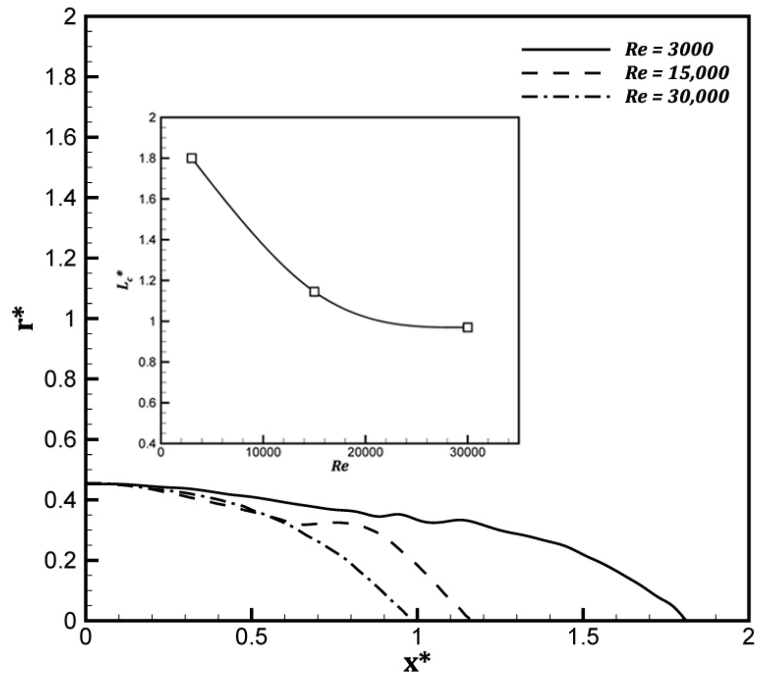

Figure 3.7: Axial variation of the dimensionless radius for different Re numbers (the main plot); comparison between the convergence lengths of different Re cases (the inner plot). $We = 30,000$, $\hat{\rho} = 0.05$, $\hat{\mu} = 0.0066$, $\hat{d} = 0.8$.

From Figure 3.7 it is evident that, as the Reynolds number is decreased, the convergence length of the annular sheet increases, producing a more elongated bell with larger radius but smaller curvature. The convergence length (L_c) for $Re = 3000$ is 1.8 times the nozzle diameter, while it is almost equal to the nozzle diameter for $Re = 30,000$. A shorter "bell shape" at higher Reynolds corresponds to a larger downstream spreading, which is expected as they both correspond to a stronger mixing of the annular jet with its ambient environment.

The inner plot in Figure 3.7 shows the normalized convergence length (L_c^*) versus the Reynolds number. As indicated, the convergence length decreases with increasing the Reynolds number; however, it becomes almost independent of the Re number, at very high Reynolds. This means that it is not possible to decrease the convergence length continuously to any desired value by just increasing the Re number. The results indicate that the minimum convergence length that could be reached with this geometry is almost equal to the nozzle diameter; i.e. $L_c^* = 1$.

The comparison between the convergence rate of the annular sheets for different Reynolds numbers is given in Figure 3.8. Each symbol in this figure, indicates the radial distance of the tip of the liquid jet from the axis of symmetry at its corresponding dimensionless time. The results indicate a behavior similar to the convergence length; i.e. the higher Reynolds case converges faster than the lower Re cases. The jet with $Re = 3000$ collapses on the centerline at $t^* = 46$ while the case with $Re = 30,000$ converges after $t^* = 35$, and the convergence rate becomes less dependent on the Reynolds number, as the Re number increases. In other words, the convergence rate decreases more rapidly with Re at lower Reynolds numbers.

The axial penetration of the annular liquid jet over time is compared in Figure 3.9 for different Reynolds numbers. As the figure shows, all of the Reynolds cases have a similar axial penetration rate before their collapse on the centerline; which means, they have all

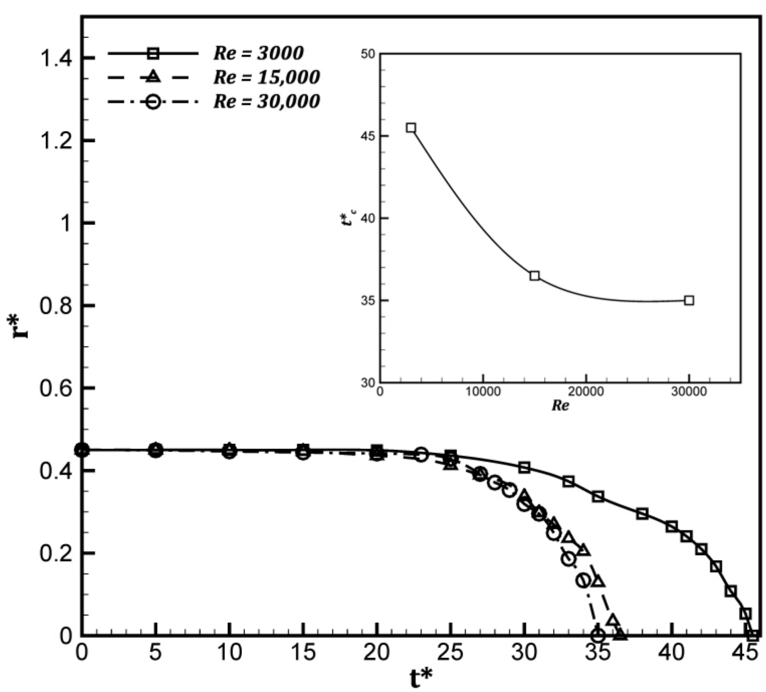

Figure 3.8: Variation of the dimensionless radius of the annular jet tip versus dimensionless time, for different Re numbers (the main plot); comparison between the convergence rate of different Re cases (the inner plot). $We = 30,000$, $\hat{\rho} = 0.05$, $\hat{\mu} = 0.0066$, $\hat{d} = 0.8$.

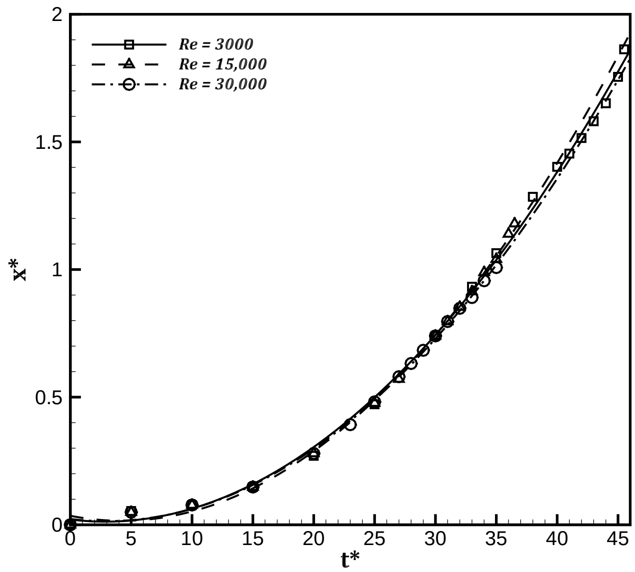

Figure 3.9: Axial penetration of the annular jet versus dimensionless time, for different Re numbers. $We = 30,000$, $\hat{\rho} = 0.05$, $\hat{\mu} = 0.0066$, $\hat{d} = 0.8$.

reached the same axial distance from the nozzle exit, at the same time. For instance, the time required for all of the cases to penetrate one diameter in the axial direction is $t^* = 35$. However, these results should not be misinterpreted, as this does not mean that the length of the liquid sheets are the same for all cases. As was indicated in Figures 3.7 and 3.8, the case with higher Re converges faster, and thus, at the same time instant, the tip of its jet is closer to the axis of symmetry than the lower Re jets. This means that, the length of the annular sheet in larger for the higher Re cases; however, the length difference between the high Re case and the lower Re case is contributed to the radial growth (convergence), keeping the axial penetrations the same for all cases. The reason is that, the higher Reynolds number jet has more momentum relative to various drag effects; so, it penetrates farther (both radially and axially) and produces a longer jet at comparable instants of time. For the lower Reynolds number case this lack of momentum leads to a shorter liquid jet at different stages of injection.

3.1.3 Instability analysis

Figure 3.10 compares the evolution of the annular jets at different instances of time for $Re = 3000$ and $Re = 30,000$ cases. This figure illustrates the formation of a mushroom-shaped cap (2D) as the jet develops along the chamber while the pressure drops and the jet exit velocity increases during the first 25 μs from the start of injection. The mushroom-shaped cap grows in volume and vortices at the interface roll back and entrain air into the rear side of the cap as was seen before. This figure also illustrates the effects of liquid viscosity on the jet development for the same exit velocity at the nozzle exit at comparable instants of time. The viscosity of the liquid in (a) is 10 times that of (b). The discrepancies between the unstable structures at the liquid/gas interface on the cap shown in Figure 3.10 (a) and (b) are significant.

Figure 3.10 shows that the mushroom-shaped cap deforms after 30 μs from the start of injection and well-known KH and RT inabilities appear on the liquid/gas interface. Unlike the primary KH wavelengths, RT waves are directing normal to the direction of the flow and have smaller wavelengths compared to the primary KH wavelengths. For lower Re numbers, shown in 3.10(a), the RT wavelengths are significantly larger compared to case (b). This is consistent with the fact that viscosity has stabilizing effects for shorter wavelengths if surface tension is constant.

By comparing the two columns in Figure 3.10, it can be seen that the instabilities occur much sooner, and grow much faster, for the higher Re jet. The RT instabilities emerge at $t^* = 25$ for $Re = 30,000$, while only a few instabilities appear at the back of jet cap at $t^* = 30$ for lower Reynolds case. High Re number jet is associated with longer and thinner ligaments with RT wavelengths appearing at the rear side of the cap. In other words, the front of the jet decelerates due to the drag forces acting on it. So, the lighter fluid is then accelerating into the heavier fluid, which according to the RT theory would be stabilizing

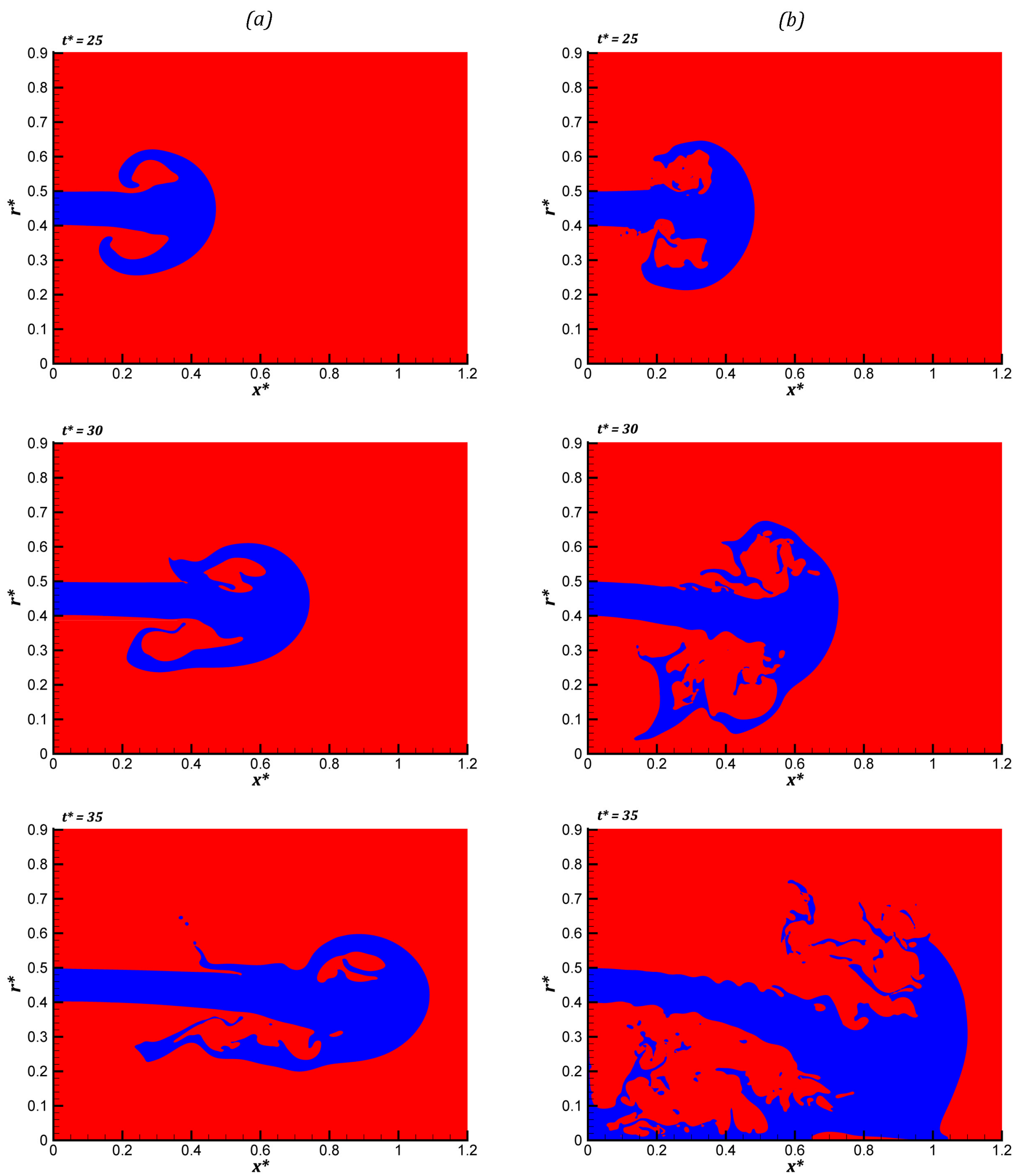

Figure 3.10: Jet development at $t^* = 25$ (top), $t^* = 30$ (middle) and $t^* = 35$ (bottom). $We = 30,000$, $\hat{\rho} = 0.05$, $\hat{\mu} = 0.0066$, $\hat{d} = 0.8$; (a) $Re = 3000$, (b) $Re = 30,000$.

on the front side of the jet cap and destabilizing on the rear side of the jet cap. However, due to the stabilizing effects of viscosity, we did not detect RT waves at the back of the cap for case (a) at $t^* = 30$. As time elapses, longer RT wavelengths compared to case (b) seat at the back of the jet cap. Effects of viscosity on the wavelength and growth rate of the instabilities on the annular jet interface are analyzed in this section.

Guidance from the linear theory

Although the research to be discussed uses the complete Navier-Stokes equations to solve the annular jet injection and accounts for the nonlinear behavior and couplings between different instability mechanisms, it is useful to examine the predictions of the linear theory especially in terms of unstable wavelengths and the dominant wavelengths with the maximum growth rates.

There are four physical phenomena which contribute to the hydrodynamic instability: (1) acceleration tangent to the interface, i.e., Rayleigh-Taylor (RT) instability; (2) inertial difference across the shear layer at the jet interface, i.e., Kelvin-Helmholtz instability; (3) capillary effects; and (4) viscous effects. These four effects are ordered above so that, in the dispersion relation for the growth rate obtained for viscous potential flow (and not therefore for shear flow) discussed by Joseph et al. [4], the four related terms appear proportional to wave number to the first, second, third, and fourth power, respectively. So, viscous effects dominate at very short wavelengths while gravity (acceleration) effects dominate at very long wavelengths and surface tension has stabilizing effects on shorter wavelengths. If an acceleration much larger than gravitational acceleration is applied, which is the situation in our transient jet, short wavelength can be experienced. The acceleration term is destabilizing (stabilizing) when the heavier (lighter) fluid accelerates into the lighter (heavier) fluid [5].

Joseph et al. [4] studied the stability of stratified gas-liquid flow in a horizontal rectangular channel using viscous potential flow. The analysis led to an explicit dispersion relation in which the effects of surface tension and viscosity on the normal stress are not neglected but the effect of shear stresses is neglected. In their analysis, a gas layer of thickness h_g with uniform velocity (U_g) is considered over a liquid layer of half thickness h_l with uniform flow (U_l); the two-layer Newtonian incompressible fluids are immiscible. The pressure has been considered to have an equilibrium distribution due to the gravity. The Kelvin-Helmholtz instability is considered of small disturbances to the undisturbed state. The discontinuous prescription of data in the study of Kelvin-Helmholtz instability is a viscous potential flow solution of the Navier-Stokes, in which no-slip conditions at the walls and no-slip and continuity of shear stress across the gas liquid interface are neglected. The following general dispersion equation can be obtained from Joseph et al. [4].

$$\omega_r = \frac{1}{A}\left\{-B \pm (D_r^2 + D_i^2)^{1/4} \cos\left(\frac{1}{2}\tan^{-1}(\frac{D_i}{D_r})\right)\right\} \tag{3.1}$$

where

$$\begin{aligned}
A &= \rho_l \coth(kh_l) + \rho_g \coth(kh_g) \\
B &= k^2[\mu_l \coth(kh_l) + \mu_g \coth(kh_g)] \\
D_r &= \rho_l \rho_g (U_g - U_l)^2 k^2 \coth(kh_l)\coth(kh_g) + k^4[\mu_l \coth(kh_l) + \mu_g \coth(kh_g)] \\
&- [\rho_l \coth(kh_l) + \rho_g \coth(kh_g)][(\rho_l - \rho_g)gk + \sigma k^3] \\
D_i &= 2k^3(\rho_g \mu_l - \rho_l \mu_g)(U_g - U_l)\coth(kh_l)\coth(kh_g)
\end{aligned}$$

In the equation above, ω_r is the temporal growth rate, μ_l, μ_g, ρ_l, and ρ_g are the viscosity and density and the indices l and g refer to liquid and gas, respectively. σ is the surface tension coefficient, k is the wave number, g is the gravitational acceleration that can be replaced by the acceleration of the light fluid into the heavy liquid since this acceleration is considerably greater than gravitational acceleration, as discussed in the previous section. If ω_r (the real part of the complex frequency) is negative, then the interface is stable. In our case, the gas velocity U_g is zero and the thickness of the gas layer h_g is much greater than the liquid sheet thickness, thus $h_g \to \infty$, and $\coth(kh_g) = 1$.

Joseph et al. [4] show that, if both the top and bottom are far away $h_g \to \infty$, $h_l \to \infty$, and if $\hat{\rho} = \hat{\mu}$, so that D_i becomes zero ($\rho_g \mu_l = \rho_l \mu_g$), the dispersion relation reduces to the simplest compact form given below:

$$\omega_r = \frac{-k^2(\mu_g+\mu_l)}{(\rho_g+\rho_l)} \pm \left[\frac{k^4(\mu_g+\mu_l)^2}{(\rho_g+\rho_l)^2} - \frac{\sigma k^3}{(\rho_g+\rho_l)} + \frac{\rho_g\rho_l k^2(U_g-U_l)^2}{(\rho_g+\rho_l)^2} - \frac{(\rho_l-\rho_g)gk}{(\rho_g+\rho_l)}\right]^{1/2} \tag{3.2}$$

Figure 3.11 shows a plot of the growth rate versus wavelength based on Equation (3.1) by Joseph et al. [4] for three Reynolds numbers that are considered in this study. The same dimensionless parameters mentioned in Table 2.1 have been used in this plot. Positive values indicate the instability region while negative values ($\lambda < 0.4\ \mu m$) imply stability. Clearly, at sub-micron wavelengths, where viscosity and capillary effects dominate, we find stable behavior.

The dispersion relation reflected in (3.1) accounts for both Kelvin-Helmholtz and Rayleigh-Taylor instabilities. Figure 3.11 clearly shows that instabilities are expected in the wavelength range that are found in our simulations, i.e. $O(1\text{–}100\mu m)$. As shown for our sub-millimeter, super-micron wavelength range of interest, unlike the gravity viscosity and surface

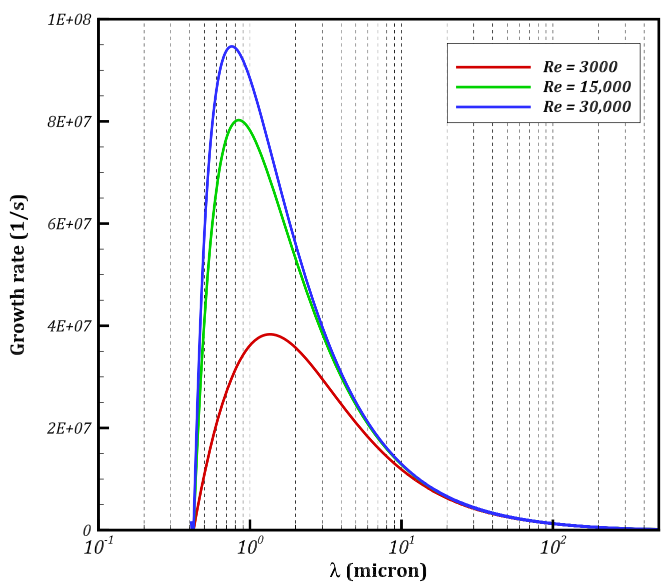

Figure 3.11: Linear growth rate as a function of wavelength based on VPF instability analysis of Joseph et al. [4]. $We = 30,000$, $\hat{\rho} = 0.05$, $\hat{\mu} = 0.0066$, $\hat{d} = 0.8$.

tension are very important. As can be seen in this figure, the maximum instability growth rate moves towards smaller wavelengths, as Re number increases, and we should expect to see smaller wavelengths at higher Reynolds numbers. The range of unstable wavelengths, however, is not affected by the viscosity variation. It should be emphasized that the given plot is based on the linear theory, which does not take into account the effects of shear stress, and is not able to give very accurate information about the dominant wavelength with maximum instability growth rate. However, it gives a proper guidance about the range of the instabilities and their behavior with respect to viscosity variation.

Computational results

The prediction of the small-scale wavelengths is of great importance. According to Varga et al. [37], the scale of the primary mean droplet sizes during the atomization process are close to the most unstable RT wavelength. The most interesting unstable structures, especially the secondary instability occurs after the mushroom-shaped cap develops during the first 40 μs after the start of injection.

The break-up of the ligaments, that emerge as the instabilities grow, produce a range of small-scale drops. Observation of this phenomenon in computational simulations is very much dependent on the grid resolution. As discussed earlier, a coarse grid produces thicker ligaments and larger droplets when detached from the jet core. If we were considering secondary atomization models these larger droplets would turn into smaller droplets later in time. This dependence on the numerical grid resolution has been reported by Gorokhovski & Hermann [55].

In order for the reported wavelengths and two-dimensional drop diameters to be accurate, the grid resolution should be sufficiently high. In other words, the size of the grid cells should be smaller than the smallest drops that we are supposed to observe in the annular

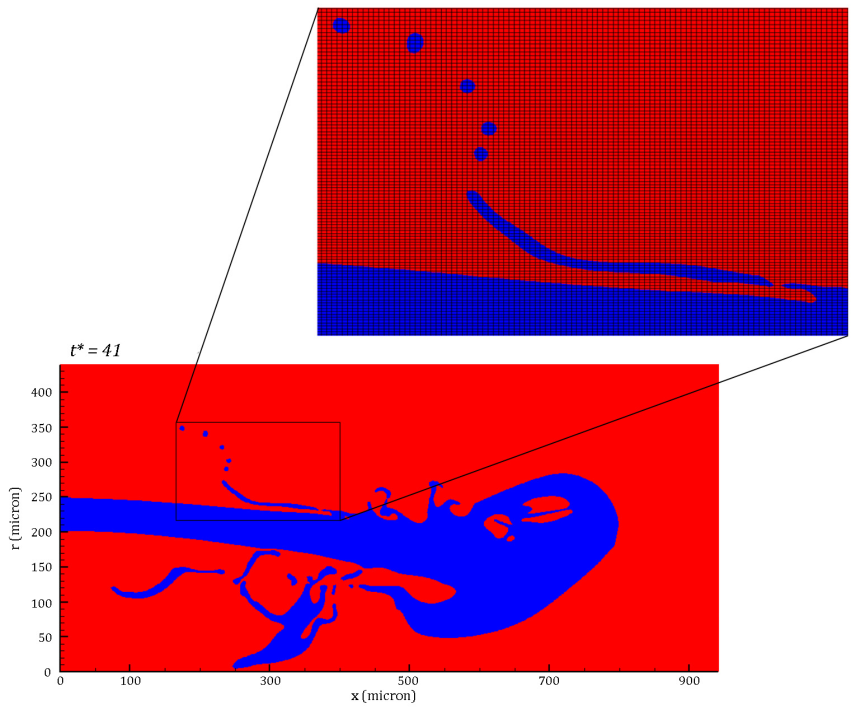

Figure 3.12: The grid resolution check in capturing the smallest drops. $Re = 3000$, $We = 30,000$, $\hat{\rho} = 0.05$, $\hat{\mu} = 0.0066$, $\hat{d} = 0.8$.

jet flow. Figure 3.12 illustrates the grid resolution around some droplets (3D rings) that are ruptured from a ligament that protrudes from the main jet core, for a typical $Re = 3000$ case, at $t^* = 41$. As the figure shows, there are at least 12–15 grid cells inside the smallest droplets, which enables the computational code to predict the droplets interface position and its surface curvature with sufficient precision. The grid system that has been used for this computational simulation is able to capture the droplets with diameters larger than about 4 μm; which is sufficient for capturing the drop sizes that are observed in the experiments for this kind of flow.

Figure 3.13 graphs the unstable structures at the jet interface at different instances of time after the injection (35–40 μs) for $Re = 3000$ (Fig. 3.13(a)) and $Re = 30,000$ (Fig. 3.13(b,c)). These three figures show the instabilities on the main liquid sheet core and regions close to the jet tip; i.e. on the back of the mushroom-shaped cap. This figure indicates how different types of instabilities at the jet interface have been differentiated in this study. The vertical

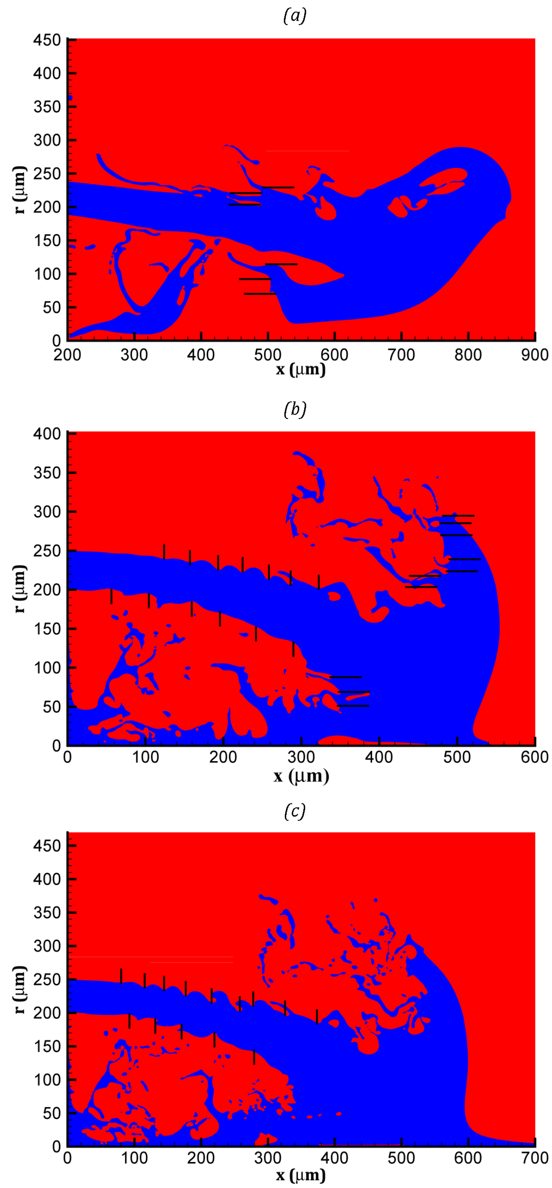

Figure 3.13: Unstable structures at the liquid interface at different time instants, indicating primary (KH) and secondary (RT) wavelengths on the main liquid sheet stem and close to the head part of the jet. $We = 30,000$, $\hat{\rho} = 0.05$, $\hat{\mu} = 0.0066$, $\hat{d} = 0.8$; $Re = 3000$ (a), $Re = 30,000$ (b,c). (horizontal and vertical tick marks indicate secondary and primary instability wavelengths, respectively.)

tick marks in this figure show the primary KH wavelengths while the horizontal tick marks indicate the RT secondary wavelengths on top of the primary KH wavelengths and also at the back of the jet cap.

As Figure 3.13 illustrates, the wavelength of both KH and RT instabilities are larger for

$Re = 3000$ (a) compared to the higher Re case (b,c), indicating the stabilizing effect of the liquid viscosity for shorter wavelengths. The higher Re case corresponds to thinner ligaments and smaller droplets, while the ligaments are thicker and longer for the lower Re case, with the same surface tension (We number). The number of unstable waves and the detached ligaments resulting from them are also more discernible for $Re = 30,000$ compared to the lower Re jet.

The range of unstable KH and shorter RT wavelengths during the early stages of injection has been demonstrated in Figure 3.14 for the three Re numbers. The wavelength in these

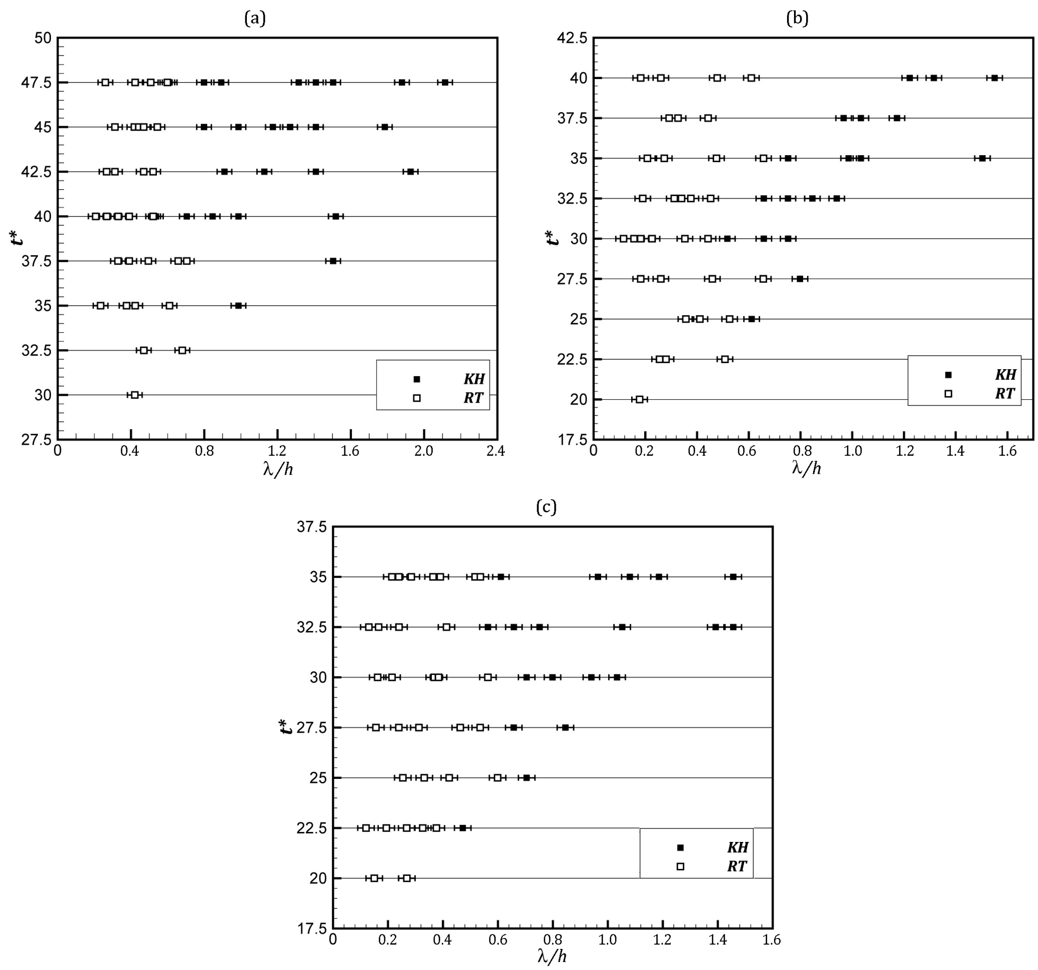

Figure 3.14: Dimensionless KH and RT wavelength spectrum during start-up vs. time; the error bars correspond to 5% and $h = 50\ \mu m$. $We = 30,000$, $\hat{\rho} = 0.05$, $\hat{\mu} = 0.0066$, $\hat{d} = 0.8$; $Re = 3000$ (a), $Re = 15,000$ (b), $Re = 30,000$ (c).

plots, has been normalized by the liquid sheet thickness $h = 50\ \mu m$, so that it could be more conveniently compared to the cases with different sheet thicknesses, as will be analyzed in the future sections.

What could be seen in all of the plots in Figure 3.14 is that, in all cases, the RT instabilities are observed earlier than the first seen KH instabilities. It is also clear that instabilities occur much sooner for high Re jets compared to the lower ones. At $t^* = 30$ for $Re = 3000$ jet and $t^* = 20$ for the two higher Re cases, secondary instability wavelengths in the range of 0.2–0.5 sheet thickness are detected at the back of the jet cap. 5 μs later, KH waves in the range of 0.6–1.0 sheet thickness appear at the interface due to the shear instability at the liquid sheet main stem. Later in time, KH waves continue to develop at the upstream interface further and air is entrained between the interfacial protrusions. As the liquid jet develops with time, drag causes the relative velocity between the liquid and air to decrease, and consequently, the primary KH wavelengths increase to more than $1.5h$ and $2h$ for the highest and lowest Re cases, respectively. This is consistent with the linear KH theory; with negligible gravity, the decrease of the relative velocity between the liquid and gas causes an increase in the most unstable KH wavelength.

The secondary wavelengths associated with the longer KH waves also increase to $0.6h$–$0.8h$ compared to their smaller values (0.2–$0.5h$) at earlier time instants. The acceleration of the surface decreases as the relative velocity decreases, which explains the increase in secondary wavelengths. The drag forces acting on the liquid are also stronger at the beginning of the injection, which corresponds to higher jet acceleration and high shear stress at the liquid/gas interface leading to small wavelength KH and secondary instabilities at the earlier stages. As the jet develops, the acceleration of the liquid jet and the drag forces decrease; thus, longer wavelengths appear at the interface.

Secondary instability with smaller wavelengths compared to KH waves, first appear on the back of the jet cap and later at the interface. In addition, it can be concluded from the plots

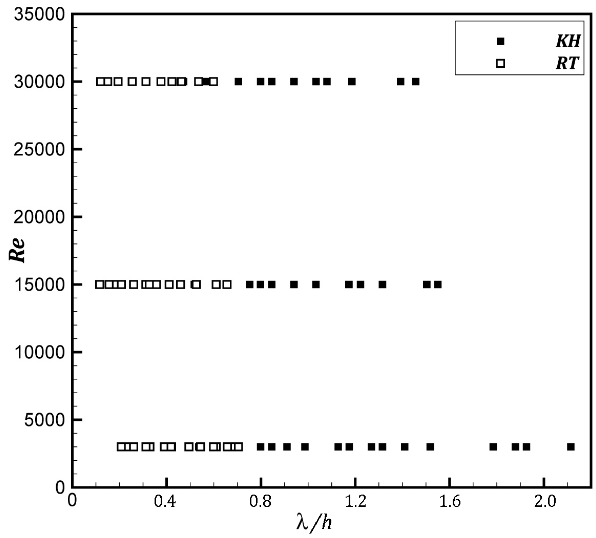

Figure 3.15: Dimensionless KH and RT wavelength spectrum during start-up vs. the Re number. $h = 50\ \mu m$, $We = 30,000$, $\hat{\rho} = 0.05$, $\hat{\mu} = 0.0066$, $\hat{d} = 0.8$.

in Figure 3.14 and Figure 3.13, that the deformation of the jet starts from the head part and is convected upstream toward the orifice. This transmission of the disturbances from the jet tip in the opposite direction of the liquid jet flow has been also indicated by Jarrahbashi and Sirignano [79] and Shinjo and Umemura [57].

Figure 3.15 illustrates the dimensionless KH and RT wavelength spectrum versus the Re number. As is obvious from the figure, both KH and RT wavelengths increase by decreasing the Re number; the reason being that the higher viscosity at lower Re numbers, dampens the smaller instability wavelengths. The range of the RT and KH instabilities, that have been detected during the first 40 μs of the injection, are between 10–35 μm and 30–110 μm, respectively. These results are in accordance with the linear theory results, that were discussed at the beginning of this section, as well as the experimental observations.

The computational results also indicate that for comparable wavelengths, the amplitude of the KH instabilities on the outer liquid interface are larger than the inner surface, which shows that the outer surface is more unstable with higher growth rates. This is consistent with the linear analysis results of Shen & Li [15], who reported that the ratio of the inner to outer wave amplitudes for the same wavelength is always less than one, and approaches one asymptotically, as the annulus radius goes to infinity; i.e. planar sheet. The complete stages of the jet evolution for the three Reynolds cases are given in appendix A.

3.2 Weber number effects

The effects of surface tension on the growth of the instabilities on the liquid/gas interface and size of the corresponding liquid elements and pinched-off droplets are analyzed in this section. The surface tension in this study is varied through the Weber number, keeping the rest of the dimensionless parameters, as well as the Re number, constant. The variation in the penetration and convergence rate and distance due to the surface tension are also discussed here. The We numbers that are considered in this study are 6000, 30,000 and 150,000, which correspond to an interface with very high surface tension, a moderate surface tension (Kerosene and air), and a very low surface tension, respectively.

3.2.1 Effects on penetration/convergence rate

Figure 3.16 shows the axial variation of the dimensionless radius of the liquid sheet mid-line, for different We numbers. In the sub-plot of the same figure, the variation of the dimensionless convergence length L_c^* versus the We number is given. As can be seen from these figures, the convergence length of the annular sheet decreases slightly, by increasing the We number. The variation in the convergence length is less than $0.1D$ (from $L_c^* \approx 1.25$ to $L_c^* \approx 1.15$) from the lowest to highest Weber number cases. This shows the less significant effect of the We number, compared to the Re number (Fig. 3.7), on the liquid sheet convergence length. However, the wiggles in the main liquid stream increases drastically, as the We number increases. This could mean that the instabilities incline more towards

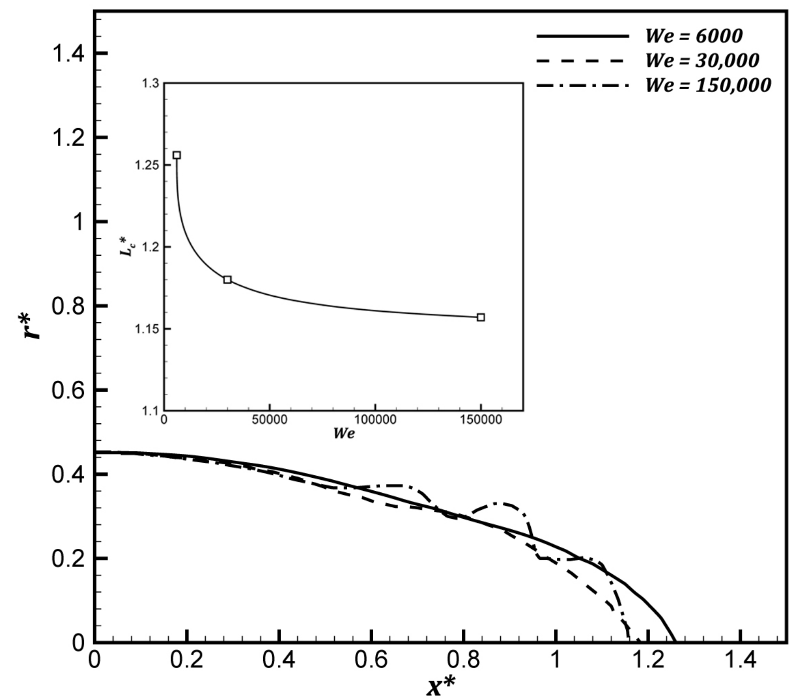

Figure 3.16: Axial variation of the dimensionless radius for different We numbers (the main plot); comparison between the convergence lengths of different We cases (the sub-figure). $Re = 15,000$, $\hat{\rho} = 0.05$, $\hat{\mu} = 0.0066$, $\hat{d} = 0.8$.

the para-sinuous mode as the We number increases. However, in such transient numerical simulation, one cannot claim such conclusion for sure, because the main liquid sheet is also under the influence of the ligaments and drops that collapse on the main stem after their breakup. As the We number increases (the surface tension decreases), the number of such incidents increase, as the number of broken-off droplets increases. The impact of these pinched-off drops and liquid elements on the liquid sheet causes deviation in the liquid sheet trajectory from its pre-owned path; i.e. the observed wiggles.

The effects of the surface tension on the convergence rate of the liquid sheet annulus is illustrated in Figure 3.17. The main plot shows the variation of the dimensionless radius of a point on the annular jet tip over dimensionless time. Similar to the convergence length, the convergence rate is also not affected by the We number, significantly. The sub-plot of Fig. 3.17 shows that all of the cases converge after 36.5–37.5 μs from the start of injection;

the dimensionless convergence time t_c^* decreasing with We number, slightly.

The axial penetration of the annular liquid jet over time is demonstrated in Figure 3.18, for different We numbers. Like the Re number, the We number does not change the liquid jet's axial penetration rate. As can be seen in the figure, all of the cases follow the same behavior through time. This figure along with Fig. 3.17 indicate that the effects of the Weber number on the jet penetration (both axial and radial) are negligible. All of the We cases produce the same length of jet at comparable time instants.

3.2.2 Effects on the instabilities

Figure 3.19 shows the instabilities growth rate as a function of wavelength for different We numbers, based on the linear Viscous Potential Flow theory of Joseph et al. [4]. As

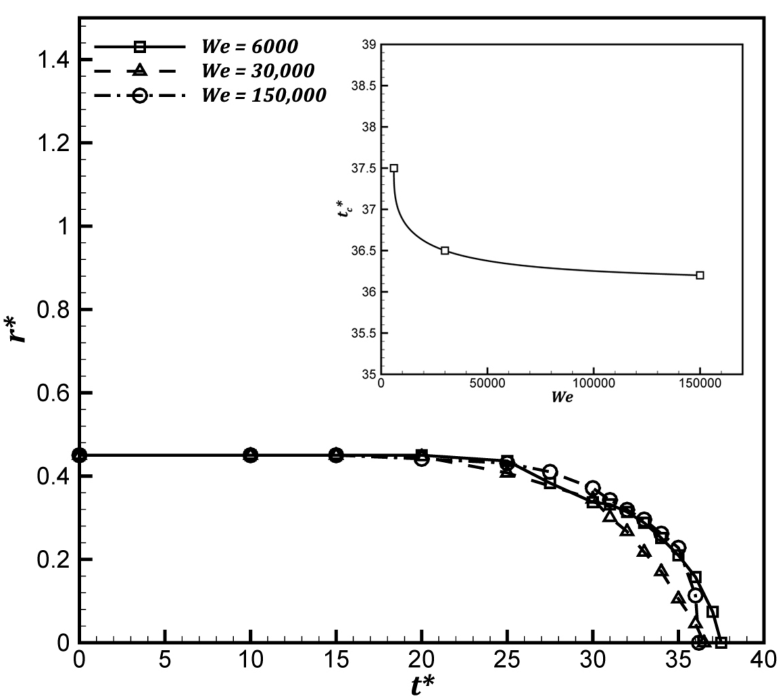

Figure 3.17: Variation of the dimensionless radius of the annular jet tip versus dimensionless time, for different We numbers (the main plot); comparison between the convergence rate of different Re cases (the sub-plot). $Re = 15,000$, $\hat{\rho} = 0.05$, $\hat{\mu} = 0.0066$, $\hat{d} = 0.8$.

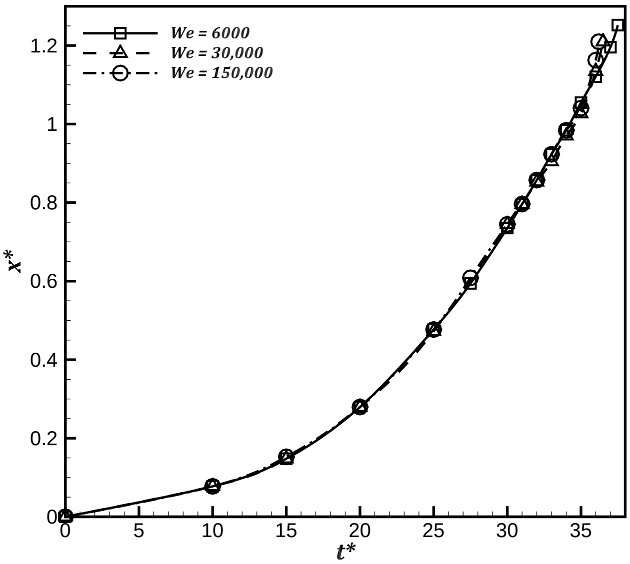

Figure 3.18: Axial penetration of the annular jet versus dimensionless time, for different We numbers. $Re = 15,000$, $\hat{\rho} = 0.05$, $\hat{\mu} = 0.0066$, $\hat{d} = 0.8$.

can be seen from this figure, unlike the Re number (viscosity), the We number (surface tension) changes the range of unstable wavelengths. As the surface tension decreases, both the neutral wavelength (the smallest unstable wavelength) and the dominant wavelength (the wavelength with the maximum growth rate) decrease. Based on the linear theory, the waves with wavelength greater than 0.1 μm, 0.4 μm and 2 μm are unstable for $We = 150,000$, $30,000$ and 6000, respectively.

Figure 3.19 also indicates that the maximum growth rate also increases with the We number. Based on the viscous potential flow analysis, the surface tension has stabilizing effects for high jet velocity and high Re numbers [4]. Qualitatively, by decreasing the surface tension, we should expect for thinner ligaments to form and small wavelengths to appear at the rear side of the jet cap and strong KH and RT waves to appear on the liquid/gas interface, which will eventually breakup into more small liquid rings, as is shown in Figure 3.20.

Figure 3.20 shows the effect of surface tension on the shape of liquid jet surface (zero level-

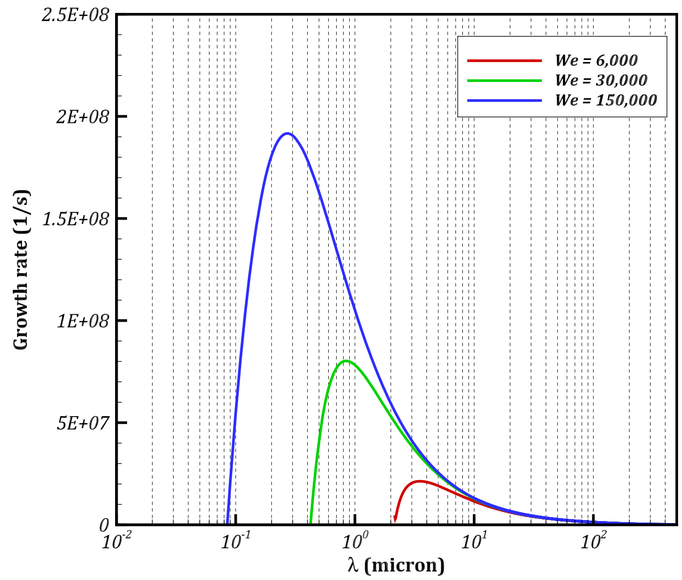

Figure 3.19: Linear growth rate as a function of wavelength based on VPF instability analysis of Joseph et al. [4]. $Re = 15,000$, $\hat{\rho} = 0.05$, $\hat{\mu} = 0.0066$, $\hat{d} = 0.8$.

set) in different instances of time after the injection. The surface tension in the left column of Fig. 3.20 (a) is 25 times the surface tension of the right column (b). As can be seen from the figure, both cases demonstrate similar behavior in terms of radial/axial penetration and size of the jet. The size of the ligaments and the amount of pinched-off rings (2D drops), however, vary drastically. The higher instabilities for the higher We case are obvious from the early stages of injection $t^* = 25$. At this time instant, the mushroom-shaped cap has formed and grown in both cases. The higher We jet shows lots of small scale instabilities (RT instabilities) on the back of its cap, which produce thin ligaments and small droplets broken-up from them. In the lower We jet, however, the edge of the cap has stretched and curved back without any breakup, and a few larger waves have emerged on the back of its cap. The broken-up rings and ligaments, in the higher We case, collide on the main jet stem; these impacts trigger more instabilities on the surface of the liquid jet, later in time.

At $t^* = 30$ the mushroom-shaped cap deforms and this deformation continues up to $t^* = 35$. At the meantime, more instabilities appear and grow on the back of the cap, as well as on the

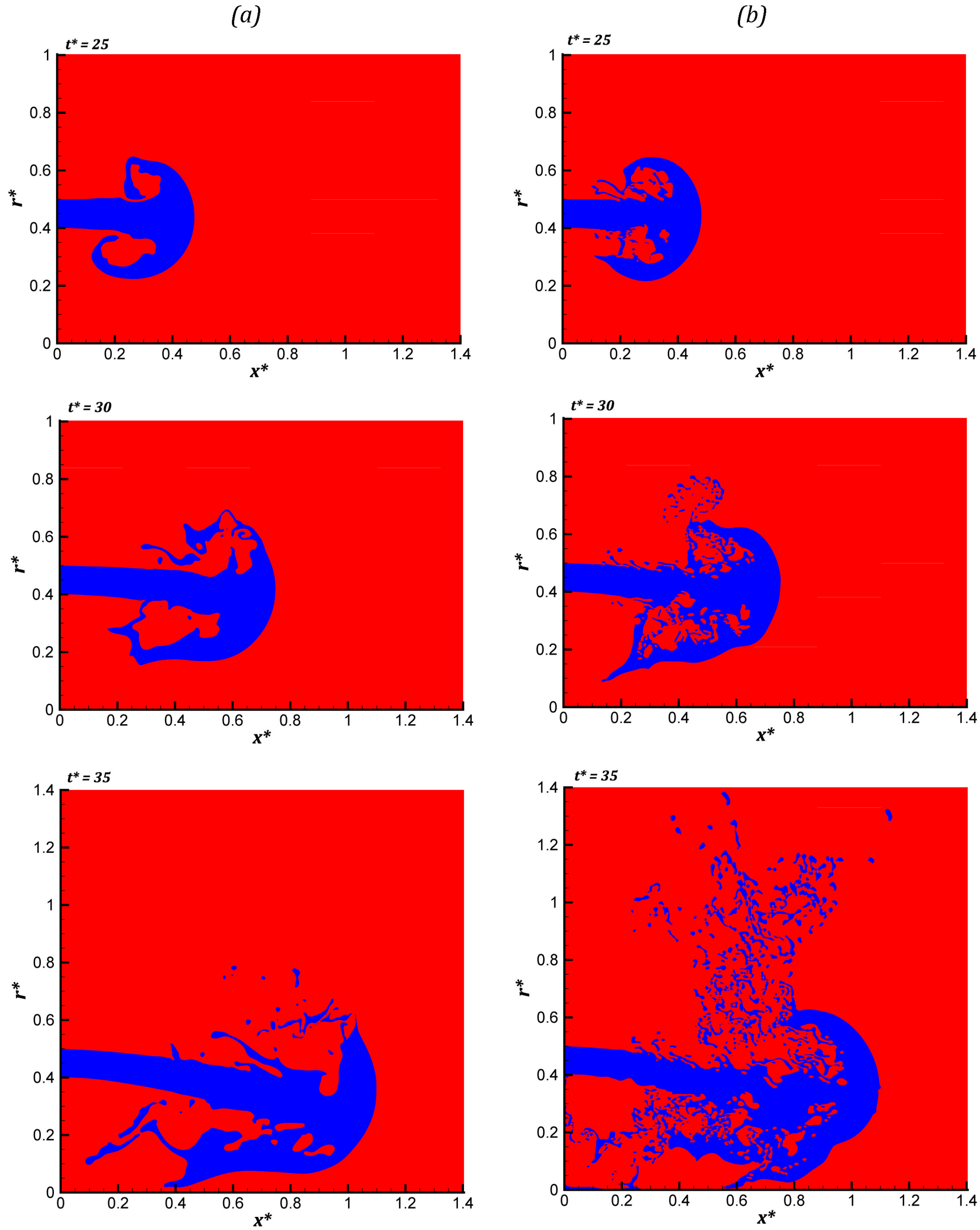

Figure 3.20: Jet development at $t^* = 25$ (top), $t^* = 30$ (middle) and $t^* = 35$ (bottom). $Re = 15,000$, $\hat{\rho} = 0.05$, $\hat{\mu} = 0.0066$, $\hat{d} = 0.8$; (a) $We = 6000$, (b) $We = 150,000$.

liquid sheet. The surrounding gas is entrained behind the jet cap, on both top and bottom sides, while vortices are shed from the edge of the curved cap. As the vortices grow larger, they catapult rings, which are pinched-off from the surface of the higher We jet, and stretch back the liquid ligaments, in the lower We jet. This phenomenon will be discussed in more detail, later in this section.

The normalized wavelength (λ/h) spectrum of unstable KH and RT instabilities during the start-up period of injection have been plotted in Figure 3.21 for the three We cases. The RT instabilities at the back of the jet cap are more pronounced at the early stages of injection

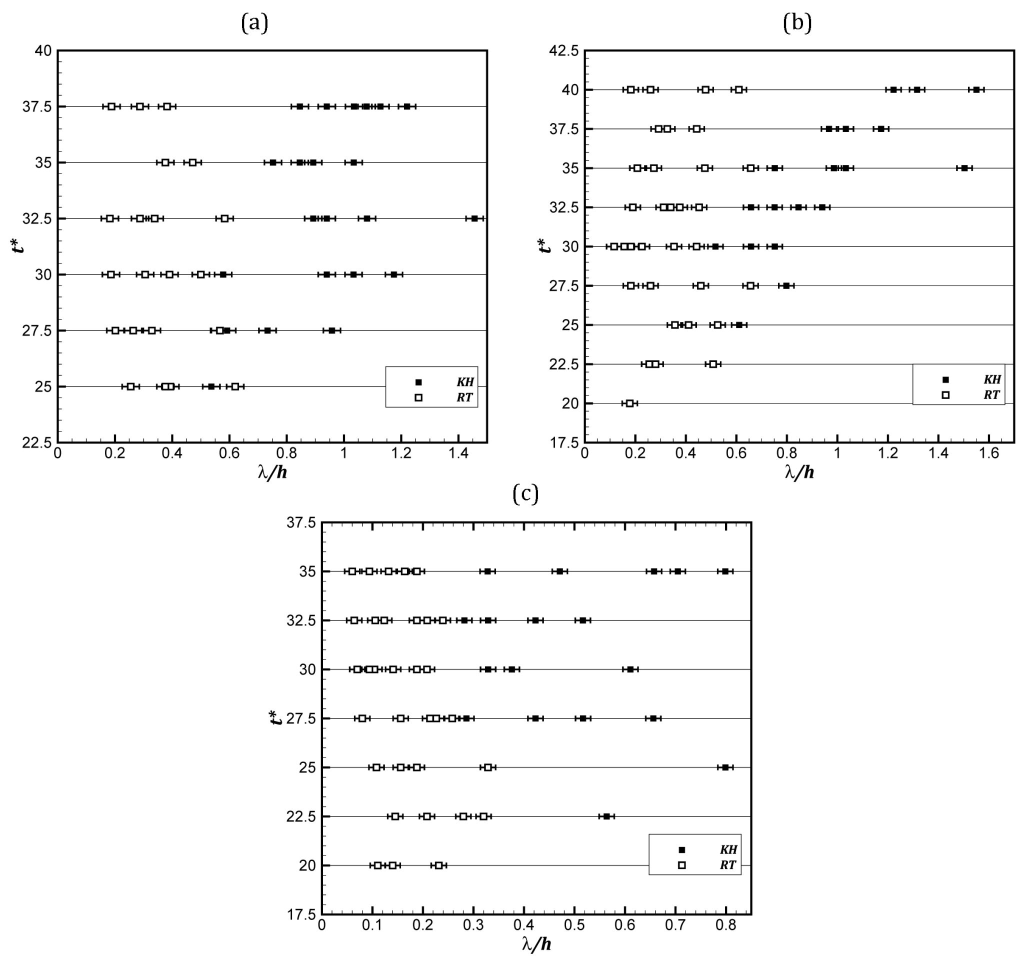

Figure 3.21: Dimensionless KH and RT wavelength spectrum during start-up vs. time; the error bars correspond to 5% and $h = 50\ \mu m$. $Re = 15,000$, $\hat{\rho} = 0.05$, $\hat{\mu} = 0.0066$, $\hat{d} = 0.8$; $We = 6000$ (a), $We = 30,000$ (b), $We = 150,000$ (c).

$t^* = 20$–25. The instabilities occur sooner in the higher We jets, compared to the lower We ones (compare $t^* = 20$ in Fig. 3.21c with $t^* = 25$ in Fig. 3.21a). The plots in Fig. 3.21 indicate that, in all the cases, the average wavelength of the distinguished RT instabilities decrease with time, while the average wavelength of the observed unstable KH waves increase.

The set of all of the observed KH and RT instabilities' wavelengths, for each We number, are illustrated in Figure 3.22, on a semi-log plot. As this figure demonstrates, the overall wavelength of both KH and RT instabilities decrease with increasing the We number. The range of the KH instabilities is $0.6h$–$1.5h$ for $We = 6000$, $0.5h$–$1.5h$ for $We = 30,000$ and $0.4h$–$0.8h$ for $We = 150,000$. For the shorter RT instabilities, the smallest distinguished wavelength is $0.2h$ (10 μm), $0.1h$ (5 μm), and $0.06h$ (3 μm) for We = 6000, 30,000 and 150,000, respectively. It should be mentioned that in all of the waves (instabilities), that have been considered in this report, it has been tried to exclude the waves that have appeared or have been influenced by the collision of broken-up rings and ligaments on the liquid jet stem.

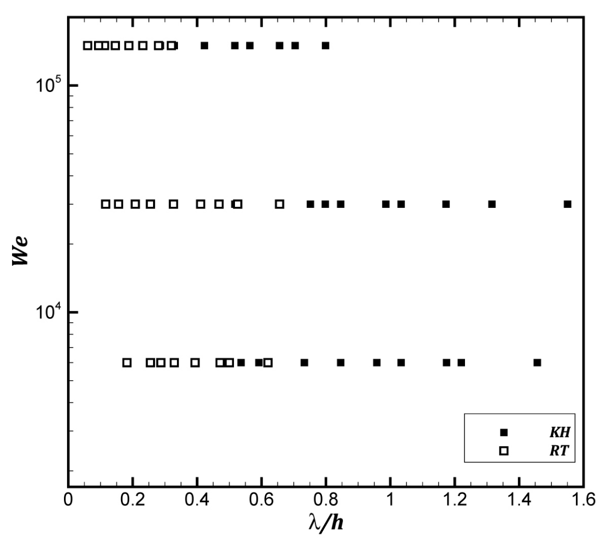

Figure 3.22: Dimensionless KH and RT wavelength spectrum during start-up vs. the We number. $h = 50\ \mu m$, $Re = 15,000$, $\hat{\rho} = 0.05$, $\hat{\mu} = 0.0066$, $\hat{d} = 0.8$; (the plot is in semi-log scale).

3.2.3 Droplet ejection mechanism

Figure 3.23 shows the mechanism that ejects the liquid rings (2D droplets) from the back of the liquid jet cap during the start-up period of injection. As could be seen in this figure, the gas that has been entrained on the back of the liquid jet cap, creates a recirculation zone with a series of smaller vortices, on both inner and outer sides of the jet (only the outer surface vortices are shown in this figure). The small disturbances on the liquid/gas interface grow into Kelvin-Helmholtz waves, and the wave crest forms a thin liquid film that flaps as the wave grows radially outward. The film breaks up into rings which are eventually thrown into the gas stream at large angles. A similar phenomenon happens on the liquid sheet stem and the vortex mechanism is responsible for ejecting the rings and ligaments in the upstream direction from the crest of the KH waves. The interaction between the vortices and the KH waves on the back of the jet cap and the jet stem are shown in Figure 3.24 for $We = 6000$ at $t^* = 32.5$.

The vortex catapult mechanism was also reported by Jerome et al. [80]; however, they

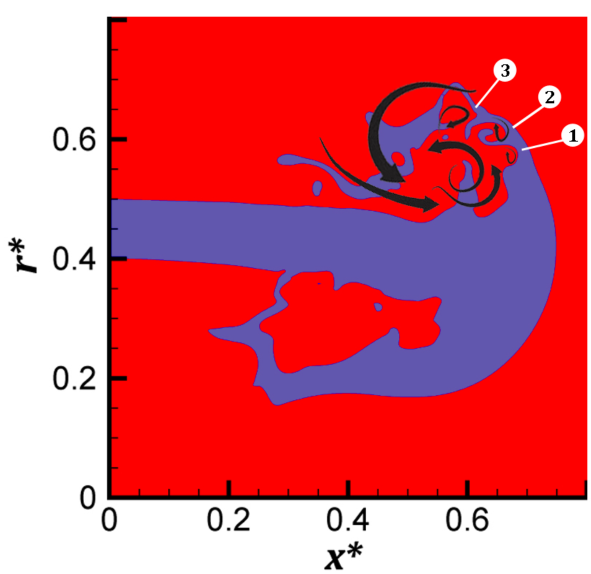

Figure 3.23: A schematic of the vortex catapult mechanism on the back of the liquid jet cap.

examined such mechanism in a planar two-phase mixing layer. A recirculation region grows downstream of the wave and leads to vortex shedding similar to the wake of a backward-facing step. The ejection mechanism results from the interaction between the liquid film and the vortex shedding sequence: a recirculation zone appears in the wake of the wave (stage 1 in Fig. 3.23) and a liquid film emerges from the wave crest (stage 2); the recirculation region detaches into a vortex and the gas flow over the wave momentarily reattaches due to the departure of the vortex (stage 3); this reattached flow pushes the liquid film down; by now, a new recirculation vortex is being created in the wake of the wave, just where the liquid film is now located; the liquid film is blown up from below by the newly formed recirculation vortex in a manner similar to a bag-breakup event; the resulting droplets are catapulted by the recirculation vortex [80].

Figure 3.25 shows the velocity vectors near the liquid jet interface region, and the vortices

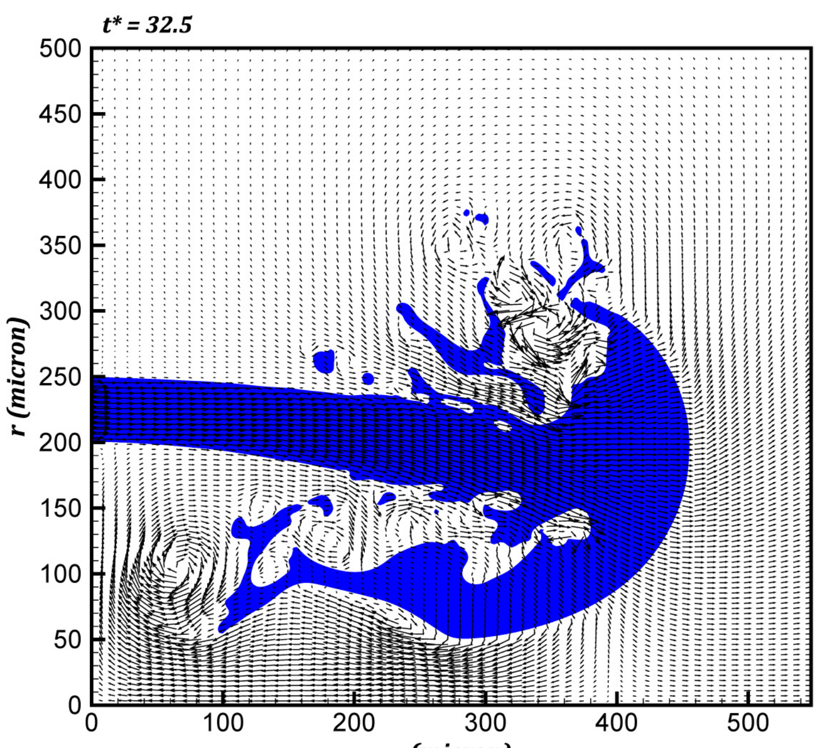

Figure 3.24: Velocity vectors close to the liquid jet interface, showing the droplet ejection mechanism. $Re = 15,000$, $We = 6000$, $\hat{\rho} = 0.05$, $\hat{\mu} = 0.0066$, $\hat{d} = 0.8$.

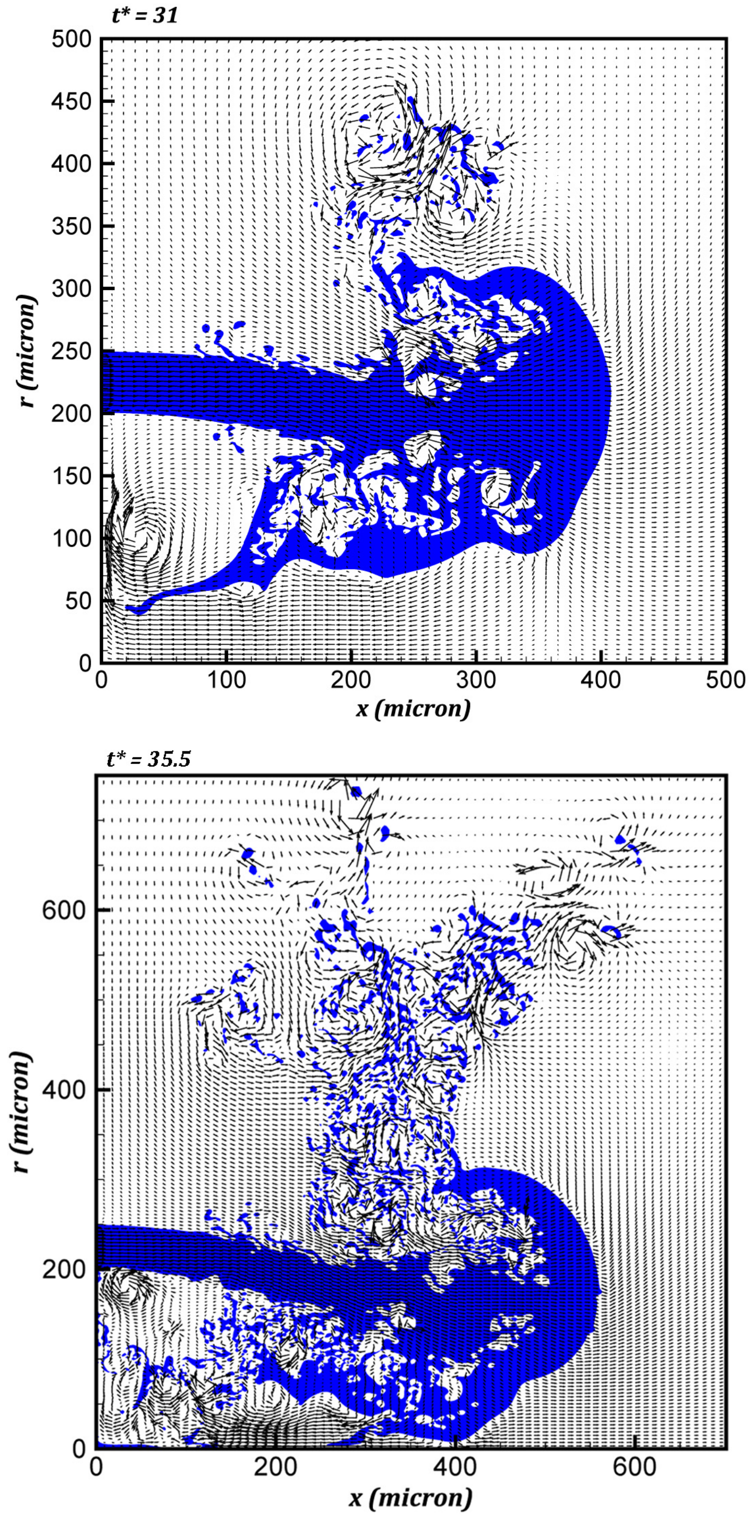

Figure 3.25: Velocity vectors close to the liquid jet interface, showing the droplet ejection mechanism at two time instants. $Re = 15,000$, $We = 150,000$, $\hat{\rho} = 0.05$, $\hat{\mu} = 0.0066$, $\hat{d} = 0.8$.

that are shed at the back of the jet cap, for $We = 150,000$, at two time instants. At high Re jets, like the ones in this study, the RT effects also assist the KH instabilities to grow on the back of the jet, and intensify the droplet ejection mechanism. As the We number increases, the vortices overcome the surface tension forces that tend to keep the liquid ligaments/drops attached to the liquid main body. As a result, vortices are detached more easily from the wakes of KH and RT instabilities. This is shown in Figure 3.25 at $t^* = 31$. The detached vortices on the back of the jet cap (and on the liquid sheet stem) catapult the rings and smaller ligaments radially outward (and axially upstream).

As time elapses, the instabilities grow, while their wavelengths decrease, on the back of the jet. The bottom picture in Figure 3.25 shows the shed vortices and the rings that are carried outward and thrown into the surrounding gas by them, at $t^* = 35.5$. In a flow where most of the momentum is in the axial direction, it is surprising to observe these large ejection angles in the radial direction. The interaction between the vortex shedding and the opposing liquid film forces (viscose and surface tension forces) determines whether a liquid ring is detached and catapulted into the gas or a liquid ligament is stretched upstream without breaking up. The complete development stages of the annular jet are presented in Appendix B, for the two We cases.

3.3 Density ratio effects

The importance of the density ratio in an annular liquid jet flow and the growth of the instabilities on the liquid/gas interface are discussed in this section. The density ratio, in this study, has been defined as the ratio of the gas density over the liquid density $\hat{\rho} = \rho_g/\rho_l$. Hence, an increase in the density ratio corresponds to a decrease in the difference between the gas and liquid densities. Some studies in the literature might prefer to define this parameter as the reciprocal of what is used here.

Three different density ratios have been studied in this research; $\hat{\rho} = 0.05$, 0.1 and 0.9. The first value corresponds to the ratio of high pressure air density to liquid Kerosene density. The last chosen value represents an almost like-density liquid and gas case. The complete steps of the jet development process for theses cases are given in Appendix C.

3.3.1 Jet penetration and convergence

Figure 3.26 shows the difference between the liquid/gas interfaces of a jet with $\hat{\rho} = 0.1$ (a) and $\hat{\rho} = 0.05$ (b) at three different times after the start of the injection. As the figure demonstrates, both jets show a similar overall behavior in the sense of position of the interface in time. However, the case with lower density ratio has higher penetration (axial growth) and convergence (radial growth) at comparable times. The bottom sub-figures in Fig. 3.26 clearly show that the jet with $\hat{\rho} = 0.1$ (left) has just collapsed on the centerline, while the lower density ratio jet (right) has converged at an earlier time and is growing along the centerline. In terms of the instabilities and ligaments' sizes, the jet with lower density ratio demonstrates more instabilities, with thinner liquid ligaments and more pinched-off liquid drops. The KH instabilities, on the liquid sheet surface, have the same pattern for both cases; however, the waves on the lower density ratio jet have shorter wavelengths compared to the other case.

When the difference between the liquid and gas density diminishes ($\hat{\rho}$ increases), the behavior of the jet changes completely. This is shown in Figure 3.27, where the liquid interface for $\hat{\rho} = 0.9$ at three time instants are shown along with their vorticity contours. The first thing to notice in this figure is that, the instabilities occur much later in time (compare $t^* = 45$ for this case with $t^* = 30$ in the previous cases). The instabilities (mostly Kelvin-Helmholtz) have much longer wavelengths and grow much faster than the former cases. It is also interesting to note that, because of the similarity in the density of the liquid and the gas,

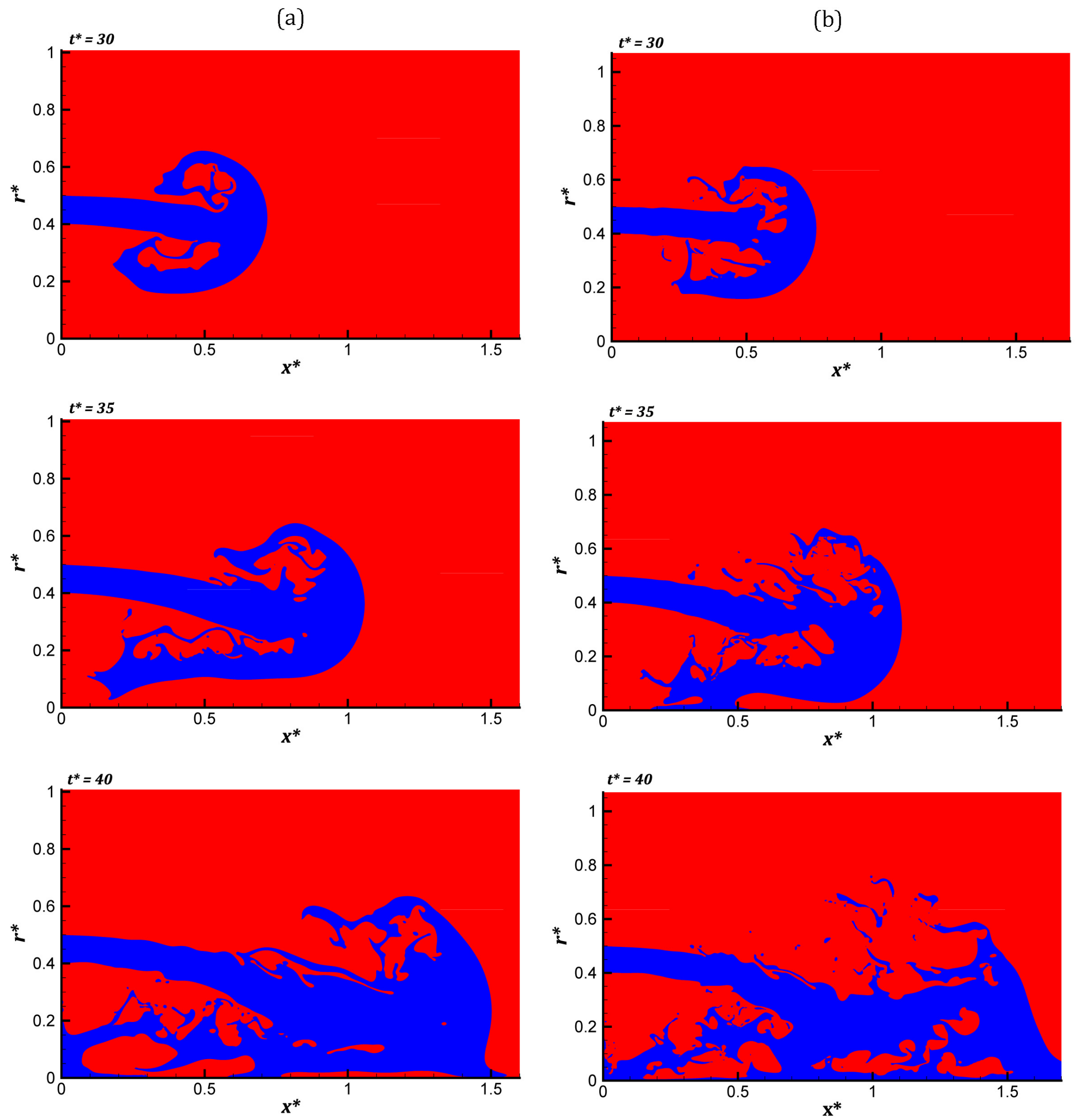

Figure 3.26: Jet development at $t^* = 30$ (top), $t^* = 35$ (middle) and $t^* = 40$ (bottom). $Re = 15,000$, $We = 30,000$, $\hat{\mu} = 0.0066$, $\hat{d} = 0.8$; (a) $\hat{\rho} = 0.1$, (b) $\hat{\rho} = 0.05$.

the jet cap inflates and the jet floats in the gas. It is apparent in this figure that the liquid jet diverges gradually (spreads into the gas) instead of converging towards the centerline.

The vortices that are generated because of large velocity gradient on the liquid/gas interface, are shed near the nozzle exit. The counter-vortices then grow as they are convected downstream by the main flow. Eventually these vortices spread into the surrounding gas by the effects of advection and viscosity. The frequency of the shed vortices depends on the

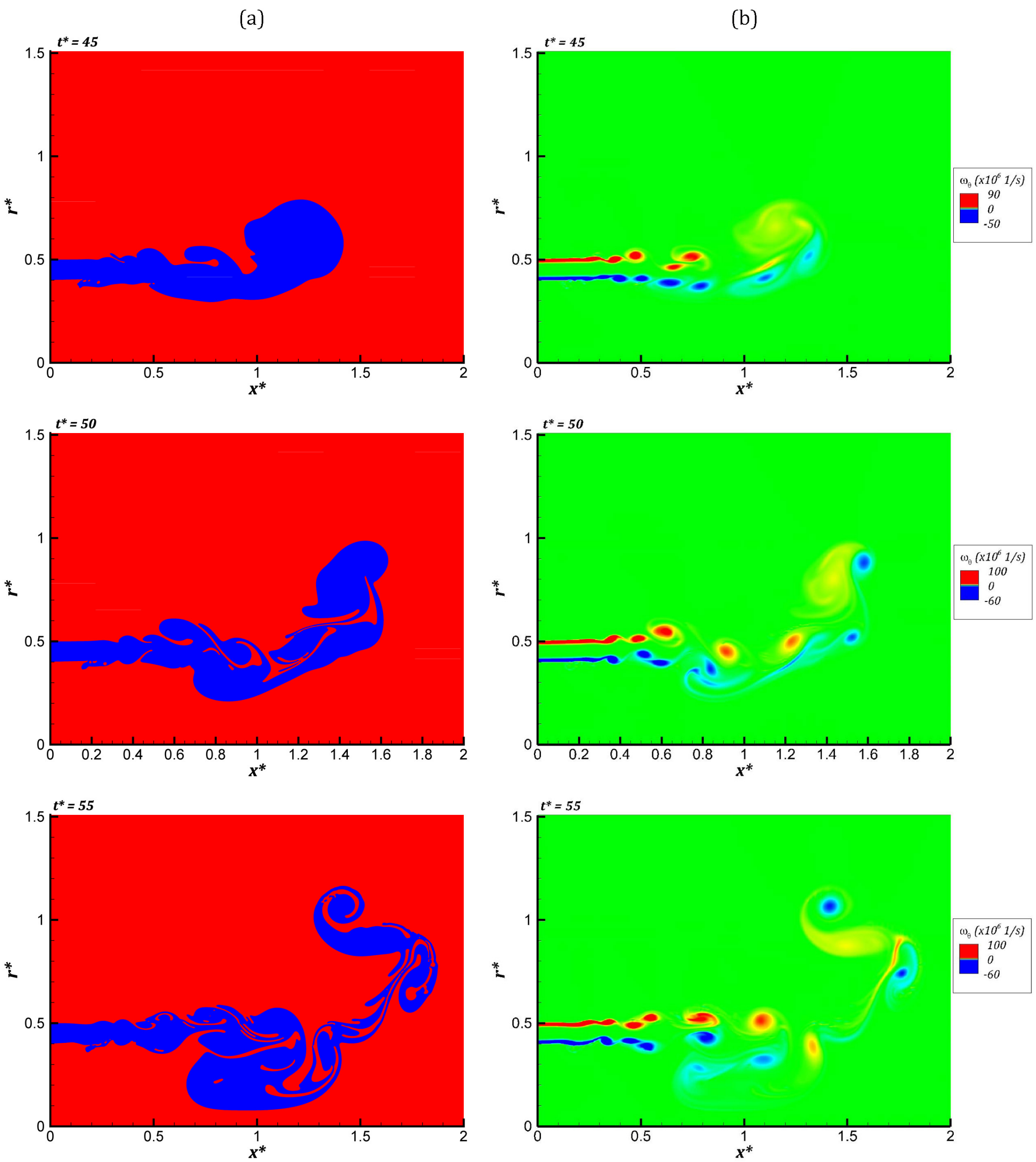

Figure 3.27: Jet development at $t^* = 45$ (top), $t^* = 50$ (middle) and $t^* = 55$ (bottom). $Re = 15,000$, $We = 30,000$, $\hat{\rho} = 0.9$, $\hat{\mu} = 0.0066$, $\hat{d} = 0.8$; (a) liquid/gas interface, (b) azimuthal vorticity.

flow Re number; increasing with an increase in the jet Reynolds number. Although this case is not of much interest in this study, as well as in many other applications such as fuel injection, the results of this case are included in the comparisons for the sake of consistency and pedagogy.

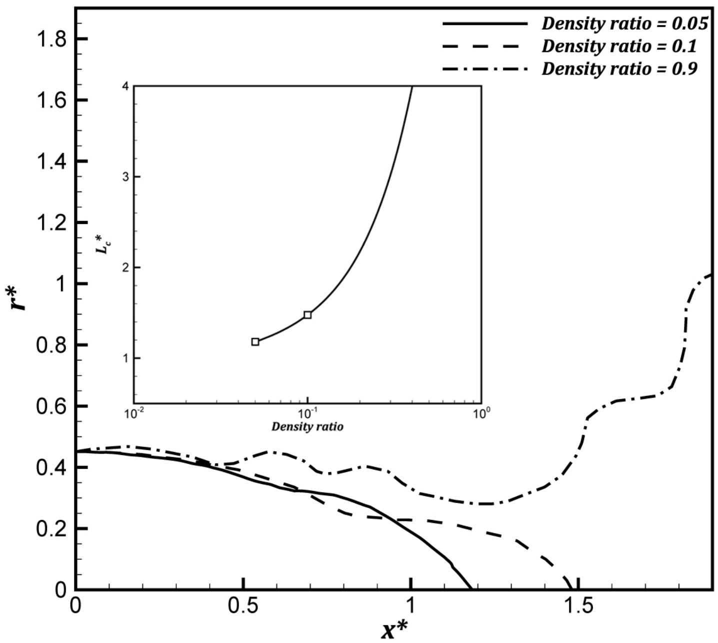

Figure 3.28: Axial variation of the dimensionless radius for different density ratios (the main plot); comparison between the convergence lengths of different density ratio cases (the sub-figure). $Re = 15,000$, $We = 30,000$, $\hat{\mu} = 0.0066$, $\hat{d} = 0.8$.

The comparison between the axial variation of the liquid sheet radius for jets with different density ratios is given in Figure 3.28. As could be seen in this figure, the case with like-density gas and liquid does not converge on the centerline. The convergence length of the liquid annulus versus the density ratio is plotted in the sub-figure of the same figure. This figure shows that the gas/liquid density ratio is an important parameter influencing the convergence length. As the density ratio increases, the convergence length grows with an increasing slope. The case with $\hat{\rho} = 0.05$ collapses at $x^* \approx 1.2D$, while the jet with $\hat{\rho} = 0.1$ converges at $x^* \approx 1.5D$.

The same story as for the convergence length, goes on for the convergence rate of the three annular jets, as is shown in Figure 3.29. The jet with $\hat{\rho} = 0.05$ converges after $t^* \approx 36$, and the convergence time increases with density ratio, such that the jet with $\hat{\rho} = 0.1$ converges at $t^* \approx 40$. The liquid jet with the highest density ratio does not converge by the end of the time that was considered for the computations.

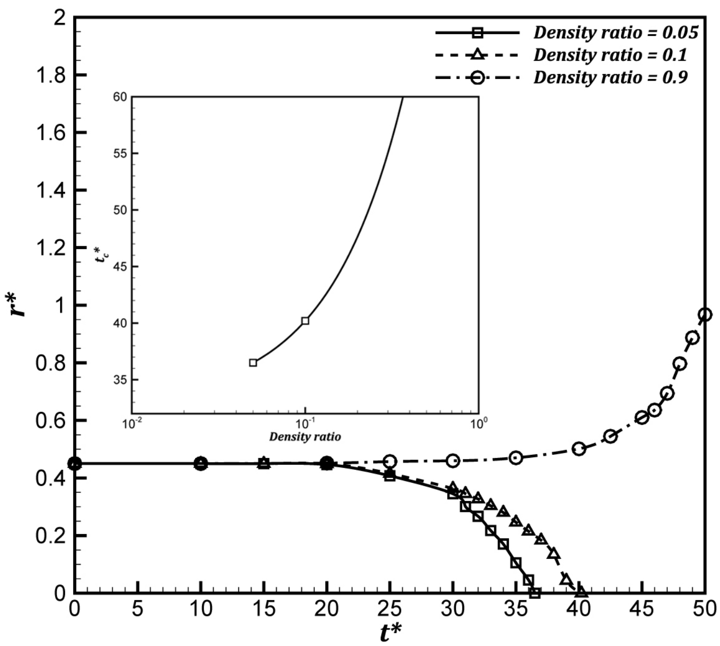

Figure 3.29: Variation of the dimensionless radius of the annular jet tip versus dimensionless time, for different density ratios (the main plot); comparison between the convergence rate of different density ratio cases (the sub-plot). $Re = 15,000$, $We = 30,000$, $\hat{\mu} = 0.0066$, $\hat{d} = 0.8$.

The axial penetration versus time of the three jets are compared in Figure 3.30. Unlike the Re and We numbers, it is apparent that the density ratio does affect the axial penetration

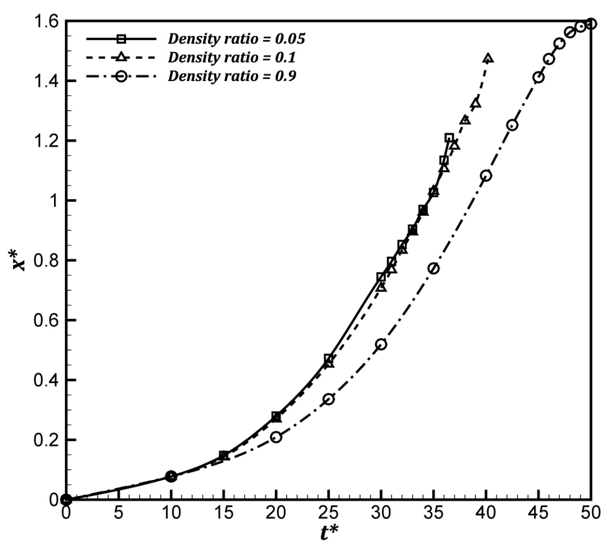

Figure 3.30: Axial penetration of the annular jet versus dimensionless time, for jets with different density ratios. $Re = 15,000$, $We = 30,000$, $\hat{\mu} = 0.0066$, $\hat{d} = 0.8$.

rate of the annular liquid jet. As was mentioned earlier, and is shown in the figure, the lower density ratio jet penetrates more compared to the higher ones. Thus, at the same time, longer liquid jet is produced by lowering the gas/liquid density ratio. The reason is that the liquid jet with lower density ratio has higher momentum relative to the gas medium, consequently, higher axial penetration is rendered. Also notice that, for the highest density ratio jet, the axial penetration is ceased (decelerated) after $t^* \approx 45$ and the jet grows more in the radial direction, as was shown in Fig 3.27.

3.3.2 Density ratio and the instabilities

As in the previous sections, it would be instructive to first study the linear analysis predictions of the growth rates. The instabilities' growth rate for different density ratios are given as a function of the instabilities' wavelength, based on the linear VPF instability analysis of Joseph et al. (eqn. 3.1), in Figure 3.31.

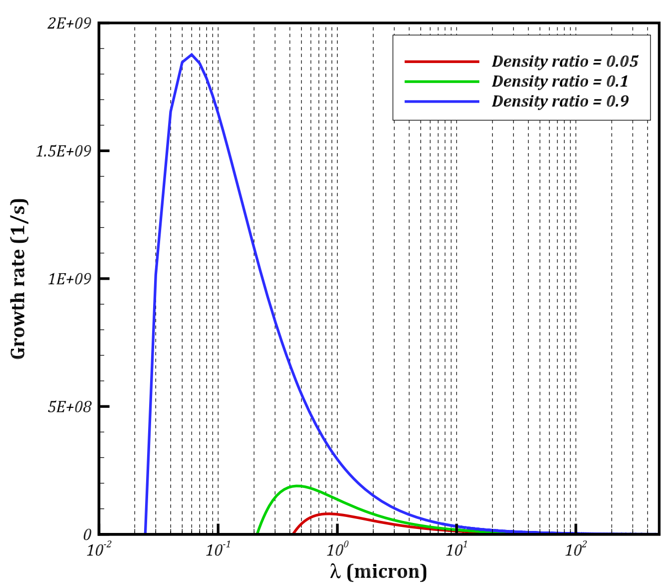

Figure 3.31: Linear growth rate as a function of wavelength for different density ratios, based on VPF instability analysis of Joseph et al. [4]. $Re = 15,000$, $We = 30,000$, $\hat{\mu} = 0.0066$, $\hat{d} = 0.8$.

As the figure shows, both the range of the unstable wavelengths and the growth rate of the waves increase with increasing the density ratio. The fact that the instabilities grow faster in the highest density ratio jet ($\hat{\rho} = 0.9$) is consistent with our numerical results, as was evident in Fig. 3.27. However, smaller unstable waves were not observed in this case, opposing what the linear analysis suggests. In fact, the wavelength of the instabilities that are observed in Fig. 3.27 for $\hat{\rho} = 0.9$ are much larger than the two other cases with lower density ratios (Fig. 3.26). Yet the linear analysis is in accordance with this observation, since it predicts that even the instabilities with larger wavelengths have higher growth rate in high density ratio compared to the negligible growth rate of low density ratio instabilities. Later in this section, we will see that, for the highest density ratio case, the numerical results show unstable waves with wavelengths twice the value of the maximum wavelengths that were observed so far.

Figure 3.32 shows the dimensionless KH and RT wavelengths that were observed in the start-up period of injection for the three density ratio jets, separately. As indicated earlier, the instabilities emerge later in time for higher density ratios. Compare the first instabilities appearing at $t^* = 20$ for $\hat{\rho} = 0.05$, with $t^* = 25$ and 42.5 for $\hat{\rho} = 0.1$ and 0.9, respectively.

The average wavelength of the KH instabilities grows larger in time, in all the cases. The RT instabilities, however, remain in almost the same range at all of the time stages. The number of observed RT instabilities are much less than the KH instabilities in $\hat{\rho} = 0.9$ case; indicating that the KH instability is dominant at very high density ratio jets. The average wavelength of both KH and RT instabilities also grow with the density ratio, as is shown in Figure 3.33. The largest unstable wave that has been distinguished for the lowest density ratio jet, has a wavelength of $1.6h$, while this value grows to $2.2h$ for $\hat{\rho} = 0.1$. The jet with the highest density ratio has unstable KH waves with wavelengths 4 times the thickness of the liquid sheet; i.e. 200 μm. The complete steps of the jets' evolution process could be found in Appendix C.

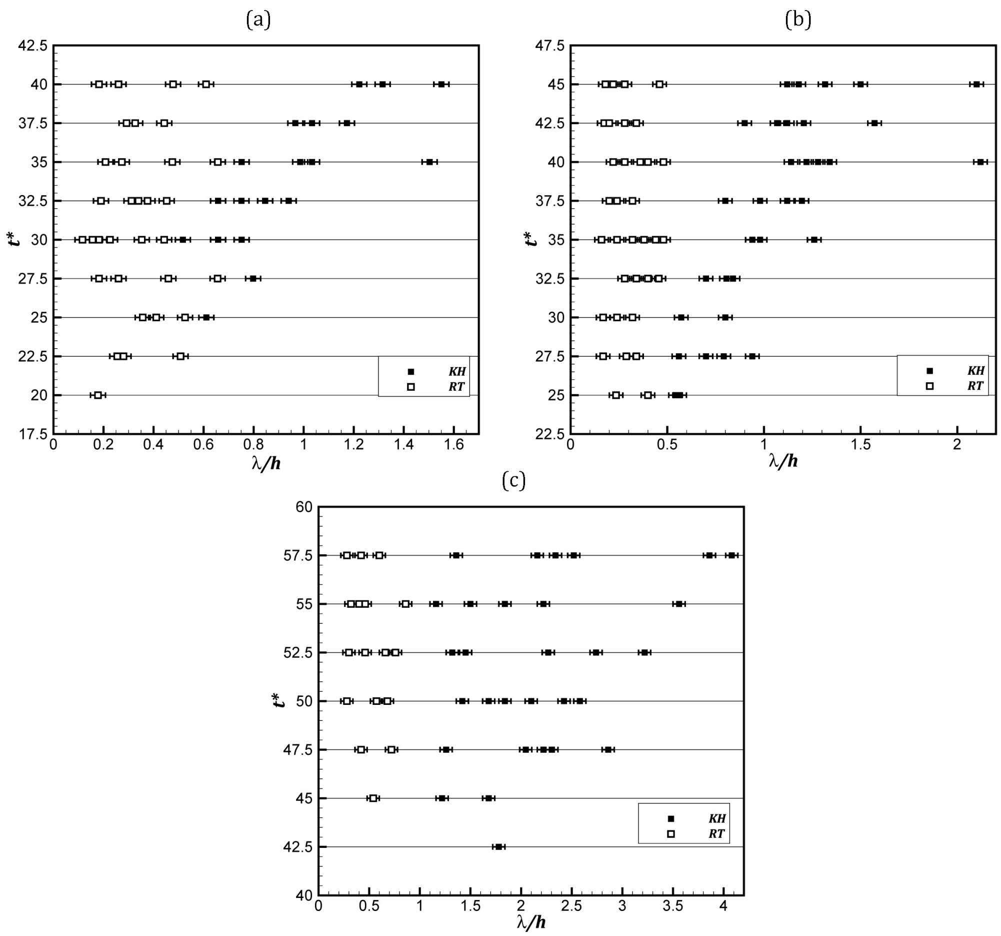

Figure 3.32: Dimensionless KH and RT wavelength spectrum vs. time; the error bars correspond to 5% and $h = 50\ \mu m$. $Re = 15,000$, $We = 30,000$, $\hat{\mu} = 0.0066$, $\hat{d} = 0.8$; $\hat{\rho} = 0.05$ (a), $\hat{\rho} = 0.1$ (b), $\hat{\rho} = 0.9$ (c).

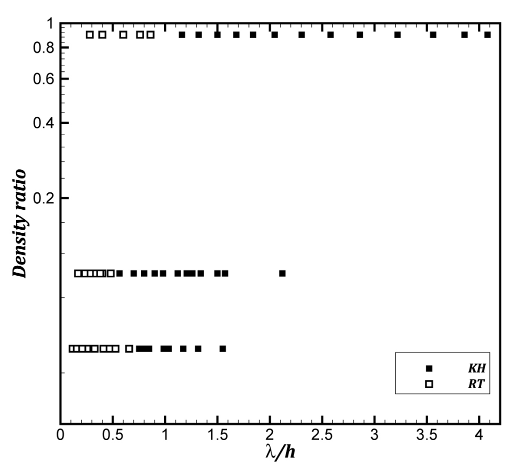

Figure 3.33: Dimensionless KH and RT wavelength spectrum during start-up vs. gas to liquid density ratio. $h = 50\ \mu m$, $Re = 15,000$, $We = 30,000$, $\hat{\mu} = 0.0066$, $\hat{d} = 0.8$; (the plot is in semi-log scale).

3.4 Viscosity ratio effects

Similar to the density ratio, the viscosity ratio is defined as the ratio of the gas viscosity to the liquid viscosity in this study, $\hat{\mu} = \mu_g/\mu_l$. The three viscosity ratios that are compared in this research are 0.0001, 0.0066 and 0.05. The first value represents an almost inviscid gas case, while the last value is chosen to mimic a highly viscous gas (keeping the liquid viscosity constant). The intermediate value equals the viscosity ratio of high pressure air and liquid Kerosene (properties given in Table 2.1). The effects of viscosity ratio variation on the annular jet flow characteristics are discussed in this section. The complete picture of the jet development steps for the aforementioned cases are given in Appendix D.

3.4.1 Jet penetration and convergence rate

The results of radial position of the liquid sheet, with respect to the axial distance from the nozzle exit and with respect to the injection time, are given in Figures 3.34 and 3.35, respectively, for the three cases. These results indicate that the viscosity ratio has only a minor influence on the annular jet convergence characteristics; the convergence length and the convergence rate.

The sub-plots in Figures 3.34 and 3.35 show that, both the convergence length L_c^* and convergence time t_c^*, increase slightly with increase of the viscosity ratio. Notice that the convergence length difference between the three cases is just about 0.03 of the jet diameter ($\approx$ 15 μm), while each of the viscosity ratios are an order of magnitude different from the other. In a sense, we could claim that the viscosity ratio has negligible effect on the convergence length. All of the jets converge at about $L_c^* \approx 1.18D$.

The effect of viscosity ratio on the convergence rate of the liquid sheet is also negligible. The jet with the highest viscosity ratio convergences only less than a microsecond after the jet

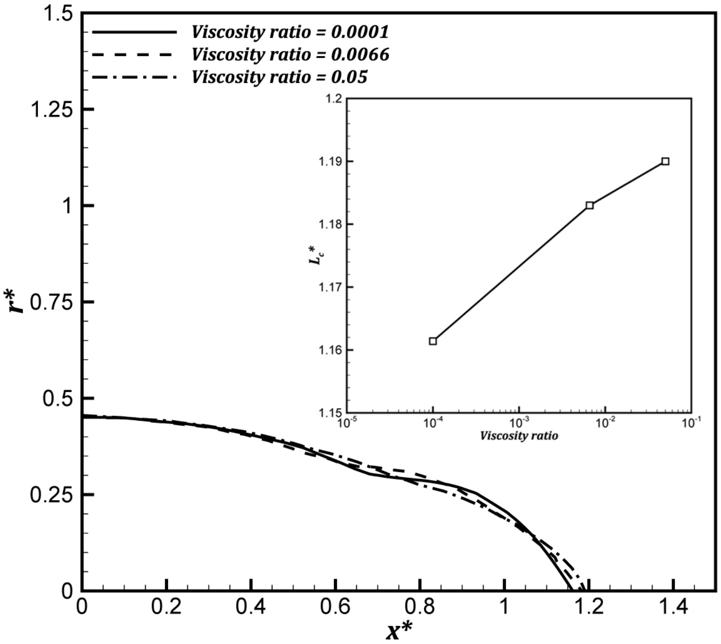

Figure 3.34: Axial variation of the dimensionless radius for different viscosity ratios (the main plot); comparison between the convergence lengths of different viscosity ratio cases (the sub-figure). $Re = 15,000$, $We = 30,000$, $\hat{\rho} = 0.05$, $\hat{d} = 0.8$.

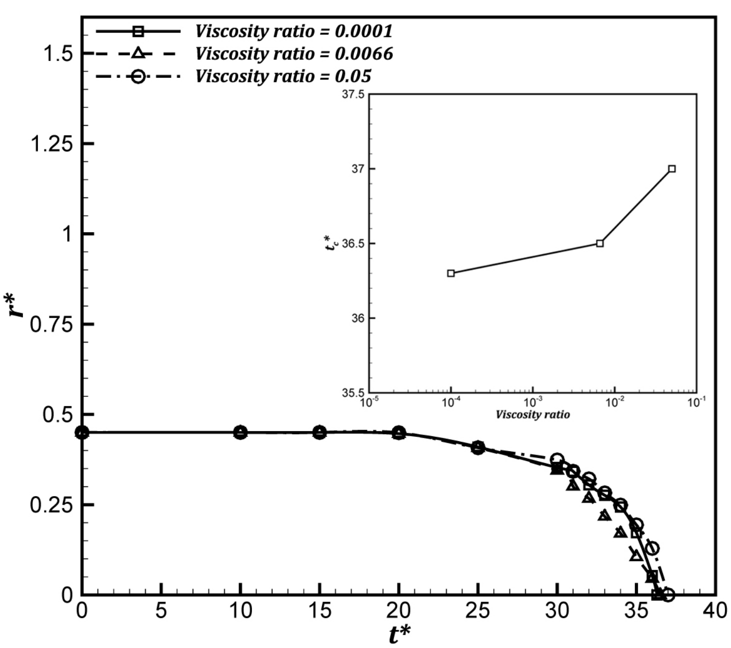

Figure 3.35: Variation of the dimensionless radius of the annular jet tip versus dimensionless time, for different viscosity ratios (the main plot); comparison between the convergence rate of different viscosity ratio cases (the sub-plot). $Re = 15,000$, $We = 30,000$, $\hat{\rho} = 0.05$, $\hat{d} = 0.8$.

with the lowest viscosity ratio; the difference between the viscosity ratios of the two cases are two orders of magnitude, though. All three cases collapse on the centerline at $t_c^* \approx 36.5$ after the start of injection.

In terms of the axial penetration, the three jets with different viscosity ratios also give the same performance, as is shown in Figure 3.36. This figure shows that, the axial penetration of all three jets match perfectly at early time instants $t^* < 30$. For $30 < t^* < 40$, although not perfectly, the three cases match very closely. These results, and the results of the radial penetration given before, show that the length of the liquid jet is almost independent of the gas/liquid viscosity ratio, for the range of flow parameters that have been studied in this research.

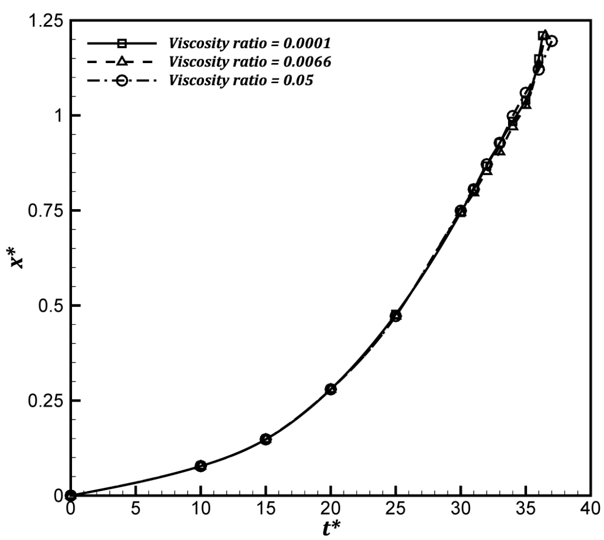

Figure 3.36: Axial penetration of the annular jet versus dimensionless time, for jets with different viscosity ratios. $Re = 15,000$, $We = 30,000$, $\hat{\rho} = 0.05$, $\hat{d} = 0.8$.

3.4.2 Viscosity ratio and the instabilities

The linear viscous potential flow analysis results of Joseph et al. [4], shown in Figure 3.37, indicate that the viscosity ratio has negligible effect on the growth rate of the instabilities, as well as the range of unstable wavelengths. The increase in the growth rate of comparable

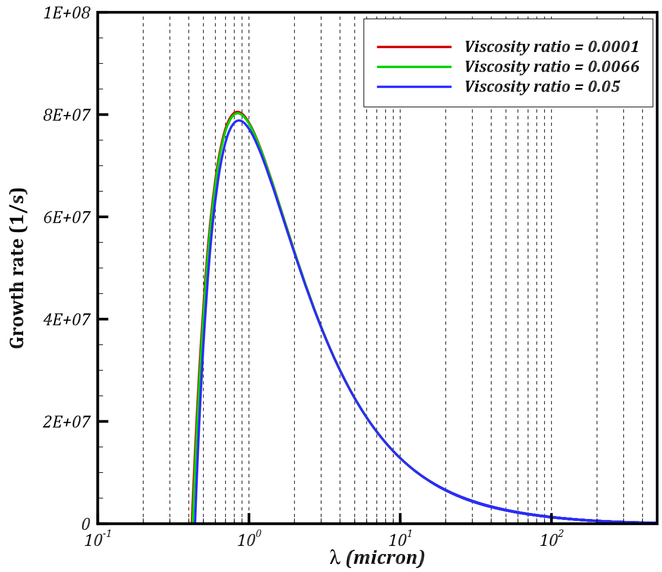

Figure 3.37: Linear growth rate as a function of wavelength for different viscosity ratios, based on VPF instability analysis of Joseph et al. [4]. $Re = 15,000$, $We = 30,000$, $\hat{\rho} = 0.05$, $\hat{d} = 0.8$.

wavelengths, from the higher viscosity ratio jets to the lower ones, is very small, so that the linear analysis suggests that we should statistically see the same range of wavelengths and growth rates in all three cases.

The comparison between the liquid jets' interface for the jets with $\hat{\mu} = 0.0001$ and $\hat{\mu} = 0.05$, at three instants of injection, are given in Figure 3.38. At $t^* = 30$, and before that, the two jets look almost the same. However, the liquid jet with lower viscosity ratio (a) shows thinner and more elongated ligaments near the curled edges of the jet cap, compared to the high viscosity ratio jet (b). Also notice the earlier appearance of the Kelvin-Helmholtz waves on the stem of the liquid sheet in the jet with lower viscosity ratio (Fig. 3.38a, at $t^* = 30$). These waves could be tracked up to $t^* = 32.5$, where the KH waves have grown on the surface of the low viscosity ratio jet (a), while the instabilities on the liquid sheet with higher viscosity ratio are just about to emerge (b). Both jets have penetrated the same axial distance at this time.

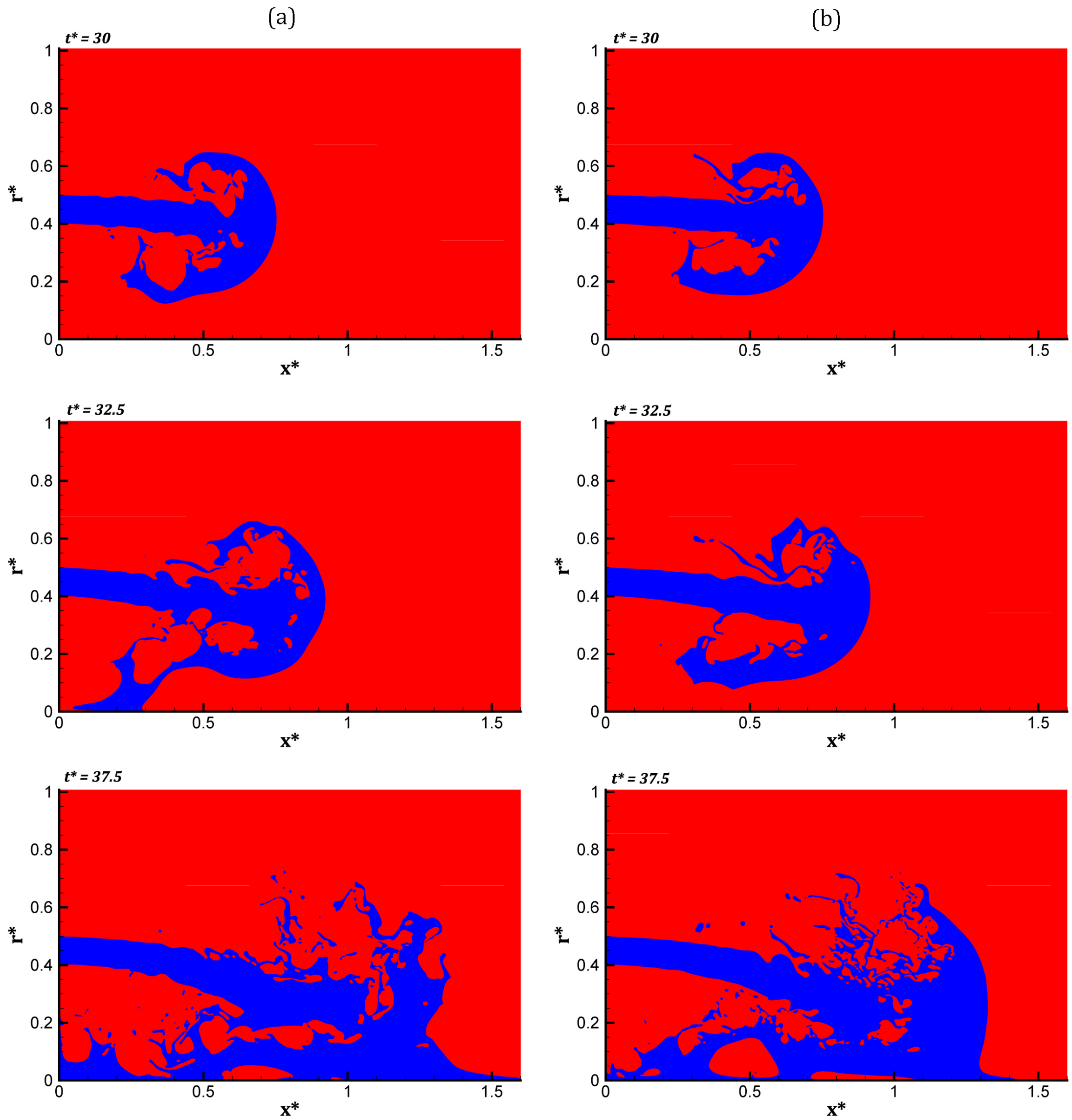

Figure 3.38: Jet development at $t^* = 30$ (top), $t^* = 32.5$ (middle) and $t^* = 37.5$ (bottom). $Re = 15,000$, $We = 30,000$, $\hat{\rho} = 0.05$, $\hat{d} = 0.8$; (a) $\hat{\mu} = 0.0001$, (b) $\hat{\mu} = 0.05$.

Later at $t^* = 37.5$, we can see that the jet with lower viscosity ratio deforms more quickly. The mushroom-shaped cap of the jet with $\hat{\mu} = 0.0001$ deforms severely and looses its curved smooth form at its leading edge. The liquid jet with higher viscosity ratio, however, still holds its mushroom-shaped cap in its original form up to this time. A few recognizable KH waves on both inner and outer sides of the liquid sheet surface are apparent for the jet with high viscosity ratio (b), at this time. Following these waves until $t^* = 40$ (Fig. D2 in Appendix

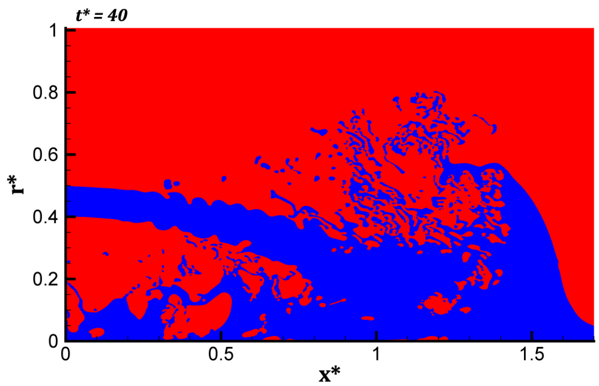

Figure 3.39: KH waves on the jet interface at $t^* = 40$. $Re = 15,000$, $We = 30,000$, $\hat{\rho} = 0.05$, $\hat{\mu} = 0.05$, $\hat{d} = 0.8$.

D), we can see in Figure 3.39 that, the wavelength of these KH waves decreases as they move upstream, and a series of KH waves with almost same size appear on both inner and outer sides of the sheet. The wavelength of the instabilities on the inner surface being longer and with smaller amplitudes, compared to the outer surface waves. Both inner and outer waves grow in amplitude but diminish in wavelength as they move upstream with respect to the jet. The whole picture of the liquid sheet at this time, suggests that the instabilities are in a mode between sinuous (anti-symmetric) and varicose (symmetric) modes (refer to Fig. 1.6 for the definitions); i.e. the phase difference of the inner and outer waves is neither 0 nor π.

Earlier in the Introduction chapter, we discussed about a non-dimensional time based on the liquid viscosity and gas density and the nozzle diameter, $t_{lg} = \mu_l t/\rho_g D^2$, which was introduced by Jarrahbashi & Sirignano [79], for prediction of the real time at which the azimuthal instabilities (lobes formation, etc.) for a cylindrical liquid jet occur. Here we will test whether such dimensionless time could be used for qualitative prediction of the time at which certain KH waves appear on the liquid sheet surface or not.

From the earlier sections on the effects of the Re number and the density ratio, we saw that the instabilities occur earlier for higher Re number (lower μ_l) and lower density ratios (lower ρ_g). The dimensionless time t_{lg} is consistent with the latter statement, because $\dfrac{t_2}{t_1} \sim \dfrac{\rho_{g2}}{\rho_{g1}}$

based on the definition of t_{lg}; thus, as the gas density goes down the required time for appearance of certain KH instabilities decreases. However, by the definition, the t_{lg} form suggests that $\frac{t_2}{t_1} \sim \frac{\mu_{l1}}{\mu_{l2}}$; which means that the time at which the instabilities are first observed should be postponed by a decrease in the liquid viscosity. However, this is not consistent with what we see in our computational results. A decrease in the liquid viscosity corresponds to a higher Re number, and as indicated, the instabilities occur earlier at higher Re jets. Hence, t should be directly proportional to the liquid viscosity, opposing to what is suggested by t_{lg} definition.

From this analysis, we would conclude that the dimensionless time defined by Jarrahbashi and Sirignano [79] is not appropriate for the prediction of the 2D axisymmetric KH instabilities on an annular jet. This should not be misinterpreted as either one of the analyses are incorrect, though. The defined dimensionless time was devised for occurrence of 3D azimuthal instabilities on a cylindrical jet, while our simulation does not allow for those instabilities to occur (because of the axisymmetry). It should also be noted that Jarrahbashi and Sirignano [79] found that the 3D instabilities occur much faster than the axisymmetric ones, and this could be another justification for why such dimensionless time does not work in this 2D analysis.

The range of the observed KH and RT wavelengths on the liquid jets with different viscosity ratios are given in Figure 3.40 as a function of the injection time. As could be seen in all the plots, the average wavelength of the unstable KH waves increases with time, while the RT instabilities diminish in wavelength as we go forward in time. The advent of the instabilities are also quite the same in all the jets, regardless of their significant difference in the viscosity ratio. All the jets experience their first perturbations at $t^* = 20$–22.5.

The range of all the KH and RT wavelengths that have been observed during the start-up period of injection is illustrated as a function of the jet viscosity ratio, in Figure 3.41. What is interesting to note at a first glance, is that the range of both KH and RT instabilities are

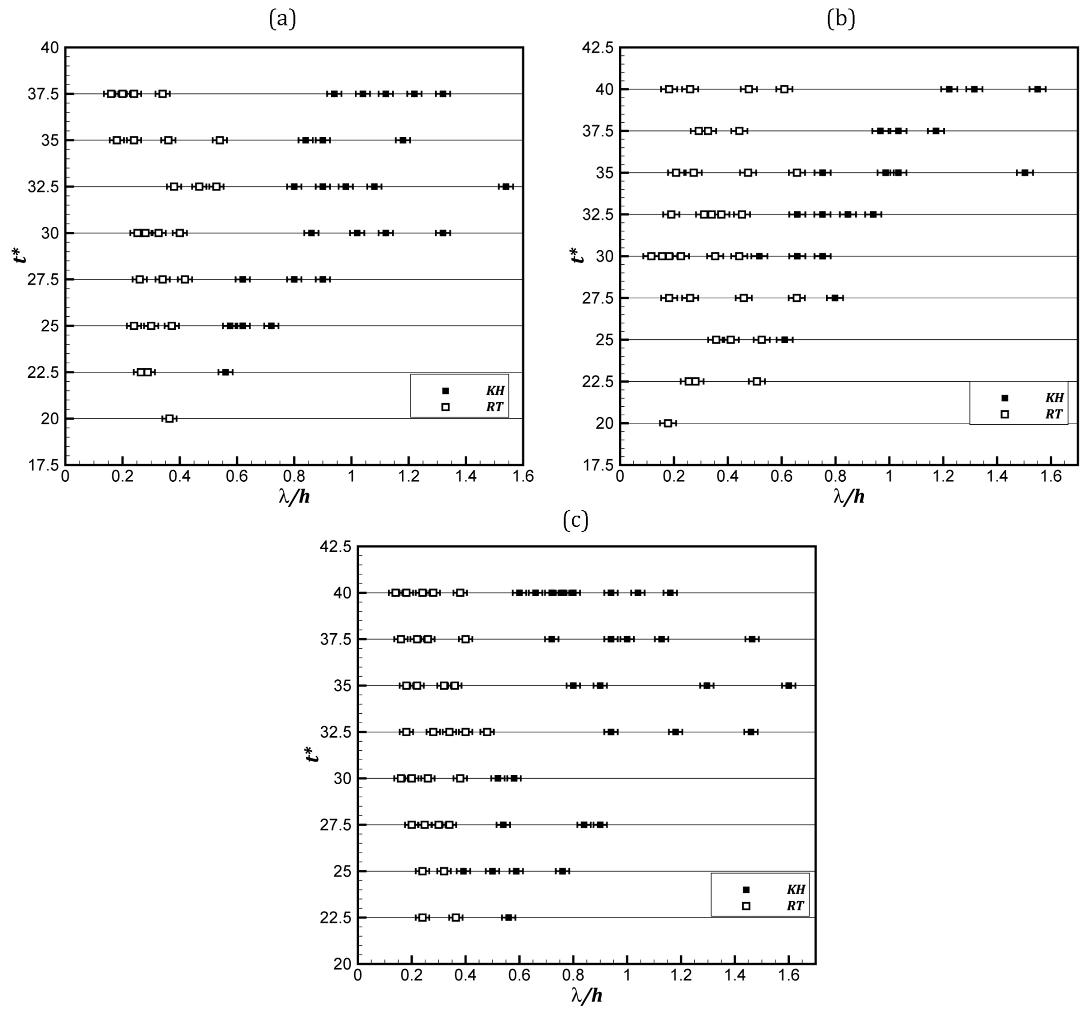

Figure 3.40: Dimensionless KH and RT wavelength spectrum vs. time; the error bars correspond to 5% and $h = 50\ \mu m$. $Re = 15,000$, $We = 30,000$, $\hat{\rho} = 0.05$, $\hat{d} = 0.8$; $\hat{\mu} = 0.0001$ (a), $\hat{\mu} = 0.0066$ (b), $\hat{\mu} = 0.05$ (c).

almost the same for all different viscosity ratios. This means that, statistically speaking, the range of the unstable wavelengths is independent of the gas/liquid viscosity ratio. This result is totally consistent with the results of linear VPF analysis that were presented earlier in this section (refer to Fig. 3.37). The largest and smallest KH waves that have been seen in the simulations are about $1.6h$ ($80\ \mu m$) and $0.5h$ ($25\ \mu m$), respectively, for all of the cases. The RT wavelengths also vary from $0.16h$ to $0.55h$, with a few small deviations in some cases.

In summary, it could be concluded that both the linear analysis and the numerical compu-

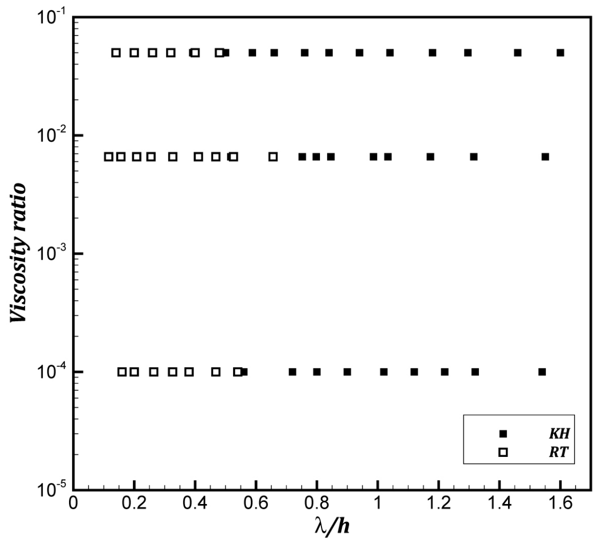

Figure 3.41: Dimensionless KH and RT wavelength spectrum during start-up vs. gas to liquid viscosity ratio. $h = 50\ \mu m$, $Re = 15,000$, $We = 30,000$, $\hat{\rho} = 0.05$, $\hat{d} = 0.8$; (the plot is in semi-log scale).

tations indicate that the viscosity ratio has negligible effects on the range of instabilities, as well as the rate and length of annular jet convergence towards the centerline. However, it should be noted that the time instant at which certain types of instabilities are observed on the liquid surface is affected by the viscosity ratio. Also, the zero level-set contours showed the noticeable differences in the deformation rate of the liquid jet near the tip region, for different viscosity ratios. The complete portrait of the jet development steps, for the cases that have been studied in this section, are given in Appendix D.

3.5 Sheet thickness effects

The annular liquid sheet thickness is varied in this section to study its effects on the unstable structures and the contraction rate. The sheet thickness is altered using the inner to outer nozzle diameter ratio $\hat{d} = d/D$, while the outer nozzle diameter is kept constant $D = 500\ \mu m$. The three diameter ratios that have been used in this study are, $\hat{d} = 0.7$, 0.8 and 0.9, corresponding to sheet thicknesses of 75, 50 and 25 μm, respectively (refer to Appendix

E for a complete picture). Obviously, as the diameter ratio increases, the sheet thickness decreases, and the annular sheet moves towards a planar sheet at the limit, where $\hat{d} \to 1$.

3.5.1 Sheet thickness and jet penetration

Figure 3.42 illustrates the axial variation of the dimensionless radius of the liquid sheet, for the three diameter ratio jets. As could be seen from the trajectory of the annular jets in this plot, the liquid sheets move more towards sinuous mode, as the sheet thickness decreases. This will be seen in more detail in the later section. Figure 3.42 shows that the annular sheet convergence length increases with increasing the diameter ratio (decreasing the sheet thickness). The sub-plot in Fig. 3.42 shows that the dimensionless convergence length for the thickest liquid sheet is about 0.7, while the thinnest sheet converges at a distance 1.4 times the nozzle diameter, downstream of the nozzle exit plane.

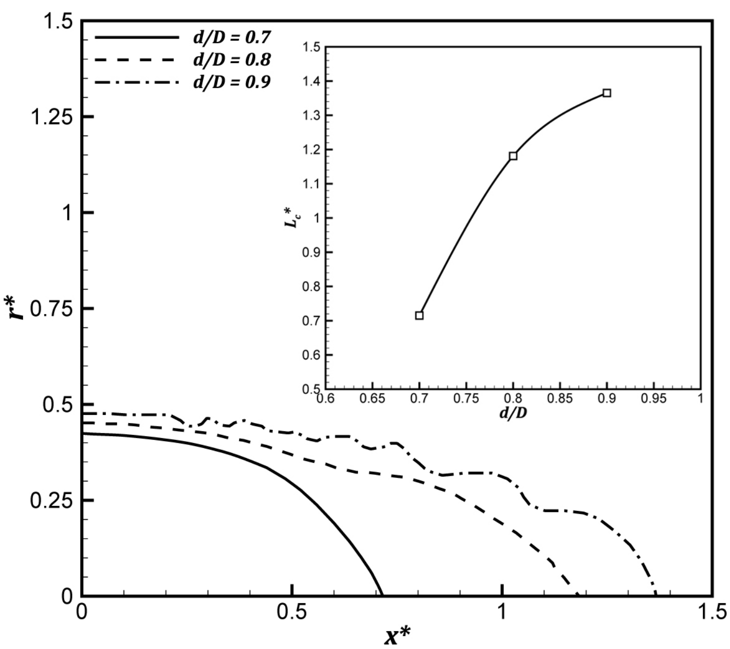

Figure 3.42: Axial variation of the dimensionless radius for different diameter ratios (the main plot); comparison between the convergence lengths of different diameter ratio cases (the sub-figure). $Re = 15,000$, $We = 30,000$, $\hat{\rho} = 0.05$, $\hat{\mu} = 0.0066$.

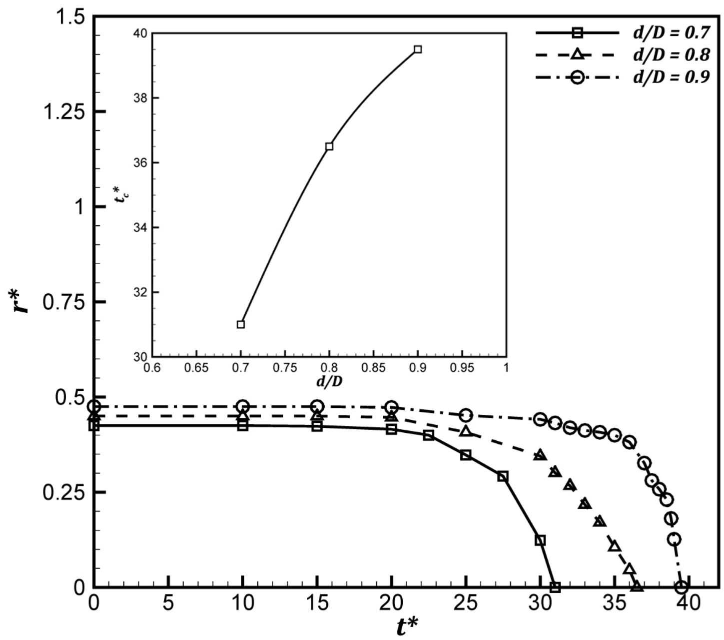

Figure 3.43: Variation of the dimensionless radius of the annular jet tip versus dimensionless time, for different diameter ratios (the main plot); comparison between the convergence rate of different diameter ratio cases (the sub-plot). $Re = 15,000$, $We = 30,000$, $\hat{\rho} = 0.05$, $\hat{\mu} = 0.0066$.

The radial convergence rate of the annular jets with different diameter ratios are compared in Figure 3.43. As could have been expected, the jet with smaller sheet thickness converges the latest. The thick annular sheet converges very soon at $t^* = 31$, while the convergence time is postponed for lower sheet thickness, and the thinnest liquid sheet converges at about $t \approx 40$; this is shown in the sub-plot of Fig. 3.43.

An interesting observation in the plots of Figure 3.43 is that, the radius of the thinnest liquid sheet start to decrease with a very steep slope after $t^* \approx 36$. In order to find out the reason for this sudden decrease, it is helpful to have a look at the liquid sheets' interfaces during the start-up period. The comparison between the liquid jets' interfaces for the thickest and the thinnest liquid sheets are given in Figure 3.44, at four different time intervals.

As could be seen in Figure 3.44, the thicker jet converges in much less time, while the thinner jet has mostly axial penetration, with very low radial deviation during the first 35 μs. At $t^* = 32.5$ a few Kelvin-Helmholtz waves appear on the inner and outer sides of both jets.

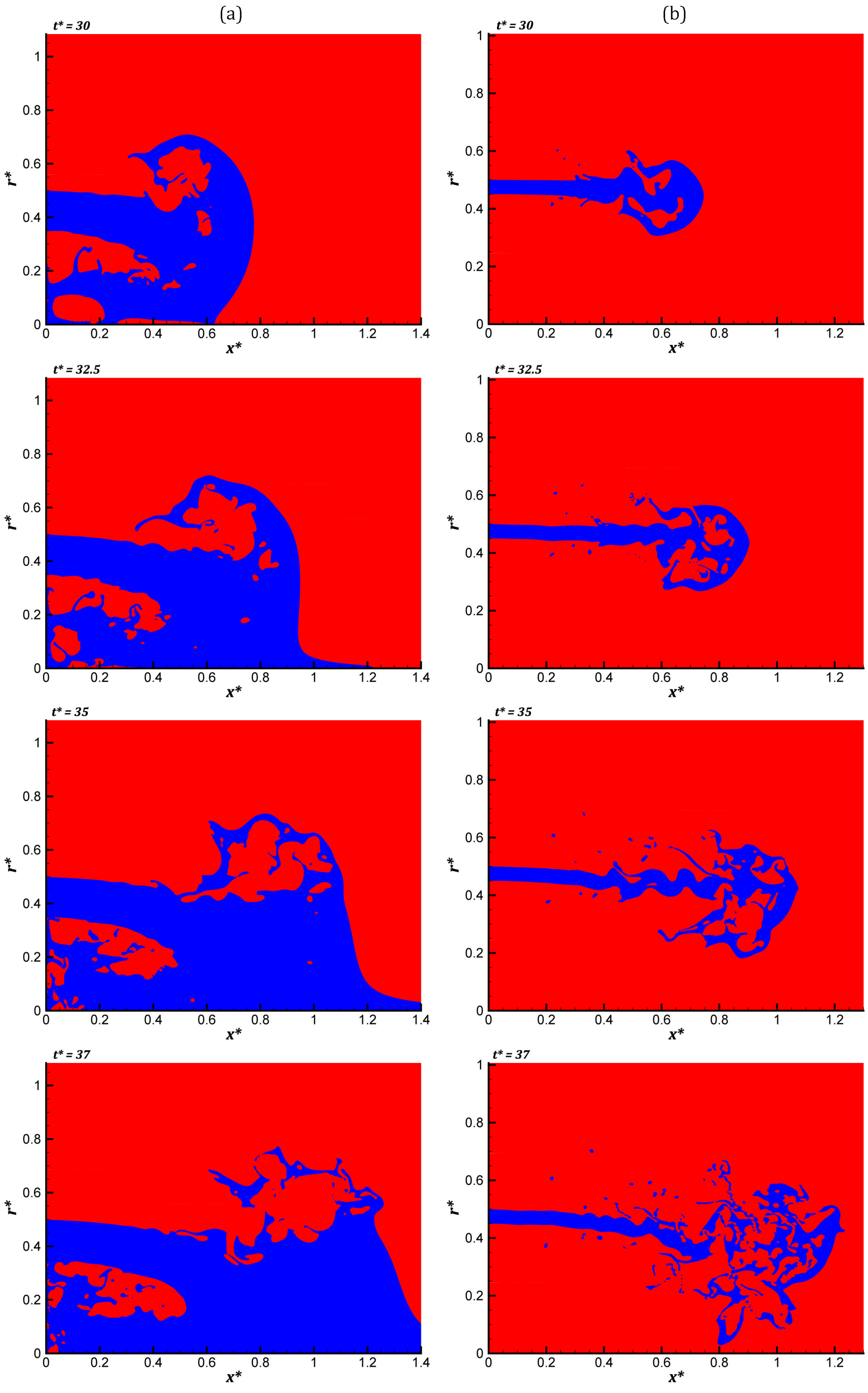

Figure 3.44: Jet development at $t^* = 30$ (top), $t^* = 32.5$ (mid-top), $t^* = 35$ (mid-bottom) and $t^* = 37$ (bottom). $Re = 15,000$, $We = 30,000$, $\hat{\rho} = 0.05$, $\hat{\mu} = 0.0066$; (a) $\hat{d} = 0.7$, (b) $\hat{d} = 0.9$.

These KH waves grow in amplitude and wavelength as time elapses and produce sinuous waves with similar amplitudes and wavelengths, and almost the same phase, on both inner and outer sides of the thinner liquid sheet at $t^* = 35$. The growth of the instabilities causes an attenuation in the sheet thickness, and we could clearly see the necking of the sheet at $x^* = 0.8$ at this time. The thin liquid sheet breaks-up at the location where this necking happens, at $t_b^* = 35.7$ (not shown in the figure). After the sheet break-up happens, the part of the jet, which is left downstream, deforms much faster, and without the necessary momentum from the main jet stem, which is now detached, to push it forward, its axial penetration slows down, while its cap spreads into the surrounding gas, under the effect of viscosity and the vortices that are now detached from the jet stem at the point of break-up. In other words, the jet cap experiences an explosion-like transformation which degrades the liquid jet behind the cap into thinner ligaments and rings. Since most of the detached vortices are advected in the radial direction, this phenomenon causes a sudden decrease in the jet radius; i.e. higher rate of radial convergence and lower axial penetration.

The effects of sheet break-up in the thinner annular jet could be also detected in the axial penetration rate of the jets, plotted in Figure 3.45. The thicker liquid sheet has higher penetration than the thinner ones at early time intervals $t^* < 25$. As is illustrated in this figure, and was also shown in Fig. 3.44, after $t^* = 25$ the thicker sheet starts to grow radially, while the thinner jets continue to grow axially, and overtake the thicker jet in axial penetration. However, after $t^* = 31$, when the thicker jet collapses on the axis of symmetry, its axial velocity increases as most of its momentum is contributed to axial penetration only (of-course some part of the jet is deflected upstream towards the nozzle on the centerline). Hence, the axial penetration of the thicker jet again becomes larger than the thinner ones. This obviously more pronounced when the thinnest liquid sheet breaks-up at $t^* \approx 36$. The effect of the sheet breakup on the axial penetration of the thin annular jet could be clearly seen in Fig. 3.45, where the line associated with $\hat{d} = 0.9$ (shown with circles) goes under the line associated with $\hat{d} = 0.8$ (shown with triangles). The point of intersection $t^* \approx 36$

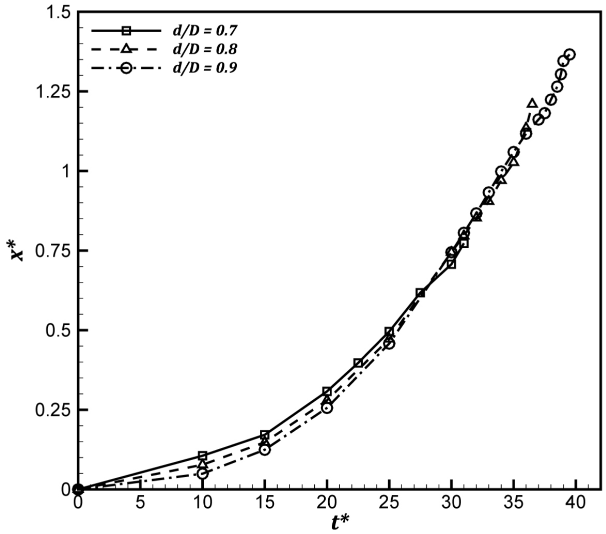

Figure 3.45: Axial penetration of the annular jet versus dimensionless time, for jets with different diameter ratios. $Re = 15,000$, $We = 30,000$, $\hat{\rho} = 0.05$, $\hat{\mu} = 0.0066$.

corresponds to the sheet breakup time.

3.5.2 Sheet thickness and the instability modes

Figure 3.46 based on the linear analysis of Joseph et al. [4], shows that the neutral wavelength, greater than which the waves become unstable, decreases with decreasing the sheet thickness. In other words, the range of the unstable waves grows with the diameter ratio. Also, the waves with similar wavelengths have higher growth rates for thinner liquid sheets based on the linear theory. This is consistent with our numerical results, shown in Figure 3.44, where we could see that the amplitude of the waves grow much faster in thinner liquid sheet jet (compare column b of Fig. 3.44 with column a). Later in this section, when we compare the wavelengths of the observed KH instabilities for different sheet thicknesses, we will see that they are also in accordance with the linear theory results.

In Figure 3.44, we saw that the KH waves emerged on the inner and outer sides of both thick and thin annular jets and they grew in time, as they moved upstream. Comparing

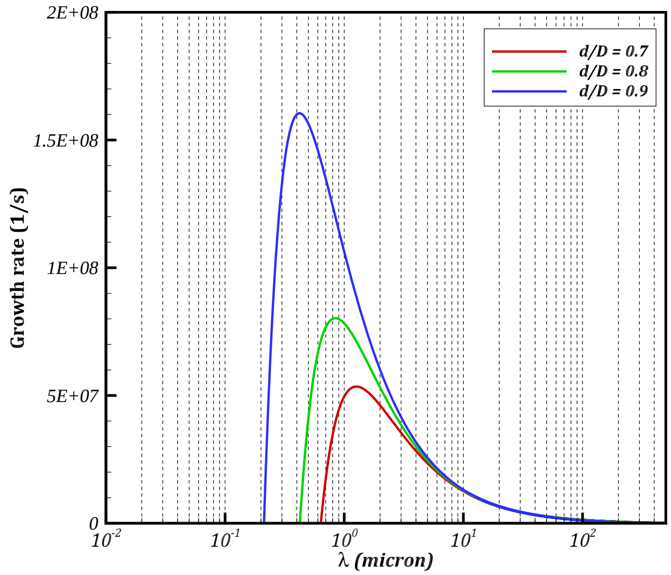

Figure 3.46: Linear growth rate as a function of wavelength for different diameter ratios, based on VPF instability analysis of Joseph et al. [4]. $Re = 15,000$, $We = 30,000$, $\hat{\rho} = 0.05$, $\hat{\mu} = 0.0066$.

the KH waves on the inner and outer interfaces of the thinnest liquid sheet at $t^* = 35$ (Fig. 3.44b), with the thicker liquid sheet, or even with all the other cases that were studied earlier, at the comparable time, we see that, these waves are the most in-phase waves that have been observed so far. The crests and troughs of all the KH waves on the outer interface match almost perfectly with the crests and troughs of the waves on the inner interface, respectively, for $\hat{d} = 0.9$ at $t^* = 35$. This shows that the instabilities move towards sinuous (anti-symmetric) mode as the liquid sheet becomes thinner (refer to Fig. 1.6 for modes' description).

After the KH instabilities grew sufficiently large and the thin liquid sheet broke-up at about $t^* \approx 36$, we saw that the amplitude of all of the waves died out, and a few small KH waves remained on the outer surface of the sheet, as is given in Figure 3.44b at $t^* = 37$. Tracking these waves later in time, we can see in Figure 3.47 that, the KH waves start to grow again on both sides of the sheet at $t^* = 38.5$, and their phases start to synchronize to form a sinuous wave. We can expect the same procedure to go on again and cause the second sheet

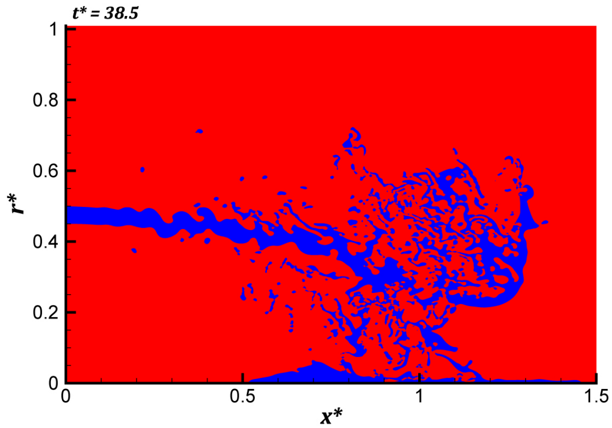

Figure 3.47: KH waves on the jet interface at $t^* = 38.5$. $Re = 15,000$, $We = 30,000$, $\hat{\rho} = 0.05$, $\hat{\mu} = 0.0066$, $\hat{d} = 0.9$.

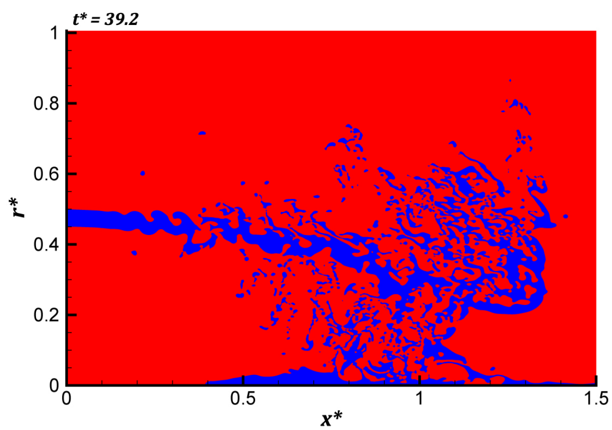

Figure 3.48: The second sheet breakup at $t^* = 39.2$. $Re = 15,000$, $We = 30,000$, $\hat{\rho} = 0.05$, $\hat{\mu} = 0.0066$, $\hat{d} = 0.9$.

breakup, and the same process is repeated over and over again. The second sheet breakup occurs at $t^*_{b2} = 39.2$ and $L^*_{b2} = 0.4$, as is recorded in Figure 3.48. Notice that, the sheet breakup distance from the nozzle exit has be halved from its primary length $L^*_{b1} = 0.8$. Thus, we can presume that all the next breakups happen at a closer distance from the nozzle exit, however, we know that this distance cannot decrease monotonically to zero, since the KH waves cannot appear at exactly the nozzle exit plane. This suggests the existence of a limit distance, where no breakups could happen at a distance less than that.

Figure 3.49 illustrates the dimensionless KH and RT wavelength spectrum at different time

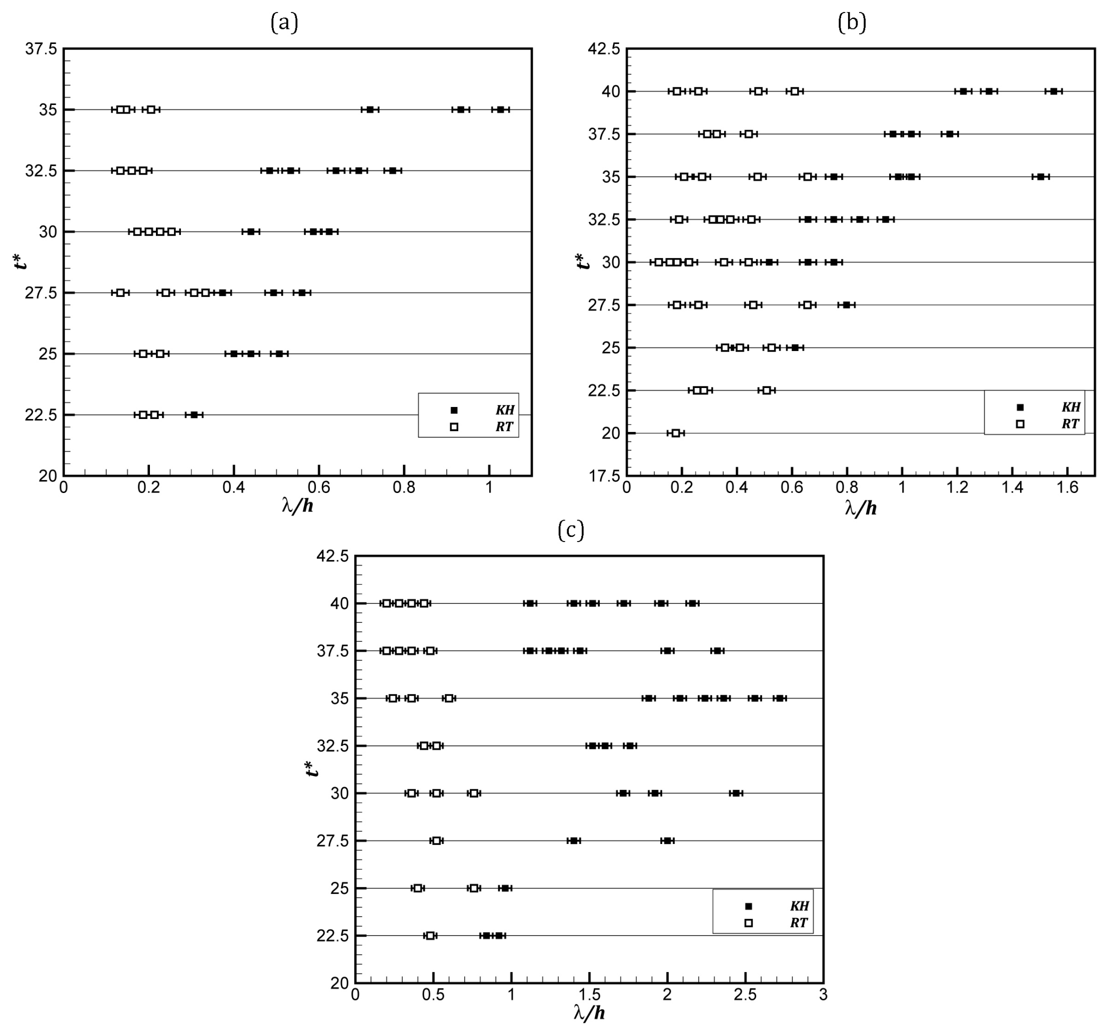

Figure 3.49: Dimensionless KH and RT wavelength spectrum vs. time; the error bars correspond to 5%. $Re = 15,000$, $We = 30,000$, $\hat{\rho} = 0.05$, $\hat{\mu} = 0.0066$; $\hat{d} = 0.7$ (a), $\hat{d} = 0.8$ (b), $\hat{d} = 0.9$ (c).

intervals for the three different sheet thicknesses. In the two thicker liquid sheets (a & b), the KH waves keep growing in wavelength as time passes. The thinner liquid sheet (c), however, has its longest KH wavelengths just before it breaks-up at $t^* = 35$, after which, the wavelength of the instabilities diminishes in time, and this cycle goes on again. The average wavelength of the RT instabilities decreases with time in all of the cases.

The normalized spectrum of all of the observed KH and RT instabilities are collected in Figure 3.50 versus the annular liquid sheet diameter ratio. As this figure shows, both KH and RT instabilities' wavelengths increase with the diameter ratio, as was suggested by

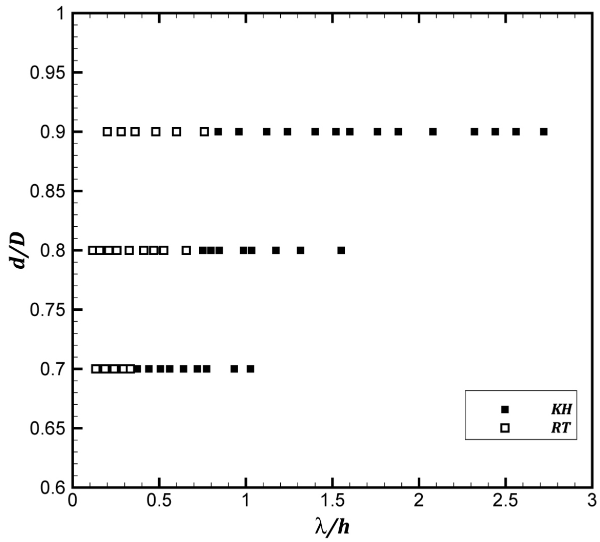

Figure 3.50: Dimensionless KH and RT wavelength spectrum during start-up vs. liquid sheet diameter ratio. $Re = 15,000$, $We = 30,000$, $\hat{\rho} = 0.05$, $\hat{\mu} = 0.0066$.

the linear Viscous Potential Flow analysis, plotted in Fig. 3.46. The thinnest liquid sheet experiences instabilities with wavelengths almost triple the sheet thickness, while the largest wavelength observed for the thickest liquid jet is about the same size as the sheet thickness. However, considering the dimensional wavelength we would see that the largest wavelength in all of the cases is almost the same, $\lambda \approx 75\ \mu m$ (notice that the sheet thicknesses are 75, 50 and 25 μm, from the thickest to the thinnest). The same story goes on for the RT instabilities, which also grow in wavelength as the sheet thickness decreases. The complete picture of the jet development steps for the thickest and thinnest liquid sheets are given in Appendix E.

3.6 Characteristic convergence time

In this section, we intend to modify the previously defined characteristic time $\tau = D/U$, by using the results that we have obtained for the convergence rate as a function of the other parameters. The new characteristic time τ_c, which can be used to normalize the dimensional time, represents the convergence time in a more appropriate way than the original definition. Based on the numerical results that were represented in the earlier sections, we can conclude that the characteristic convergence time is proportional to the dimensionless groups as follows:

$$\begin{aligned}
\tau_c &\propto Re^{-0.1} \\
\tau_c &\propto We^{-0.01} \\
\tau_c &\propto \hat{\rho}^{0.15} \\
\tau_c &\propto \hat{\mu}^{0.003} \\
\tau_c &\propto \hat{d}
\end{aligned}$$

Neglecting the dependence of the convergence time on the viscosity ratio, we can write the characteristic time as

$$\tau_c = Re^{-0.1} We^{-0.01} \hat{\rho}^{0.15} \hat{d} \, \frac{D}{U} \tag{3.3}$$

If we now define a new characteristic density as $\rho_c = \dfrac{\rho_g^{2.3}}{\rho_l^{1.3}}$, and call the Reynolds and Weber numbers based on this characteristic density Re_c and We_c, the characteristic time could be written as

$$\tau_c = \frac{1}{Re_c^{0.1} We_c^{0.01}} \frac{d}{U} \tag{3.4}$$

If we further neglect the minor effects of the We number, we can simplify the characteristic time as

$$\tau_c = \frac{d}{U \ Re_c^{0.1}} = \frac{\rho_l^{0.15} \mu_l^{0.1} d}{\rho_g^{0.25} U^{1.1} h^{0.1}} \tag{3.5}$$

and the dimensional time could be normalized by this characteristic convergence time to give $t^* = t/\tau_c$. Although this characteristic time embeds all of the parameters' effects, it should be noted that it is good only for the range of the dimensionless variables that were used in this study; i.e. high Reynolds and Weber numbers, $Re > 3000$ and $We > 6000$. Most probably, the effect of surface tension on the characteristic time will grow stronger at lower Weber numbers, so that it could not be simply neglected.

Chapter 4

Conclusions

A transient 2D axisymmetric finite-volume method was used in this research to study the spatial and temporal instabilities that occur on the interface of an annular liquid jet and an incompressible gas, during the start-up period of injection. Use was made of the level-set method to track the liquid/gas interface. The effects of five dimensionless flow parameters on the emerging Kelvin-Helmholtz and Rayleigh-Taylor instabilities were studied; Reynolds and Weber numbers, gas-to-liquid density and viscosity ratios, and inner-to-outer jet diameter ratio being the five parameters. The effects of these parameters on the annular jet convergence length and rate and the structure of sheet breakup and the resulting ligaments and rings sizes were also studied. The range of the Reynolds numbers used in this study were from 3000 to 30,000, indicating a turbulent regime; and the Weber number ranged from 6000 to 150,000.

Two significant velocity reversals were traced on the annular jet centerline, which corresponded to the recirculation zone and the jet collapse on the axis of symmetry. A few examples of the complicated vortical structures in the recirculation zone were shown and the vortex mechanism assisted by the KH instabilities, that were responsible for ejection of the liquid rings and ligaments from the main jet stream, were introduced. The convergence length and time of the annular liquid sheet were seen to decrease with the Re and We numbers and increase with the gas-to-liquid density and viscosity ratios and inner-to-outer annulus diameter ratio; the effects of the We number and the viscosity ratio being less significant than the others. A characteristic convergence time was also proposed based on the obtained numerical results in the range of parameters that were used in this study, which could more properly predict the dimensional time at which the jet collapses on the axis of symmetry.

The range of unstable KH and RT wavelengths were plotted at different time intervals from the start of injection, for all of the flow conditions that were studied in this report. The average wavelength of the observed KH and RT instabilities decreased with the Re and We numbers, and increased with the gas/liquid density ratio, and was almost independent of the viscosity ratio and the sheet thickness; indicating that the unstable wavelengths normalized by the sheet thickness increase significantly by decreasing the sheet thickness. The results also indicated the stabilizing effect of the liquid viscosity and surface tension at high Reynolds and Weber numbers.

Tracing the unstable KH and RT wavelengths in time, revealed that the average RT wavelengths tend to diminish, while the KH instabilities grow in wavelength as time elapses, during the start-up period of injection. For a very thin liquid sheet, however, the average KH wavelength reaches a maximum just before the sheet breaks-up and then decreases as a result of the breakup. Later in time, the KH wavelengths grow again and cause the second sheet breakup, which happens at a closer distance from the nozzle exit plane. The oscillation of the KH wavelengths between a maximum and minimum value, indicate that the thin annular sheet experiences several sheet breakup cycles, each of which cause detachment of numerous large and small vortices that move radially outward after they are shed from the the main liquid sheet stem during the breakup. The vortices advect liquid ligaments and rings (2D droplets) outward, and expedite the atomization process. For a very low liquid surface tension (high We number), it was seen that, the detached vortices have enough strength to dominate the surface tension forces and pinch-off thin liquid ligaments and rings and carry them with themselves. This mechanism justifies the observation of numerous small liquid rings and ligaments at the high We jet.

At the end, it is to be mentioned that both turbulence and the annular jet breakup are three-dimensional phenomena and need to be studied in 3D. The axisymmetric assumption of the jet injection problem in this study, hinders the occurrence of the azimuthal instabilities, which might happen sooner than the axisymmetric instabilities and can even grow faster than them. The 3D annular jet has been proven to be more unstable than the axisymmetric jet. For a better understanding of the atomization process, a 3D simulation of the planar or annular sheet breakup problem is suggested, along with the study of vortex structures and its corresponding mechanisms that cause formation of lobes and ligaments and eventually, sheet breakup and droplet pinch-off. Consideration of swirl to inhibit the annular collapse would also be of practical interest.

Bibliography

[1] Liu, H., "Science and Engineering of Droplets: Fundamentals and Applications", *Noyes Publications*, 2000.

[2] Rayleigh, L., "On the instability of jets", *Proc. London Mathematical Society*, Vol. 10, 1879, pp. 4-13.

[3] Weber, C., "On the breakdown of a fluid jet, Zum Zerfall eines Flussigkeitsstrahles", *Z. Angew. Math. und Mech.*, Vol. 11, 1931, pp. 136-154.

[4] Joseph, D. D., Funada, T., Wang, J., "Potential Flows of Viscous and Viscoelastic Liquids", *Cambridge University Press*, 2008.

[5] Taylor, G., "The instability of liquid surfaces when accelerated in a direction perpendicular to their planes. I", *Proc. R. Soc. Lond. A*, Vol. 201 (No. 1065), 1950, pp. 192-196.

[6] Squire, H. B., "Investigation of the instability of a moving liquid film", *Br. J. Appl. Phys.* Vol. 4, 1954, pp. 167–169.

[7] Dombrowski, N., Johns, W. R., "The aerodynamic instability and disintegration of viscous liquid sheets", *Chemical Engineering Science*, Vol. 18, 1963, pp. 203–214.

[8] Hagerty, W. W., Shea, J. F., "A study of the stability of plane fluid sheets", *Trans. ASME: J. Appl. Mech.*, Vol. 22, 1955, pp. 509–514.

[9] Sirignano, W. A., Mehring, C., "Review of theory of distortion and disintegration of liquid streams", *Prog. Energy Combus. Sci.*, Vol. 26, 2000, pp. 609–655.

[10] Li, X., Tankin, R. S., "On the temporal instability of a two-dimensional viscous liquid sheet", *J. Fluid Mech.*, Vol. 226, 1991, pp. 425–443.

[11] Ponstein, J., "Instability of rotating cylindrical jets", *Appl. Sci. Res. A*, Vol. 8, 1959, pp. 425-56.

[12] Crapper, G. D., Dombrowski, N., Pyott, G. A., "Kelvin-Helmholtz wave growth on cylindrical sheets", *J. Fluid Mech.*, Vol. 68, 1975, pp. 497-502.

[13] Meyer, J., Weihs, D., "Capillary instability of an annular liquid jet", *J. Fluid Mech.*, Vol. 179, 1987, pp. 531-45.

[14] Lee, J. G., Chen, L. D., "Linear stability analysis of gasliquid interface", *AIAA J.*, Vol. 29, 1991, pp. 1589-95.

[15] Shen, J., Li, X., "Instability of an annular viscous liquid jet", *Acta Mech.*, Vol. 114, 1996, pp. 167-183.

[16] Shen, J., Li, X., "Breakup of annular viscous liquid jets in two gas streams", *J. Propuls. Power*, Vol. 12, 1996, pp. 752-759.

[17] Jeandel, X., Dumouchel, C., "Influence of the viscosity on the linear stability of an annular liquid sheet", *Int. J. Heat Fluid Flow*, Vol. 20, 1999, pp. 499-506.

[18] Li, H. S., Kelly, R. E., "The instability of a liquid jet in a compressible airstream", *Phys. Fluids A*, Vol. 4, 1992, pp. 2162-2168.

[19] Cao, J., Li, X., "Stability of plane liquid sheets in compressible gas streams", *J. Propuls. Power*, Vol. 16, 2000, pp. 623-627.

[20] Craster, R. V., Matar, O. K., Papageorgiou, D. T., "On compound liquid threads with large viscosity contrasts", *J. Fluid Mech.*, Vol. 533, 2005, pp. 95-124.

[21] Ibrahim, E. A., McKinney, T. R., "Injection characteristics of non-swirling and swirling annular liquid sheets", *Proceedings of the Institution of Mechanical Engineers, Part C: Journal of Mechanical Engineering Science*, Vol. 220, 2006, pp. 203-214.

[22] Fu, Q., Yang, L., Qu, Y., Gu, B., "Linear stability analysis of a conical liquid sheet", *J. Propuls. Power*, Vol. 26, 2010, pp. 955-968.

[23] Ahmad, Z. U., Khayat, R. E., Maissa, P., Mathis, C., "Axisymmetric annular curtain stability", *Fluid Dyn. Res.*, Vol. 44, 2012, pp. 1-23.

[24] Jazayeri, S. A., Li, X., "Nonlinear instability of plane liquid sheets", *J. Fluid Mech.*, Vol. 406, 2000, pp. 281-308.

[25] Clark, C. J., Dombrowski, N., "Aerodynamic instability and disintegration of inviscid liquid sheets", *Proc. R. Soc. Lond. A*, Vol. 329, 1972, pp. 467-478.

[26] Rangel, R. H., Sirignano, w. A., "Nonlinear growth of Kelvin-Helmholtz instability: Effect of surface tension and density Ratio", *Phys. Fluids*, Vol. 31, 1988, pp. 1845-1855.

[27] Rangel, R. H., Sirignano, w. A., "The linear and nonlinear shear instability of a fluid sheet", *Phys. Fluids A*, Vol. 3, 1991, pp. 2392-2400.

[28] Panchagnula, M. V., Sojka, P. E., Baja, A. K., "The non-linear breakup of annular liquid sheets", *Proc. 11th Ann. Conf. Liquid Atom. Spray Systems*, 1998, pp. 170-174.

[29] Mehring, C., Sirignano, W. A., "Nonlinear distortion of infinitely long thin planar and annular liquid sheets", *Proc. 11th Ann. Conf. Liquid Atom. Spray Systems*, 1998a, pp. 155-159. ILASS, North and South America.

[30] Mehring, C., Sirignano, W. A., "Nonlinear distortion of semi-infinitely long thin planar and annular liquid sheets", *Proc. 11th Ann. Conf. Liquid Atom. Spray Systems*, 1998b, pp. 160-164. ILASS, North and South America.

[31] Mehring, C., Sirignano, W. A., "Axisymmetric capillary waves on thin annular liquid sheets part I: temporal stability", *Phys. Fluids*, Vol. 12, 1999a, pp. 1417-1439.

[32] Mehring, C., Sirignano, W. A., "Axisymmetric capillary waves on thin annular liquid sheets part I: spatial stability", *Phys. Fluids*, Vol. 12, 1999b, pp. 1440-1460.

[33] Mehring, C., Sirignano, W. A., "Nonlinear capillary wave distortion and disintegration of thin planar liquid sheets", *J. Fluid Mech.*, Vol. 388, 1999, pp. 69-113.

[34] Ibrahim, M. A., Jog, M. A., "Nonlinear instability of an annular liquid sheet exposed to gas flow", *Int. J. Multiphase flow*, Vol. 34, 2008, pp. 647-664.

[35] Crapper, G. D., Dombrowski, N., Jepson, W. P., Pyott, G. A., "A note on the growth of Kelvin-Helmholtz waves on thin liquid sheets", *J. Fluid Mech.*, Vol. 57, part 4, 1973, pp. 671-672.

[36] Mansour, A., Chigier, N., "Disintegration of liquid sheets", *Phys. Fluids A*, Vol. 2, 1990, pp. 706-719.

[37] Varga, C. M., Lasheras, J. C., Hopfinger, E. J., "Initial breakup of a small-diameter liquid jet by a high-speed gas stream", *J. Fluid Mech.*, Vol. 497, 2003, pp. 405-434.

[38] Marmottant, P., Villermaux, E., "On spray formation", *J. Fluid Mech.*, Vol. 498, 2004, pp. 73-111.

[39] Crua, C., Shoba, T., Heikal, M., Gold, M., Higham, C., "High-speed microscopic imaging of the initial stage of diesel spray formation and primary breakup", *SAE Int.*, 2010.

[40] Shoba, T. T., Crua, C., Heikal, M. R., Gold, M. "Optical characterization of diesel, RME and kerosene sprays by microscopic imaging", *24th European Conference on Liquid Atom. Spray Sys.*, 2011, pp. 1-9. ILASS-Europe 2011.

[41] Kendall, J. M., "Experiments on annular liquid jet instability and on the formation of liquid shells", *Phys. Fluids*, Vol. 29 (7), 1986, pp. 2086-2094.

[42] Carvalho, I. S., Heitor, M. V., "Liquid film break-up in a model of a prefilming airblast nozzle", *Exp. Fluids*, Vol. 24, 1998, pp. 408-415.

[43] Fu, H., Li, X., Prociw, L. A., Hu, T. C. J., "Experimental investigation on the breakup of annular liquid sheets in two co-flowing airstreams", *AIAA 1st International Energy Conversion Engineering Conference*, 2003, pp. 1-11.

[44] Wahono, S., Honnery, D., Soria, J., Ghojel, J., "High-speed visualization of primary break-up of an annular liquid sheet", *Exp. Fluids*, Vol. 44, 2008, pp. 451-459.

[45] Duke, D., Honnery, D., Soria, J., "A cross-correlation velocimetry technique for breakup of an annular liquid sheet", *Exp. Fluids*, Vol. 49, 2010, pp. 435-445.

[46] Stanley, S. A., Sarkar, S., Mellado, P., "A study of the flow-field evolution and mixing in a planar turbulent jet using direct numerical simulation", *J. Fluid Mech.*, Vol. 450, 2002, pp. 377-407.

[47] Klein, M., sadiki, A., Janicka, J., "Investigation of the influence of the Reynolds number on a plane jet using direct numerical simulation", *Int. J. Heat Trans. Fluid Flow*, Vol. 24, 2003, pp. 785-794.

[48] Klein, M., "Direct numerical simulation of a spatially developing water sheet at moderate Reynolds number", *Int. J. Heat Trans. Fluid Flow*, Vol. 26, 2005, pp. 722-731.

[49] Sander, W., Weigand, B., "Direct numerical simulation and analysis of instability enhancing parameters in liquid sheets at moderate Reynolds numbers", *Phys. Fluids*, Vol. 20 (053301), 2008.

[50] Richards, J. R., Lenhoff, A. M., Beris, A. N., "Dynamic breakup off liquid-liquid jets", *Phys. Fluids*, Vol. 6 (8), 1994, pp. 2640-2655.

[51] Yoon, S. S., Heister, S. D., "A nonlinear atomization model based on a boundary layer instability mechanism", *Phys. Fluids*, Vol. 16 (1), 2004, pp. 47-61.

[52] Park, H., Yoon, S. S., Heister, S. D., "A nonlinear atomization model for computation of drop size distributions and spray simulations", *Int. J. Numer. Meth. Fluids*, Vol. 48, 2005, pp. 1219-1240.

[53] Menard, T., Beau, P. A., Tanguy, S., Demoulin, F. X., Berlemont, A., "Primary break up modeling Part A: DNS, a tool to explore primary breakup", *ICLASS*, 2006.

[54] Pan, Y., Suga, K., "A numerical study on the breakup process of laminar liquid jets into a gas", *Phys. Fluids*, Vol. 18 (052101), 2006.

[55] Gorokhovski, M., Hermann, M., "Modeling primary atomization", *Annu. Rev. Fluid Mech.*, Vol. 40, 2008, pp. 343-366.

[56] Lebas, R., Menards, T., Beau, P. A., Berlemont, A., Demoulin, F. X., "Numerical simulation of primary break-up and atomization: DNS and modeling study", *Int. J. Multiphase Flow*, Vol. 35, 2009, pp. 247-260.

[57] Shinjo, J., Umemura, A., "Simulation of liquid jet primary breakup: Dynamics of ligament and droplet formation", *Int. J. Multiphase Flow*, Vol. 36, 2010, pp. 513-532.

[58] Chesnel, J., Reveillon, J., Menard, T. M., Demoulin, F. X., "Large Eddy Simulation of liquid jet atomization", *Atom. Sprays*, Vol. 21 (9), 2011, pp. 711-736.

[59] Ibrahim, A. A., "Comprehensive study of internal flow field and linear and nonlinear instability of an annular liquid sheet emanating from an atomizer", *PhD. Dissertation*, 2006, Department of Mechanical, Industrial and Nuclear Engineering, University of Cincinnati.

[60] Siamas, G. A., Jiang, X., Wrobel, L. C., "A numerical study of an annular liquid jet in a compressible gas medium", *Int. J. Multiphase Flow*, Vol. 34, 2008, pp. 393-407.

[61] Siamas, G. A., Jiang, X., Wrobel, L. C., "Numerical investigation of a perturbed swirling annular two-phase jet", *Int. J. Heat Fluid Flow*, Vol. 30, 2009, pp. 481-493.

[62] Siamas, G. A., Jiang, X., Wrobel, L. C., "Dynamics of annular gas-liquid two-phase swirling jets", *Int. J. Multiphase Flow*, Vol. 35, 2009, pp. 450-467.

[63] Dabiri, S., Sirignano, W. A., Joseph, D. D., "Cavitation in an orifice flow", *Phys. Fluids*, Vol. 19 (072112), 2007.

[64] Dabiri, S., Sirignano, W. A., Joseph, D. D., "Two-dimensional and axisymmetric viscous flow in apertures", *J. Fluid Mech.*, Vol. 605, 2008, pp. 1–18.

[65] Dabiri, S., "Effects of cavitation on high pressure atomization", *PhD. Dissertation*, 2009, University of California, Irvine.

[66] Brodkey, R. S., "The Phenomena of Fluid Motions", *Addison-Wesley*, Reading, Mass., 1967.

[67] Leonard, B. P., "A stable and accurate convective modeling procedure based on quadratic upstream interpolation", *Computer Methods in Applied Mechanics and Engineering*, Vol. 19, 1979, pp. 59–89.

[68] Hayase, T., Humphrey, J. A. C., Greif, R., "A consistently formulated QUICK scheme for fast and stable convergence using finite-volume iterative calculation procedure", *J. Comput. Phys.*, Vol. 98 (1), 1992, pp. 108–118.

[69] Patankar, S. V., Spalding, D. B., "A calculation procedure for heat, mass and momentum transfer in three-dimensional parabolic flows", *Int. J. Heat Mass Transfer*, Vol. 15 (10), 1972, p. 1787.

[70] Versteeg, H., Malalasekra, W., "An Introduction to Computational Fluid Dynamics, The Finite Volume method, 2nd ed.", *Pearson*, 2006, pp. 227–236.

[71] Tryggvason, G., Unverdi, S. O., "Computations of three-dimensional Rayleigh-Taylor instability", *Phys. Fluids A*, Vol. 2 (656659), 1990.

[72] Glimm, J., Bryan, O. M., Menikoff, R., Sharp, D., "Front tracking applied to Rayleigh-Taylor instability", *SIAM J. Sci. Stat. Comput.*, Vol. 7 (230251), 1986.

[73] Popinet, S., Zaleski, S., "A front-tracking algorithm for accurate presentation of surface tension", *Int. J. Numer. Meth. Fluids*, Vol. 30, 1999, pp. 775–793.

[74] Scardovelli, R., Zaleski, S., "Direct numerical simulation of free-surface and interfacial flow", *Annual Review of Fluid Mechanics*, Vol. 31, 1999, pp. 567–603.

[75] Zhao, H., Chan, T., Merriman, B., Osher, S., "Variational level-set approach to multiphase motion", *J. Comput. Phys.*, Vol. 127 (1), 1996, pp. 179–195.

[76] Sussman, M., Fatemi, E., Smereka, P., Osher, S., "An improved level-set method for incompressible two-phase flows", *Comput. Fluids*, Vol. 27, 1998, pp. 663–680.

[77] Osher, S., Fedkiw, R. P., "Level set methods: an overview and some recent results", *J. Comput. Phys.*, Vol. 169 (2), 2001, pp. 463–502.

[78] Jiang, G., Peng, D., "Weighted ENO schemes for Hamilton-Jacobi equations", *SIAM J. Sci. Comput.*, Vol. 21 (6), 2000, pp. 2126–2143.

[79] Jarrahbashi, D., Sirignano, W. A., "Vorticity dynamics for transient high-pressure liquid injection", *Phys. Fluids*, 2014, Under review.

[80] Jerome, J. J. S., Marty, S., Matas, J. P., Zaleski, S., Hoepffner, J., "Vortices catapult droplets in atomization", *Phys. Fluids*, Vol. 25 (112109), 2013.

Appendices

There are five appendices, each of which contains the complete picture of the annular jet development steps, for different cases of a certain dimensionless parameter. The Appendices are as follows: Appendix A, showing the two different Reynolds cases and the base case; Appendix B, for the two cases with different Weber numbers; Appendix C, showing the two different density ratio jets; Appendix D, corresponding to the two viscosity ratio cases; and, Appendix E, corresponding to the two cases with different diameter ratios.

Appendix A:

Fig. A1: Jet development (the base case); $Re = 15,000$, $We = 30,000$, $\hat{\rho} = 0.05$, $\hat{\mu} = 0.0066$, $\hat{d} = 0.8$.

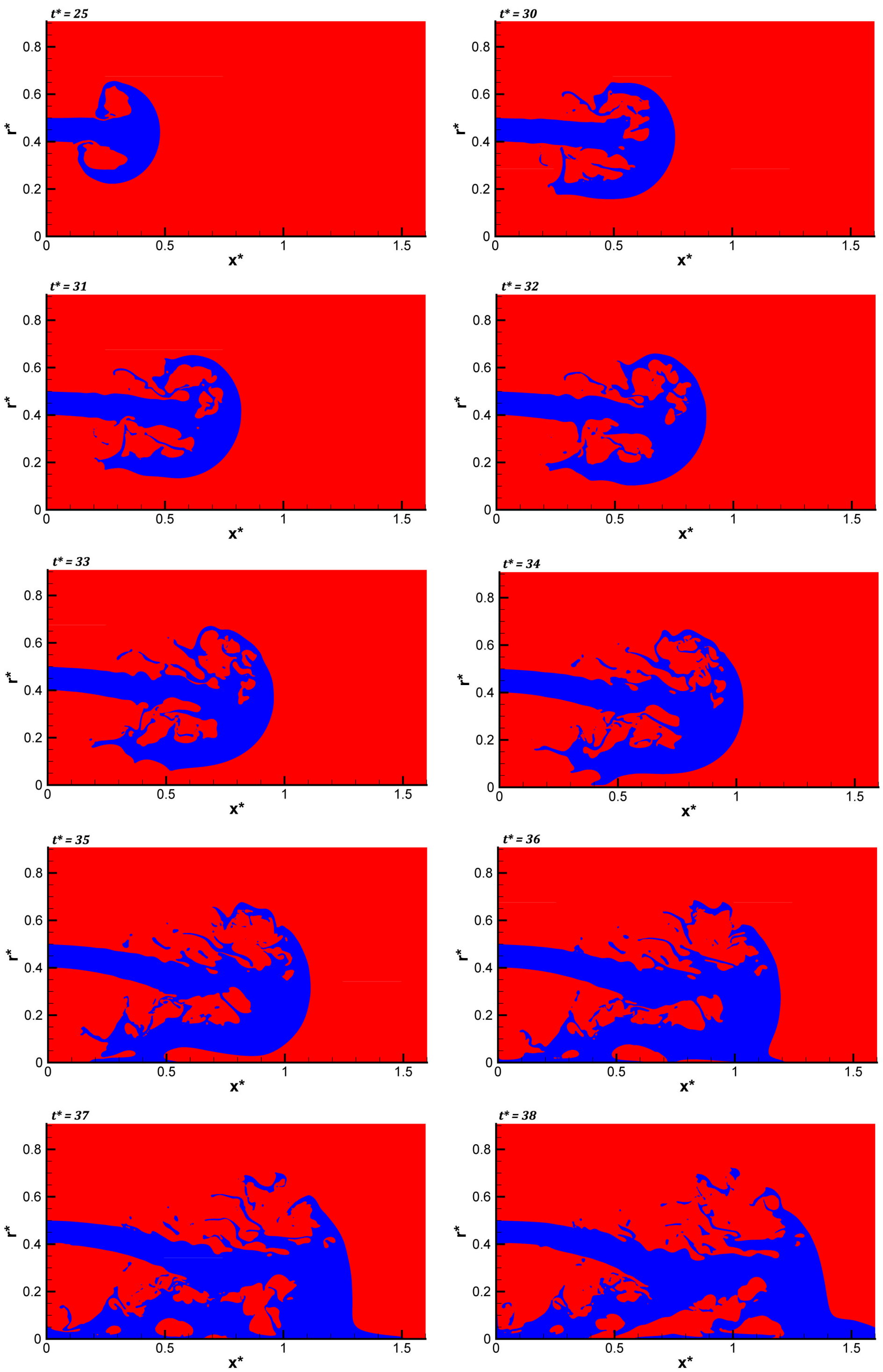

Fig. A2: Jet development; $Re = 3,000$, $We = 30,000$, $\hat{\rho} = 0.05$, $\hat{\mu} = 0.0066$, $\hat{d} = 0.8$.

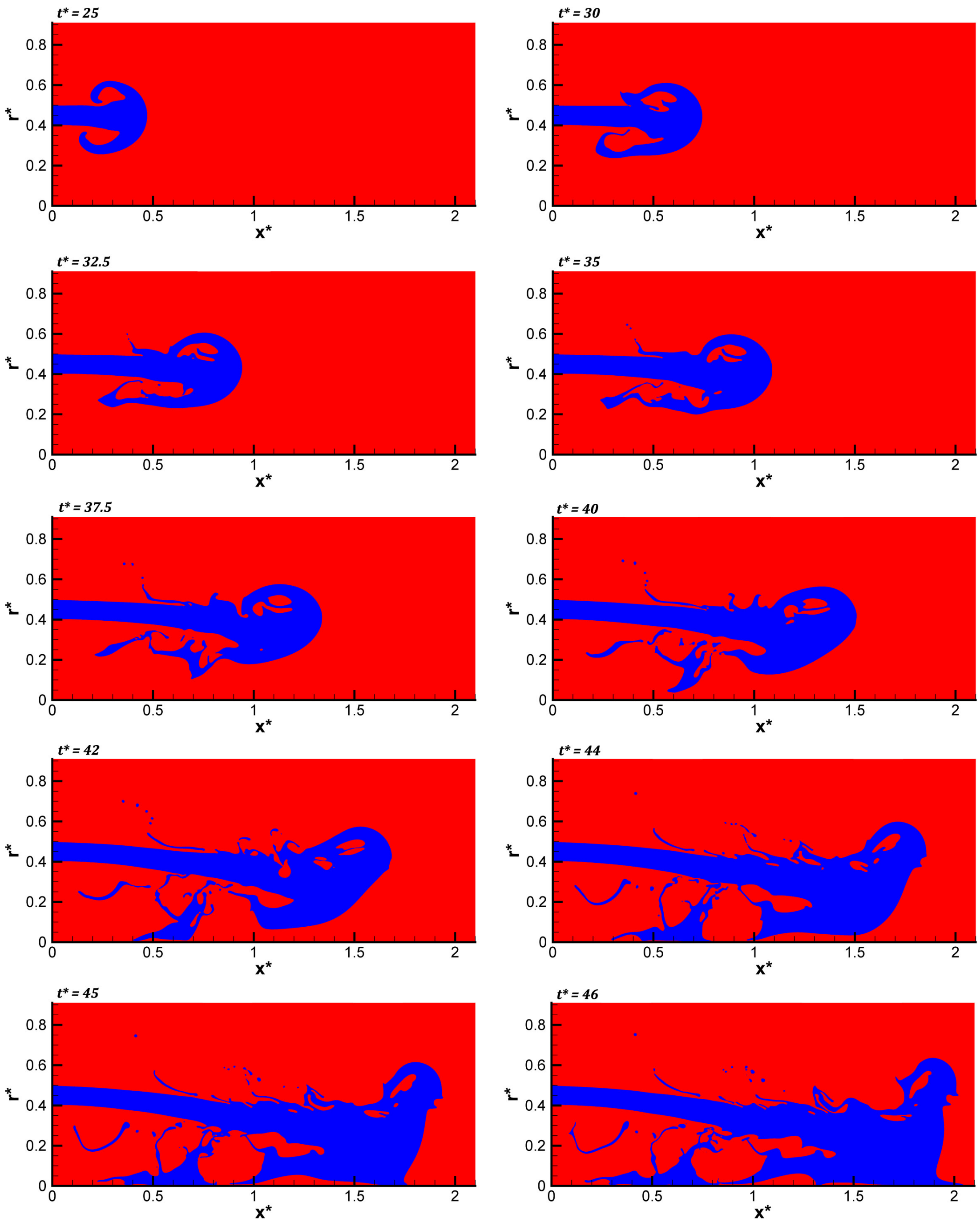

Fig. A3: Jet development; $Re = 30,000$, $We = 30,000$, $\hat{\rho} = 0.05$, $\hat{\mu} = 0.0066$, $\hat{d} = 0.8$.

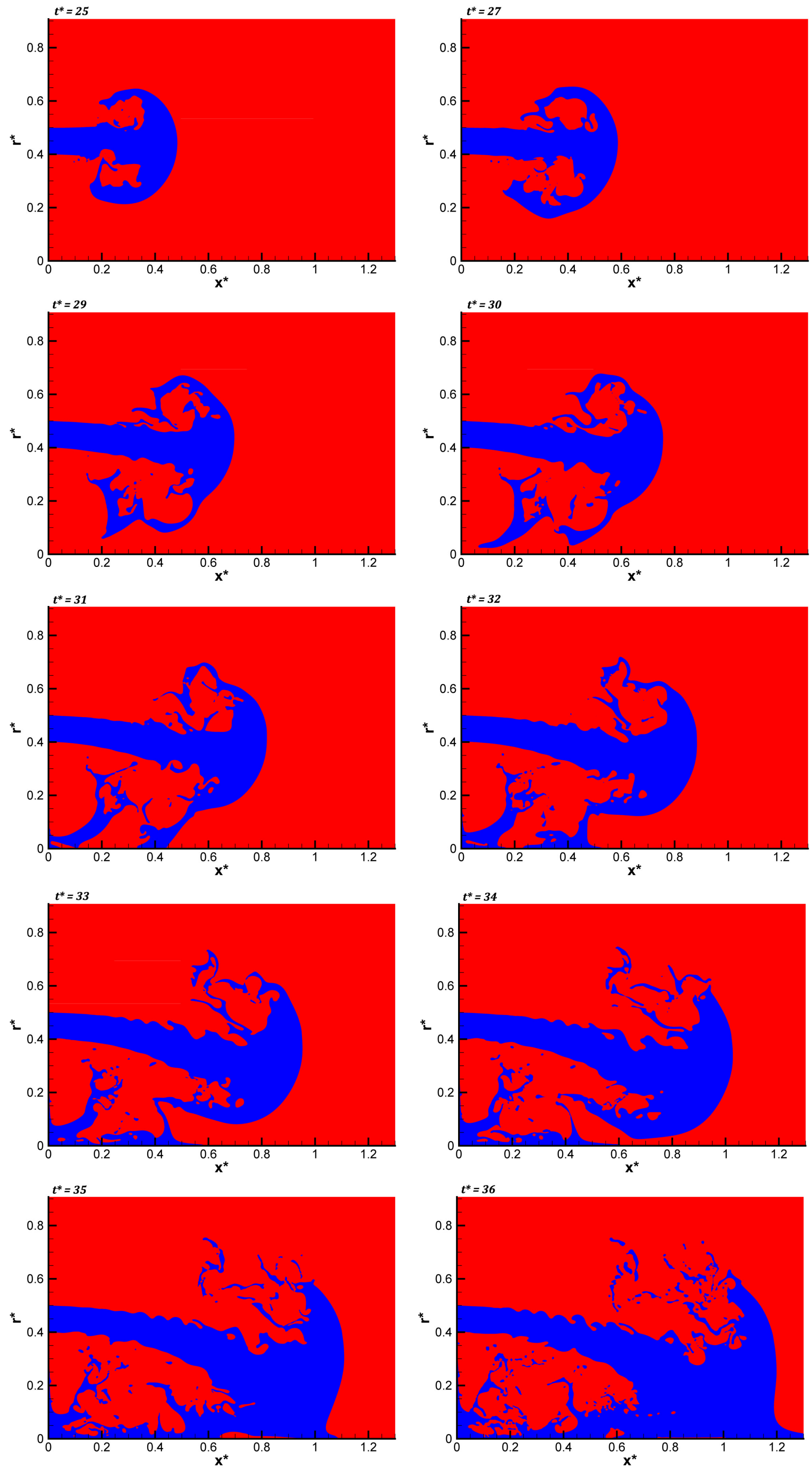

Appendix B:

Fig. B1: Jet development; $Re = 15,000$, $We = 6,000$, $\hat{\rho} = 0.05$, $\hat{\mu} = 0.0066$, $\hat{d} = 0.8$.

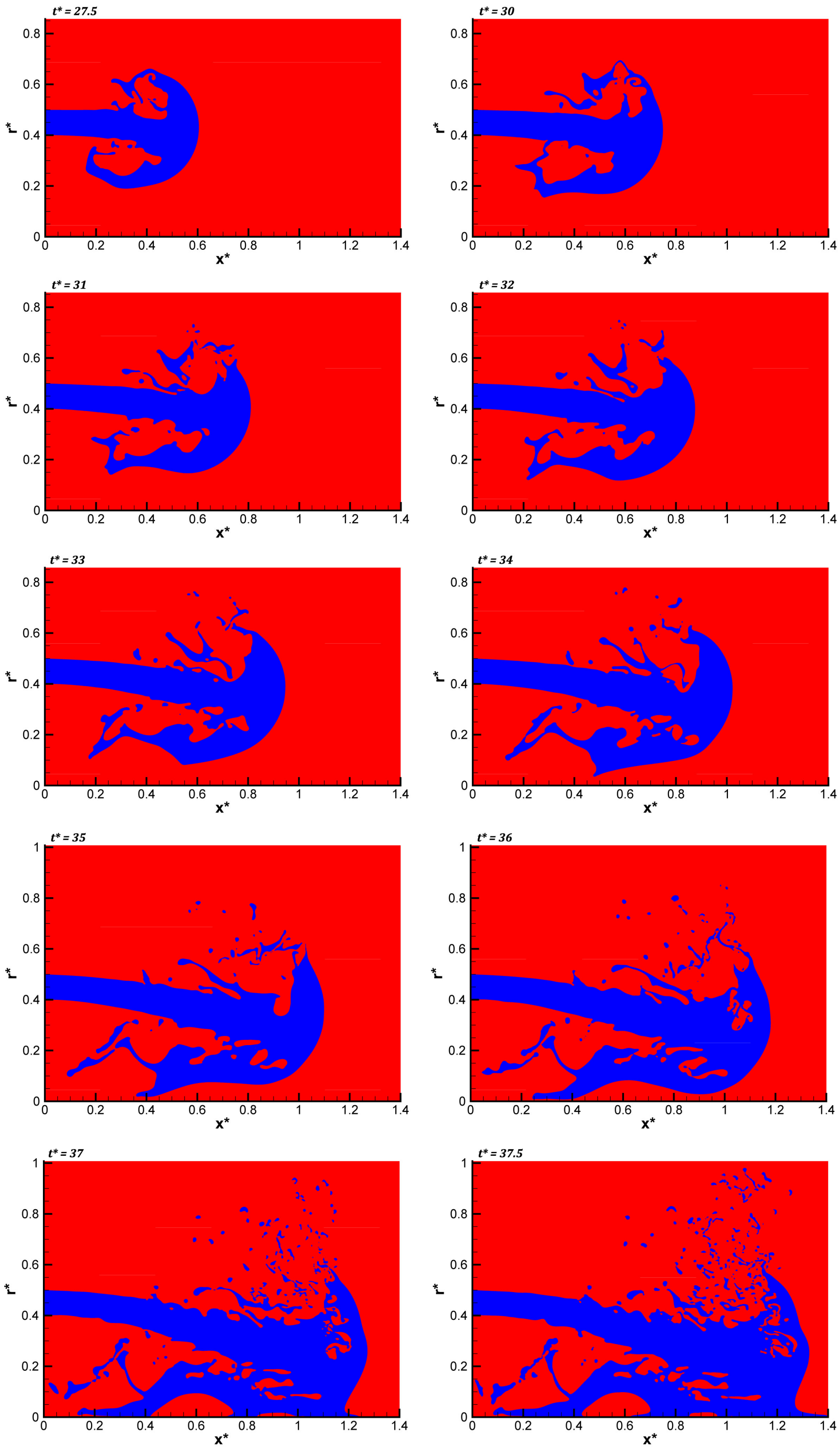

Fig. B2: Jet development; $Re = 15,000$, $We = 150,000$, $\hat{\rho} = 0.05$, $\hat{\mu} = 0.0066$, $\hat{d} = 0.8$.

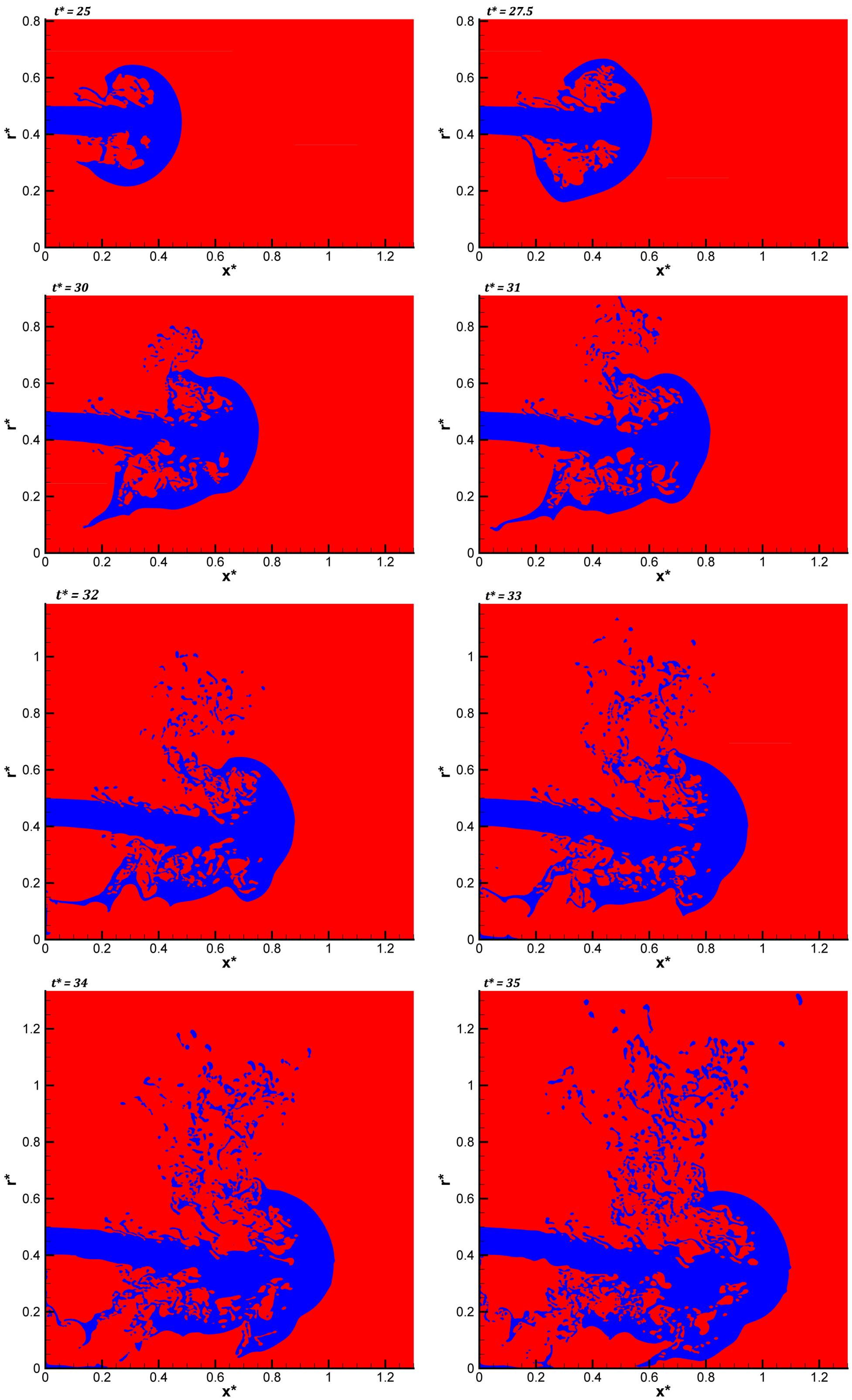

Appendix C:

Fig. C1: Jet development; $Re = 15,000$, $We = 30,000$, $\hat{\rho} = 0.1$, $\hat{\mu} = 0.0066$, $\hat{d} = 0.8$.

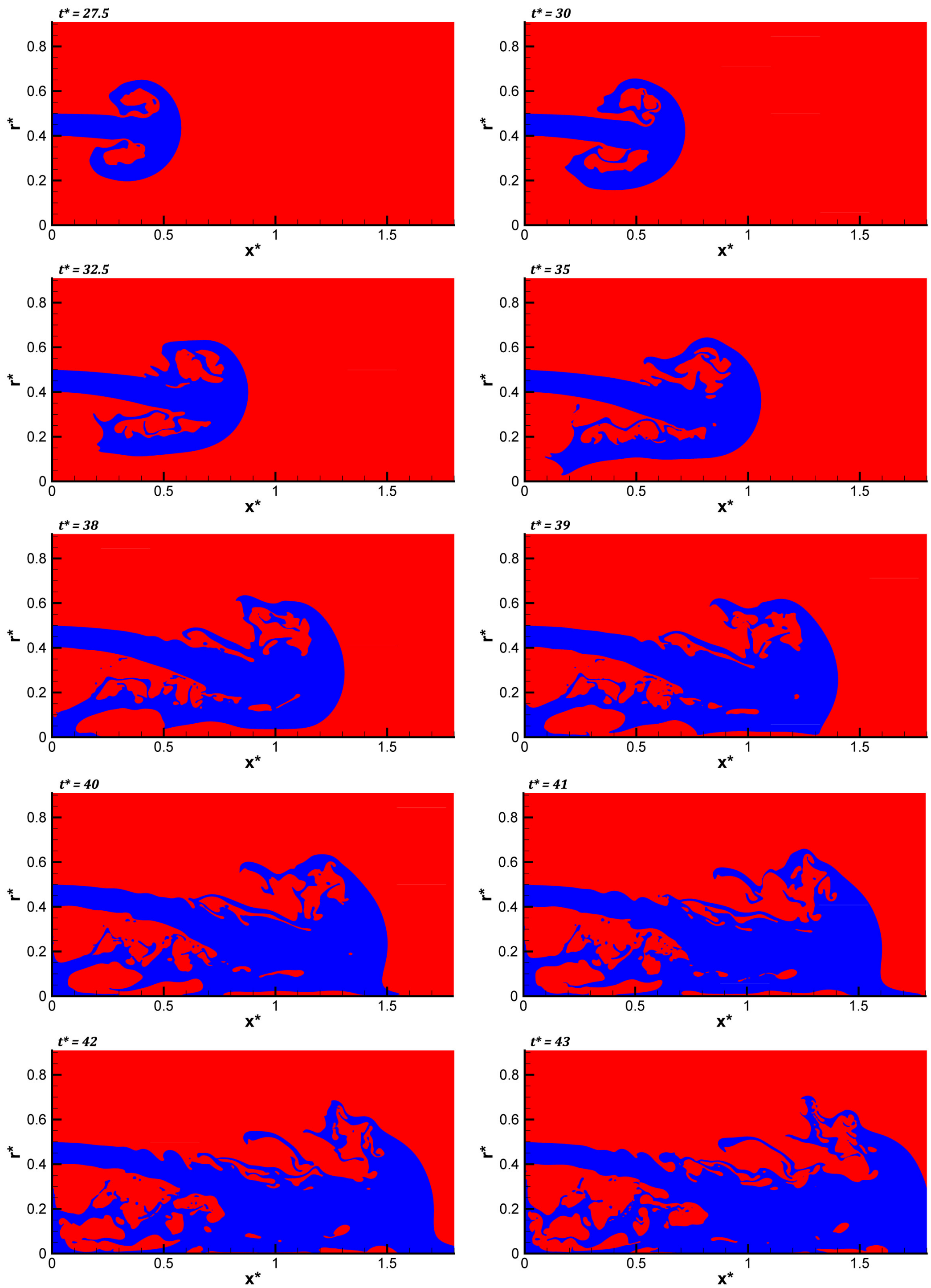

Fig. C2: Jet development; $Re = 15,000$, $We = 30,000$, $\hat{\rho} = 0.9$, $\hat{\mu} = 0.0066$, $\hat{d} = 0.8$.

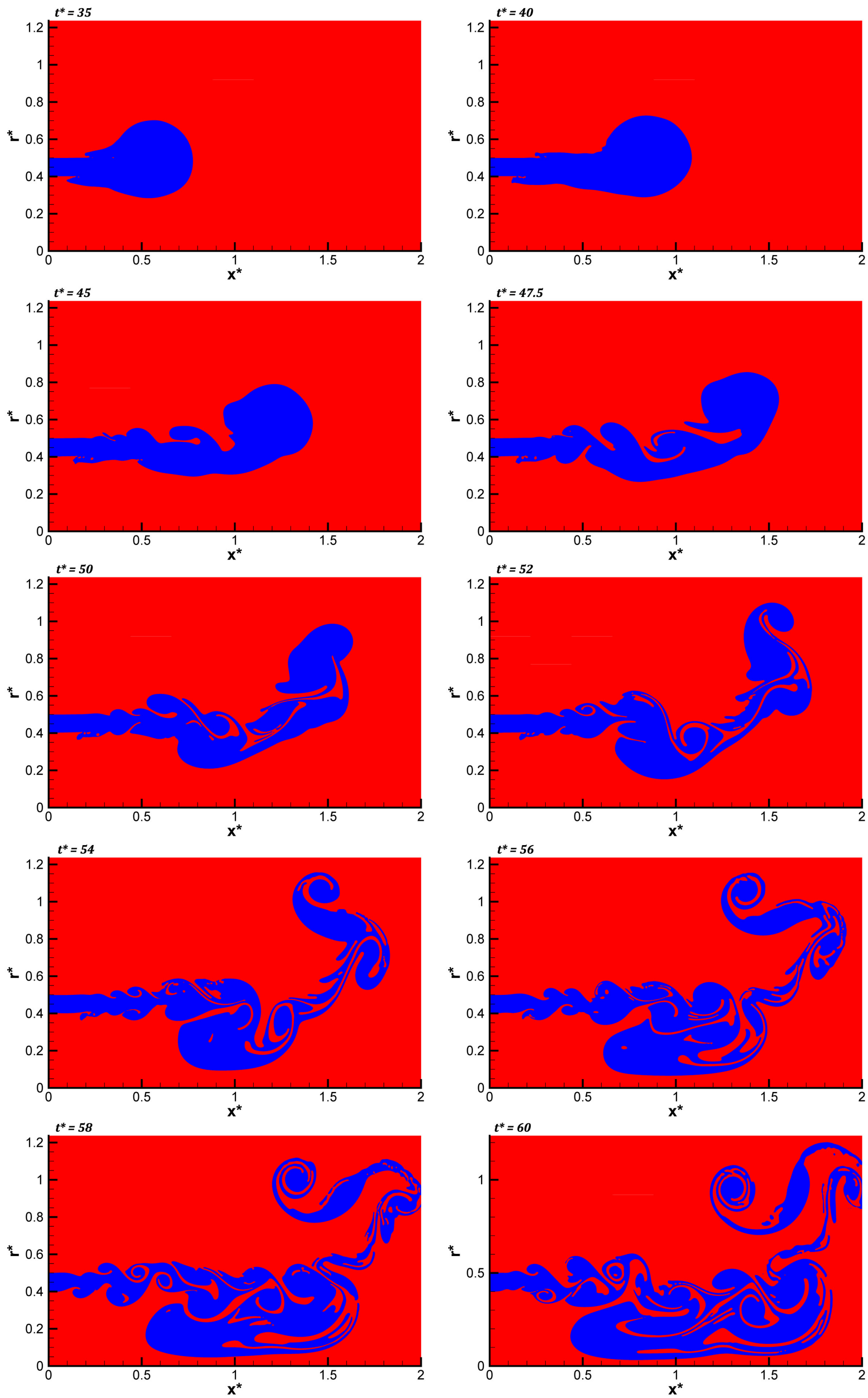

Appendix D:

Fig. D1: Jet development; $Re = 15,000$, $We = 30,000$, $\hat{\rho} = 0.05$, $\hat{\mu} = 0.0001$, $\hat{d} = 0.8$.

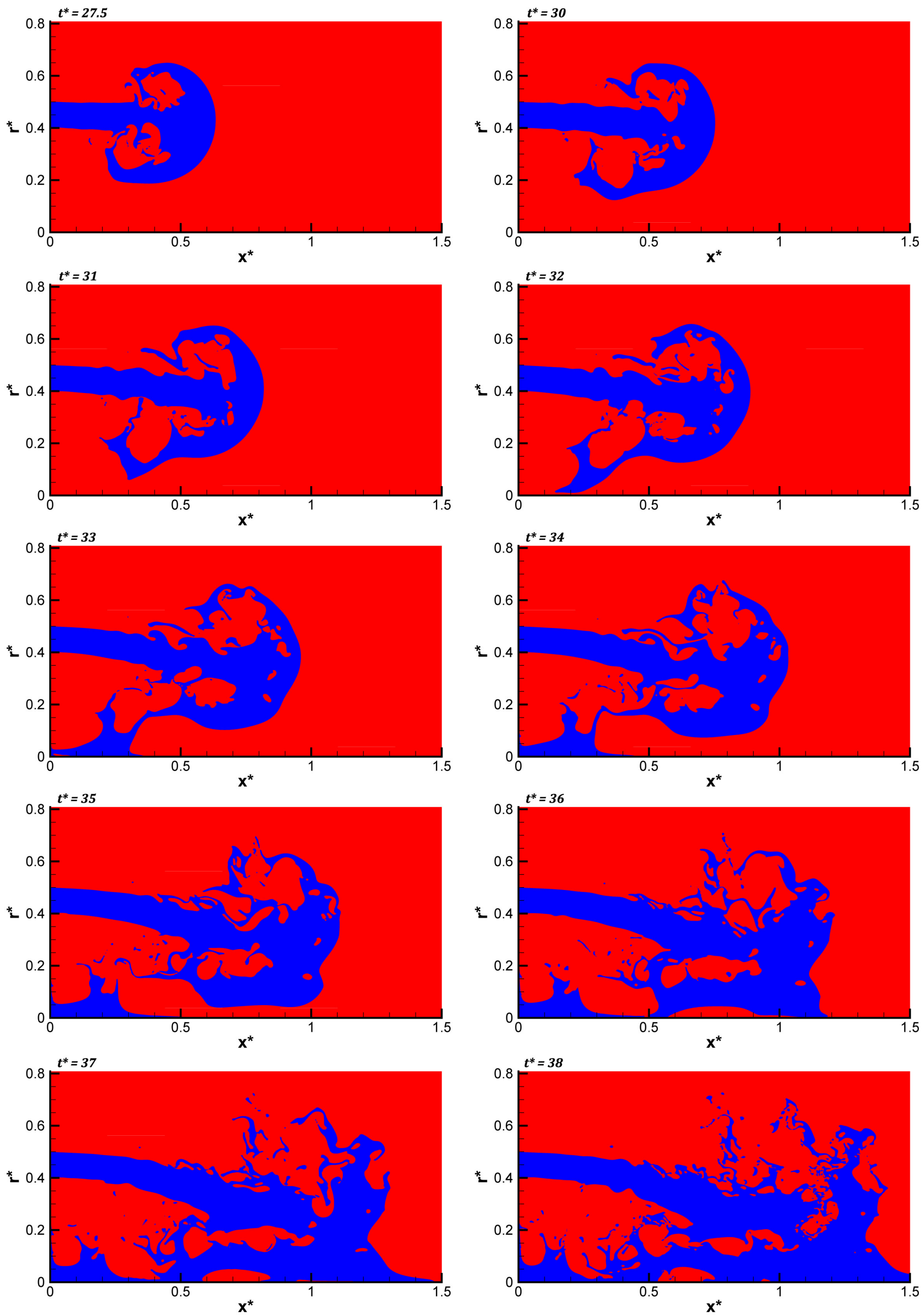

Fig. D2: Jet development; $Re = 15,000$, $We = 30,000$, $\hat{\rho} = 0.05$, $\hat{\mu} = 0.05$, $\hat{d} = 0.8$.

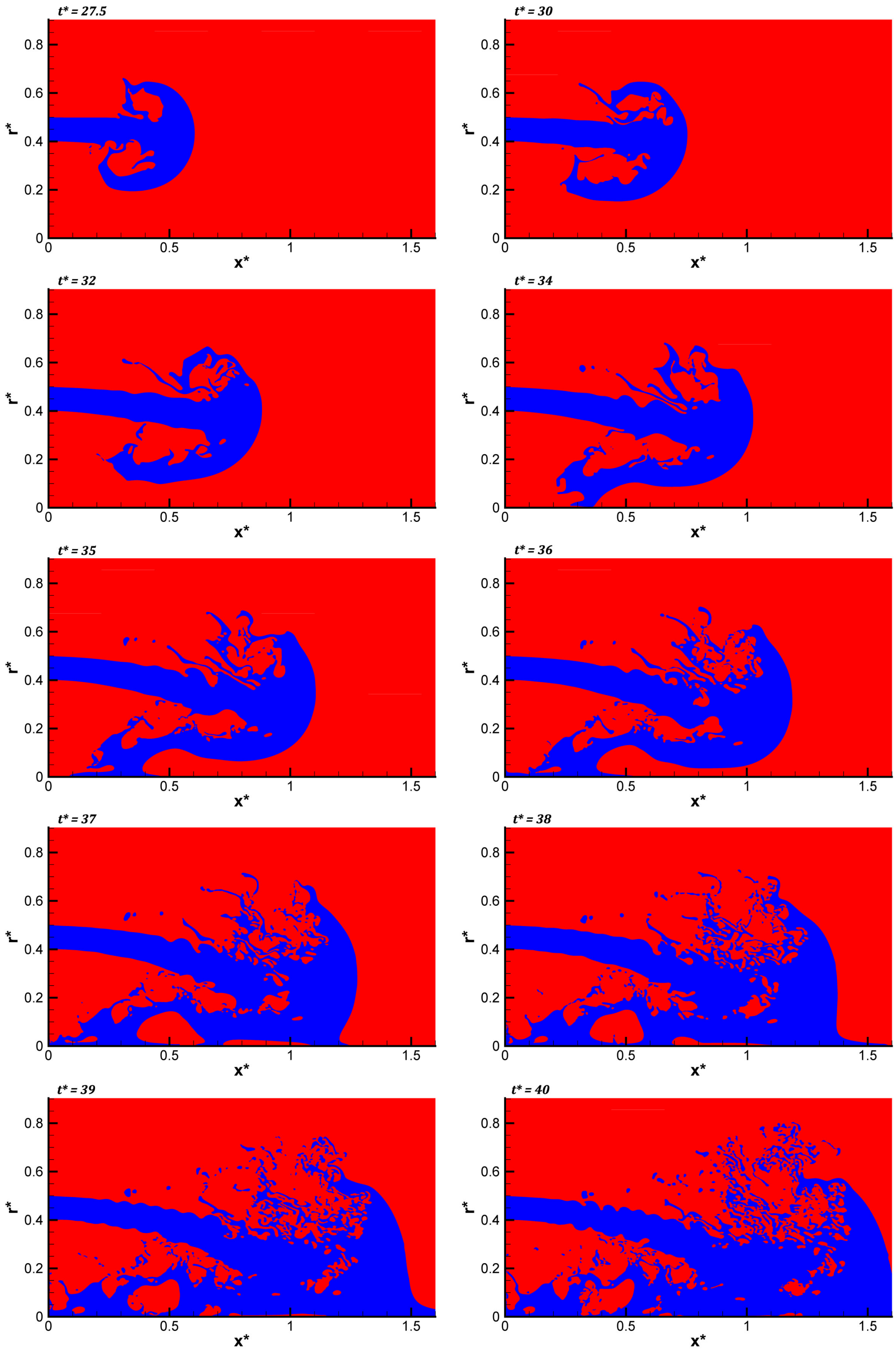

Appendix E:

Fig. E1: Jet development; $Re = 15,000$, $We = 30,000$, $\hat{\rho} = 0.05$, $\hat{\mu} = 0.0066$, $\hat{d} = 0.7$.

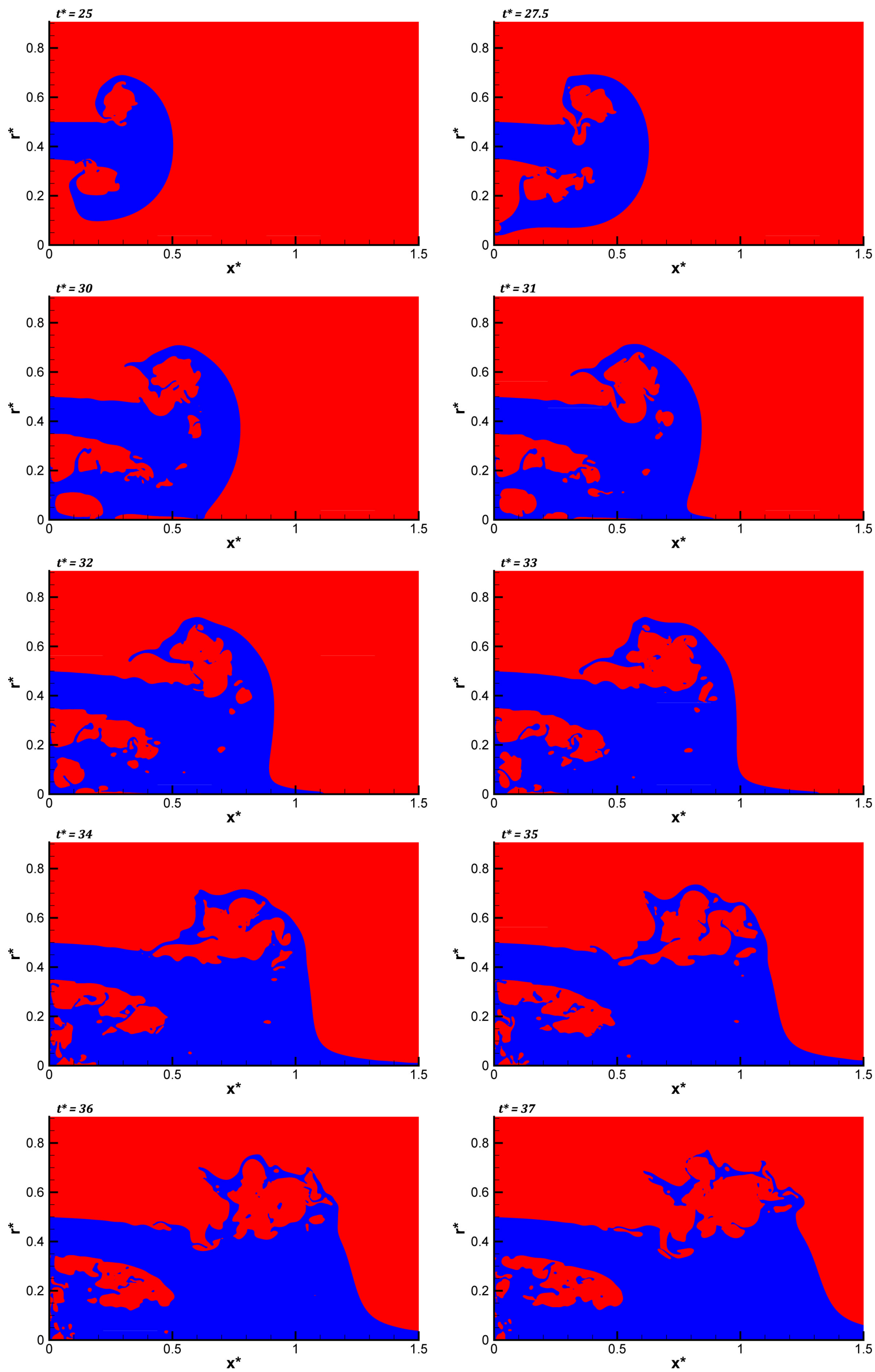

Fig. E2: Jet development; $Re = 15,000$, $We = 30,000$, $\hat{\rho} = 0.05$, $\hat{\mu} = 0.0066$, $\hat{d} = 0.9$.